공학박사 학위논문

Studies on metal organic framework derived Cu-Fe nitride and Fe-Mo oxynitride nanostructures for efficient water electrolysis

금속-유기 골격체(MOF) 를 활용하여 합성된

구리-철-질화물과 철-몰리브덴-산 질화물의

수분해 활성 연구

2021년 8월

서울대학교 융합과학기술대학원

융합과학부 나노융합전공

최예정

Studies on metal organic framework derived Cu-Fe nitride and Fe-Mo oxynitride nanostructures for efficient water electrolysis

지도 교수 박 원 철

이 논문을 공학박사 학위논문으로 제출함
2021년 6월

서울대학교 융합과학기술대학원
융합과학부 나노융합전공
최예정

최예정의 공학박사 학위논문을 인준함
2021년 6월

위 원 장 김 연 상
부위원장 박 원 철
위 원 이 강 원
위 원 장 익 황
위 원 김 재 윤

Abstract

Studies on metal organic framework derived Cu-Fe nitride and Fe-Mo oxynitride nanostructures for efficient water electrolysis

Yejung Choi
Department of Transdisciplinary Studies
Graduate School of Convergence Science and Technology
Seoul National University

Over the past several decades, nations have collectively acknowledged the necessity to slow global warming. Despite the political movements, the amount of greenhouse gases in the atmosphere increased at an alarming rate, elevating climate change from a serious issue to a full-blown emergency. One of the most effective ways to tackle global warming is to convert the current carbon-based energy system to green hydrogen-based energy system. Hydrogen can be transformed into final

energy such as electricity and thermal energy, and unlike electricity, it can be stored for a long time with a large capacity. As the current hydrogen production methods based on fossil fuels emit a considerable amount of carbon dioxide, green hydrogen production based on renewable energy is crucial. Green hydrogen can be produced through water electrolysis using an electrolyzer powered by renewable energy.

Water electrolysis consists of the hydrogen evolution reaction (HER) at the cathode and the oxygen evolution reaction (OER) at the anode. However, the intrinsically sluggish catalytic kinetics result in low electrochemical efficiency for practical use. It is therefore necessary to develop highly active advanced electrocatalysts. In quest of such feasible electrocatalyst, noble metal groups such as Pt, Ru and Ir were first proposed for their high catalytic activity toward electrolysis, but their high cost, scarcity, and unreliable stability limits them for large-scale industrial applications. For these reasons, earth-abundant transition-metals have been intensively investigated as alternative electrocatalysts, in various forms such as transition-metal oxides, carbides, phosphides, sulfides, nitrides, and oxynitrides. Among them, transition metal nitrides/oxynitrides (TMN/TMON) are of great interest owing to their advantageous properties including chemical stability and conductivity.

Transition metals such as Co, Ni, and Fe have been and still are extensively researched in various combinations and proven promising for electrolysis. Still, the relative lack of catalytic efficiency compared to the noble metal-based catalysts leaves plenty of room for further research. In this thesis, two examples of transition metal-based electrocatalysts efficient water electrolysis are presented.

The first study demonstrates an environmentally benign synthesis of CuFeN/CNT as efficient OER catalyst by structural and electrochemical manipulation of its precursor MOF. The morphology and the composition of the precursor MOF can be easily controlled by adjusting the solvent-dependent growth kinetics and the ratio of the transition metal salts. An exquisite urchin-shaped CuFe-MOF obtained in aqueous medium is then rapidly transformed into CuFeN via microwave-assisted nitridation. The final catalyst CuFeN/CNT exhibits a greatly enhanced OER activity compared to its unmodified counterparts, exhibiting current density increase from a mere 4.25 mA to 236.32 mA at an applied overpotential of 420 mV, marking a 5460.47 % increase.

The second study introduces a simple and energy-efficient synthesis route for MOF-derived FeMoON bifunctional catalyst. The final FeMoON catalyst derived from the precursor MOF is composed of 5-10 nm nanoparticles confined in the initial porous microstructure, providing

multiple active sites and pathway for electrolyte and gas transport. The incorporation of Mo in optimal ratio significantly enhances the catalytic activity by tuning the sluggish Volmer step. The optimized FeMoON alkaline water electrolyzer shows catalytic behavior surpassing that of the commercial Pt/C||RuO_2 electrolyzer (1.81 V and 1.89 V, respectively, for current density of 100 mA cm^{-2}) and good stability as well.

The impact of structural control, secondary metal introduction, and nitridation on the enhanced electrocatalytic performances of the catalysts in both studies were confirmed by significantly increased overpotentials of the comparisons prepared in the absence of each conditions.

Keywords: Metal Organic Framework (MOF), Nanocomposite, transition metal nitride/oxynitride, Electrocatalyst, Water electrolysis.

Contents

List of Figures

List of Tables

Chapter 1. Introduction

1.1 Introduction to water electrolysis

Fossil fuels have remained a dominant energy source since the times of industrial revolution.[1,2] Taking advantage of the massive energy, humanity achieved rapid industrial growth within a short time. Now in consequence, humankinds are faced with fuel depletion and severe environmental issues.[3–5]. In recognition of this crisis, there is a global movement toward sustainable zero-emission energy sources.[6–8]

In the center of attention lies hydrogen, the most abundant element in the universe. Hydrogen is a clean-burning molecule that contains massive energy density surpassing that of any fossil fuel.[9] Hydrogen supply is now a major business globally. As of 2018, the global demand for hydrogen rose more than threefold since 1975 and is forecasted to continue growing (Figure 1).[10,11]

At present, ~95 % of industrial hydrogen gas is produced through coal gasification and natural gas steam reforming, where enormous amounts of energy is consumed and significant carbon emission is involved (Figure 2).[12–15] Therefore, a more energy efficient and clean approach

is necessary for in order to fully utilize hydrogen as an alternative energy source. There are two main low-carbon production routes: 1. coupling conventional technologies with carbon capture and utilization or storage (CCUS) and 2.Generating hydrogen through water electrolysis. Due to the already existing massive facilities and production cost, CCUS will likely remain the main route in the short-medium term. Water electrolyzers on the other hand is a rapidly expanding area with increasing number and size of projects and installed electrolyzer capacity (Figure 3). In 2020, Japan commenced a 10 MW project and Canada started a 20-MW project. There also have been developments announced to operate in hundreds of MWs scale in the early 2020. The 2020 hydrogen strategy report by European Commissions ambitiously stated that they would be supporting the installation of minimum of 6 GW of renewable electrolyzers within five years in the European Union. The International Energy Agency (IEA)'s 2020 tracking report states that low-carbon hydrogen production will continue to grow and must to grow tremendously in effort to meet the Sustainable Development Scenario (SDS) (Figure 4). SDS is in full alignment with the Paris agreement where the objective is in "holding the increase in the global average temperature to well below 2 °C above pre-industrial levels and pursuing efforts to limit the temperature increase to 1.5 °C above pre-industrial

levels".[16]

The principle of water electrolysis was first introduced by Deiman, van Troostwijk, and Volta.[17] Water electrolysis is utilizing electrical energy to break apart water molecules into hydrogen and oxygen at cathode and anode respectively, through hydrogen evolution reaction (HER) and oxygen evolution reaction (OER) (Figure 5). Water electrolysis receives great attention as it can be also be powered by sustainable energy sources such as solar, hydro, wind, or more, resulting in a completely emission free energy generation.[18] Extensive research on electrolysis is in place over the globe to follow the massive shift in energy trend. The main challenges are in cost reduction, efficiency, and lifetime.

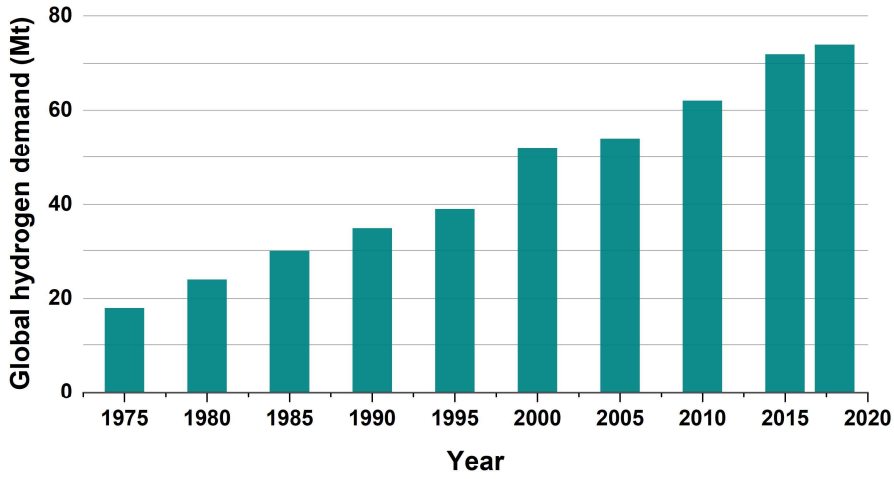

Figure 1 The growth of global demand for pure hydrogen from 1975 to 2018. International Energy Agency (IEA) technology report, 2019.[10]

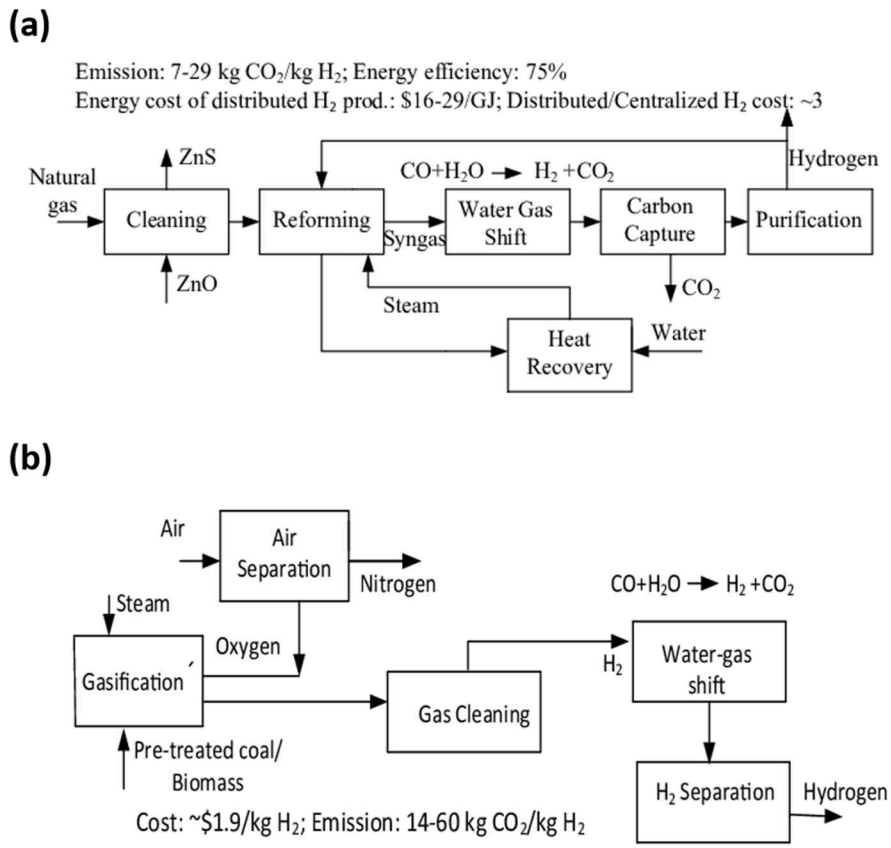

Figure 2 Typical hydrogen production by steam reforming of natural gas (a) and gasification of coal (b). [12]

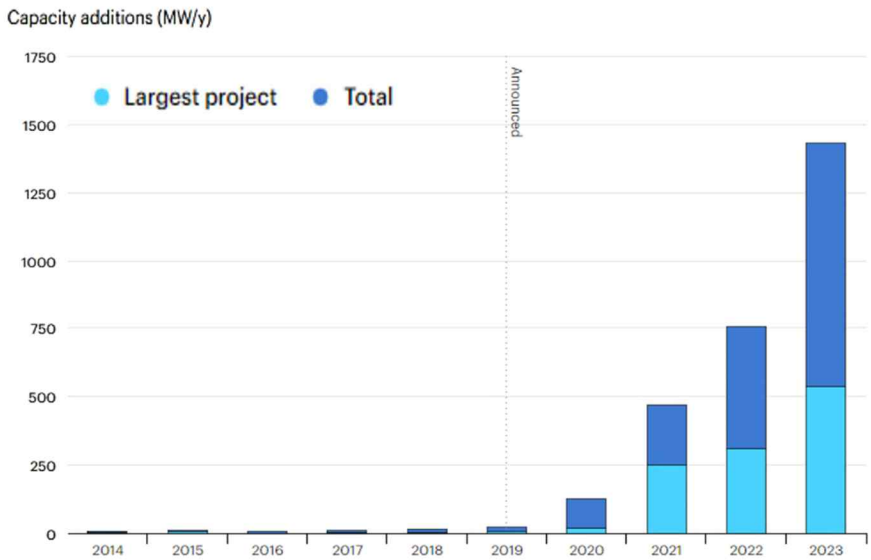

Figure 3 Global electrolysis capacity becoming operational annually, 2014-2023, historical and announced.[19]

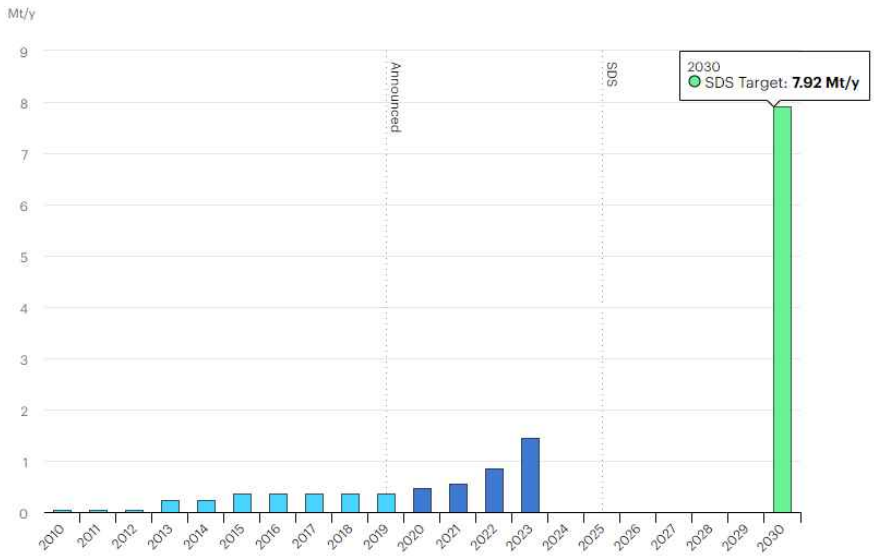

Figure 4 Low-carbon hydrogen production, 2010-2030, historical, announced and in the Sustainable Development Scenario, 2030.[19]

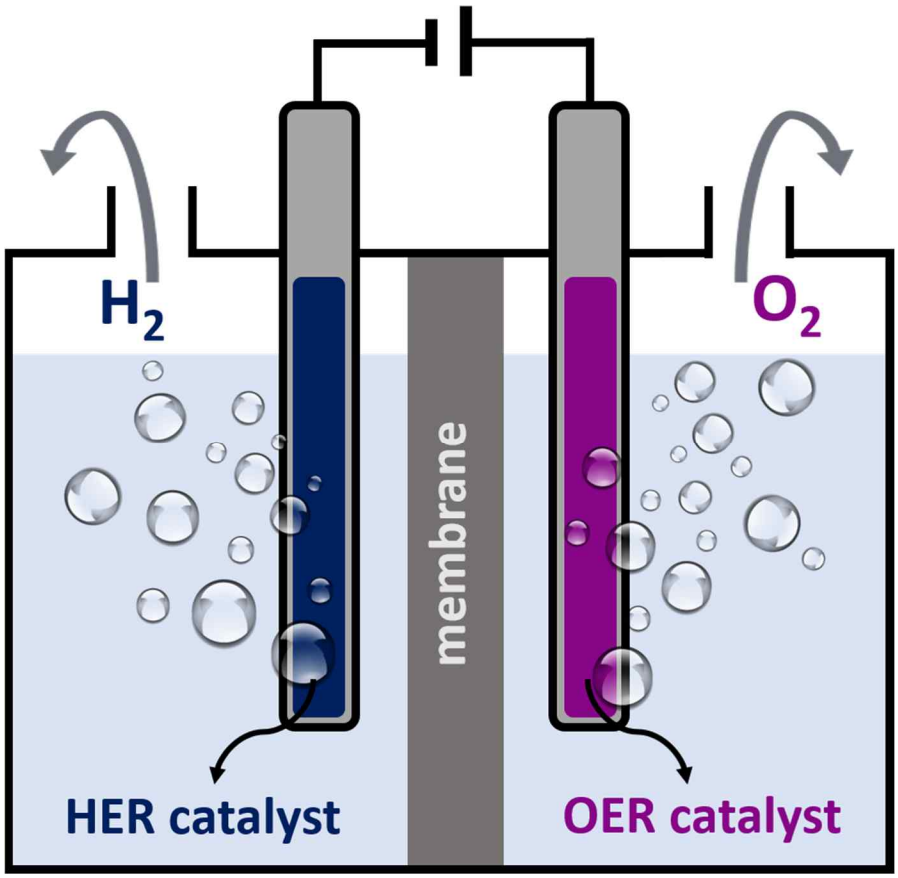

Figure 5 A schematic illustration of water electrolysis.

1.1.1 Hydrogen evolution reaction (HER)

HER is reduction of water that occurs on the surface of the cathode of a water electrolyzer. The reaction mechanism slightly differs depending on the pH of the electrolyte solution. In acidic electrolyte, HER proceeds as equations below. [20]

$$H^+ + e^- \rightarrow H_{ads} \quad (1)$$

$$H_{ads} + H^+ + e^- \rightarrow H_2 \quad (2)$$

$$2H_{ads} \rightarrow H_2 \quad (3)$$

In the above equations, H^+, H_{ads}, H_2, and e^- represent proton, adsorbed hydrogen intermediate, hydrogen gas, and electron, respectively. Each equations are assigned to the famously known Volmer (1), Heyrovsky (2), and Tafel (3) steps of the HER kinetics. [21] In alkaline electrolyte, HER follows the mechanism below. [22]

$$H_2O + e^- \rightarrow H_{ads} + OH^- \quad (4)$$

$$H_{ads} + H_2O + e^- \rightarrow H_2 + OH^- \quad (5)$$

$$2H_{ads} \rightarrow H_2 \quad (6)$$

In the above equations, H_2O and OH^- represent water and hydroxide species, respectively. Note that subsequent to the Volmer step, hydrogen gas formation may occur via either Heyrovsky or Tafel reactions. Volmer

is a discharge reaction where an electron transfers to the electrode and couples with a proton to yield an adsorbed hydrogen on an active site of the electrode. In acidic electrolyte, the hydronium cation H_3O^+ is the proton source while in alkaline electrolyte it is the water molecule. Since water molecules require higher energy for a proton to break away than the hydronium, the 'water dissociation step' represented in equation (4) brings down the reaction efficiency of alkaline HER compared to that of acidic HER.

1.1.2 Oxygen evolution reaction (OER)

OER is oxidation of water occurring on the anode of the electrolyzer. Due to the complexity of the reaction mechanism, the rate-determining step (RDS) has not been fully defined yet. The reaction mechanism of OER also slightly differs depending on the type of electrolyte. In acidic media, OER follows the equations below. [23,24]

$$2H_2O \rightarrow OH_{ads} + H_2O + H^+ + e^- \quad (7)$$

$$OH_{ads} + H_2O \rightarrow O_{ads} + H_2O + H^+ + e^- \quad (8)$$

$$O_{ads} + H_2O \rightarrow OOH_{ads} + H^+ + e^- \quad (9)$$

$$OOH_{ads} \rightarrow O_2 + H^+ + e^- \quad (10)$$

In the above equations, OH_{ads}, O_{ads}, OOH_{ads} and O_2 represent adsorbed hydroxide, adsorbed oxygen intermediate, adsorbed oxyhydroxide, and

oxygen gas, respectively. Alkaline OER follows the equation below. [24]

$$4OH^- \rightarrow OH_{ads} + 3OH^- + e^- \quad (11)$$

$$OH_{ads} + 3OH^- \rightarrow O_{ads} + 2OH^- + H_2O + e^- \quad (12)$$

$$O_{ads} + 2OH^- \rightarrow OOH_{ads} + OH^- + e^- \quad (13)$$

$$OOH_{ads} + OH^- \rightarrow O_2 + H_2O + e^- \quad (14)$$

In similarity to the slow alkaline HER kinetics, OER in acidic electrolyte is slower than in alkaline electrolyte due to the addition of water dissociation step.

1.1.3 Overall water electrolysis

In summation of the aforementioned HER and OER equations, overall water electrolysis is expressed in the equations below.

In acidic electrolyte:

HER $2H^+ + 2e^- \rightarrow H_2 \quad E^o = 0.000$ V (14)

OER $2H_2O \rightarrow O_2 + 4H^+ + 4e^- \quad E^o = 1.23$ V (15)

Overall $2H_2O \rightarrow 2H_2 + O_2 \quad E^o = 1.23$ V (16)

In alkaline electrolyte:

HER $2H_2O + 2e^- \rightarrow H_2 + 2OH^- \quad E^o = -0.83$ V (17)

OER $4OH^- \rightarrow O_2 + 2H_2O + 4e^-$ $E^o = 0.40$ V (18)

Overall $2H_2O \rightarrow 2H_2 + O_2$ $E^o = 1.23$ V (19)

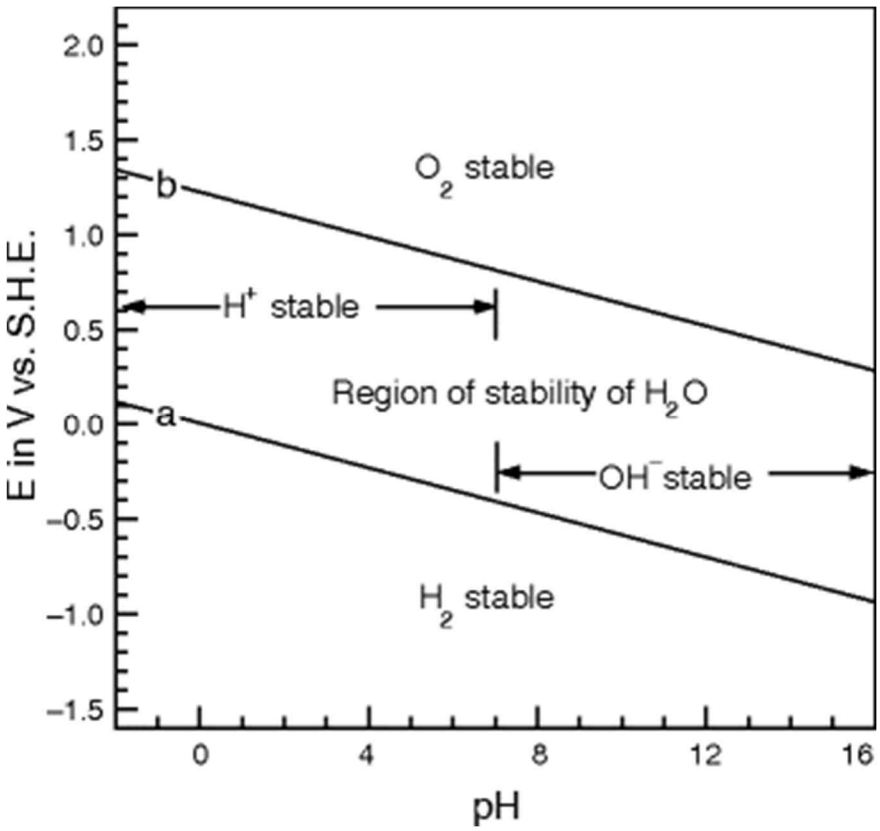

Figure 6 Pourbaix diagram of water at 25 °C. [25]

The potential-to-pH relationship is depicted in the Pourbaix diagram of water that shows a plot of thermodynamically stable phases oxygen, hydrogen, and equilibrium regions for water (Figure 6).

1.2 Transition metal-based catalysts

There exists a dilemma in selecting the electrolyte as HER and OER mechanisms favor contradicting pH. It is worthy to note that OER involves four electrons while HER only requires two electrons in both pH conditions, resulting in relatively sluggishness in OER. It must be considered that the intrinsically sluggish OER kinetics will worsen in acidic media. Moreover, another clear downside of acidic media lies in limited catalyst options. Due to the highly corrosive nature of acid electrolyte, catalyst selection is restricted to platinum group metals such as ruthenium (Ru), rhodium (Rh), palladium (Pd), osmium (Os), iridium (Ir), and platinum (Pt) that have high chemical resistance. Although these platinum group metals have been extensively researched in the past and shown sufficient water electrolysis performances (Table 1), their scarcity, high cost, and dissolution issues at high oxidative potentials makes them unpractical catalysts. [26–28] For these reasons, alkaline water electrolysis is considered more favorable for actual sustainable production of hydrogen.

Table 1 Summary of platinum group-based catalysts for water electrolysis.

Catalysts	**HER overpotential at 10 mA·cm^{-2} (mV)**	**OER overpotential at 10 mA·cm^{-2} (mV)**	**Cell voltage at 10 mA·cm^{-2} (V)**	**Electrolyte**	**Reference**
IrW nanodendrites	12	301	1.47 (0.5 M H_2SO_4)	0.1 M $HClO_4$	[29]
IrNi NCs		300	1.58	0.5 M H_2SO_4	[30]
$IrCo_{0.65}ND_s$	17	281	1.59	0.1 M $HClO_4$	[31]
IrNiCo PHNC	68	309	1.56 (2 mA·cm^{-2})	0.5 M H_2SO_4	[32]
$Pt_{62}Co_{23}/Ir_{15}$FBNWs/C	14	308	1.53	0.1 M $HClO_4$	[33]
Co-RuIr	14	235	1.52	0.1 M $HClO_4$	[34]
Rh_2P	5.4 (5 mA·cm^{-2})	510 (5 mA·cm^{-2})		0.5 M H_2SO_4	[35]
Rh_xP/NPC	19	330		0.5 M H_2SO_4	[36]

In case of alkaline water electrolysis, earth abundant and cost effective transition metals are freely utilized as catalyst materials.

Transition metals are a group of elements with partially filled d orbitals, defined by IUPAC as "*An element whose atom has an incomplete d sub-shell, or which can give rise to cations with an incomplete d sub-shell".* [37,38] Figure 7 shows the Sabatier principle expressed in volcano plots for HER and OER. In the case of HER, the metal-hydrogen (M-H) bond strength was used as the x-axis and the logarithm of the exchange current densities ($\log j_0$) as the y-axis. This volcano-like curve enables a quick comparison of the catalytic activities of different metals. It however cannot be a completely reliable representation of the metallic activities as it is only based on observations in acidic media and does not consider activities in different solution pH. Regarding the volcano plot for OER, the activity for oxygen generation on transition metal oxide surfaces in acidic and basic media was plotted by using the overpotentials measured at 0.1 mA cm^{-2} as y-axis and the heat of transition between lower and higher metal oxides as x-axis.

These plots indicate that those elements occupying the top area of the peak are likely to exert better electrochemical performances toward water electrolysis. Leaving out the noble metals for cost and scarcity issues, Ni, Co, or Fe appear promising. Past research and articles also

suggest that among the transition metal candidates, Ni, Co. and Fe show better potential for water electrolysis than most.[39] Nevertheless, alternative transition metals including Cu, Zn, Mn, Mo, Cr, Sn, and more have been explored for water electrolysis.[40–42] Table 2 shows a list of previously reported transition metal-based catalysts for water electrolysis.

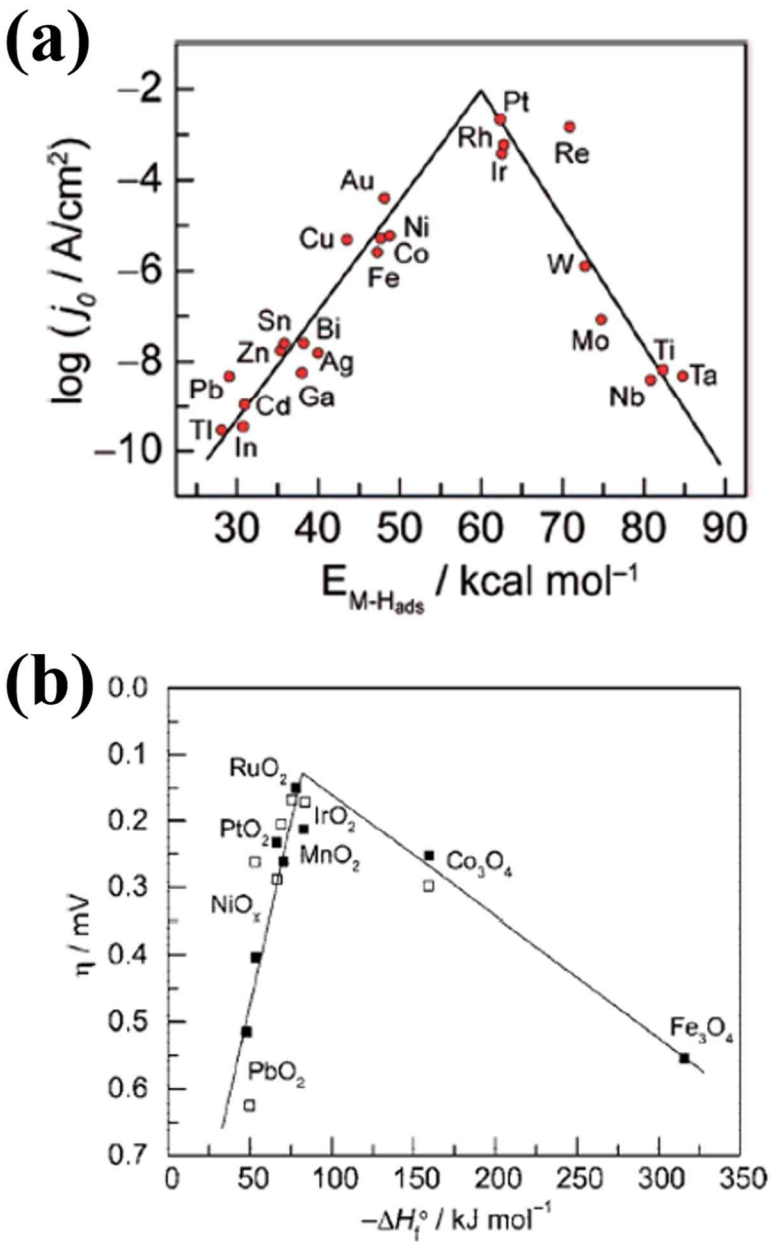

Figure 7 (a) Volcano plot for HER on metal electrodes in acidic electrolyte. (b) Volcano plot for OER on metal oxide surfaces in (■) acidic and (□) basic solutions. X-axis represents overpotentials measured at 0.1 mA cm^{-2}.[28]

Table 2 Examples of transition metal-based catalysts for water electrolysis.

Catalysts	Electrolytes	Cell voltage at 10 mA·cm^{-2} (V)	Reference
(Ni, Fe)S_2@MoS_2	1.0 M KOH	1.56	[43]
Ni-Fe-P/NF_{30}	1.0 M KOH	1.58	[44]
$NiFe_2O_4$/VACNT	1.0 M KOH	1.72	[45]
NP-$NiCo_2O_4$	1.0 M KOH	1.63	[46]
NCT-$NiCo_2S_4$	1.0 M KOH	1.60	[47]
FeCoNi@FeNC	1.0 M KOH	1.63	[48]
Cr-doped FeNi-P/NCN	1.0 M KOH	1.50	[49]
PO-Ni/NieN-CNFs	1.0 M KOH	1.69	[50]
Mo/Mn-Ni_xS_y/NF	1.0 M KOH	1.49	[51]
(Co:W:Cu) oxide	0.1 M KOH	1.80	[52]
CoP/MoP@NC/CC	1.0 M KOH	1.71	[53]
CoNi/$CoFe_2O_4$/NF	1.0 M KOH	1.57	[54]
CoN_x@GDY NS/NF	1.0 M KOH	1.48	[55]
CVN/CC	1.0 M KOH	1.64	[56]

1.2.1. Strategies for developing transition metal-based catalysts

In order to substitute the pre-existing platinum group-metal catalysts with relatively inferior transition metal-based catalysts, advanced engineering is required to bring up the catalytic activity. Here we introduce a few of the major tactics.

The first engineering tactic is coupling with non-metallic counterparts such as O, N, C, B, P, S, and Se. Such combination helps adjust the surface energy and the crystallinity of the catalysts to maximize the catalytic activities. For this reason, the reported transition metal based catalysts are seldom used in their pristine metallic form, but rather combined with non-metallic counterparts to form compounds such as transition metal oxides, hydroxides, oxyhydroxides, nitrides, oxynitrides, carbides, phosphides and so on. [40,56–66] Each compound has unique and distinctive properties and by comparing the electrochemical performances and calculated adsorption energy (density function theory (DFT)), it can be inferred that there exists some level of hierarchy among the catalysts. However, the actual catalytic performance is also greatly influenced by other factors such as gas desorption efficiency, hydrophilicity, turnover frequency (TOF), and structural integrity.[67] It is therefore difficult to determine the exact magnitude of catalytic

efficiency of the catalytic compounds.

Another engineering tactic that has been receiving growing attention is doping or mixing of a secondary or even tertiary transition metal to form a multi-metallic system. [68–70] This approach aims in the disruption of catalyst crystallinity via inclusion of foreign metals for optimal adsorption of H^+ and OH^-. The catalytic properties differ in almost every elemental composition ratio of the catalysts and therefore optimization requires extensive empirical studies.

Forming a composite with various graphitic and amorphous carbons such as carbon nanotubes and graphene is another widely used tactic.[40] The incorporation of carbon can enhance electrical conductivity, overall surface area, interaction with the electrolyte, and structural integrity. The aforementioned tactics are most often used collectively to bring out the utmost activity of the catalyst. In the attempt to incorporate all the above-mentioned tactics, catalyst design can become quite complex.

Metal organic frameworks (MOFs) however may hold the key to solve this complexity. Recently, advanced materials derived from metal organic frameworks (MOFs) through post-treatments such as calcination immerged as candidate materials with unimaginable opportunities.

1.2.2 Metal organic framework derived transition metal-based catalysts

Metal–organic frameworks (MOFs), a relatively young type of porous compound materials composed of metal ions regularly coordinated with organic linkers, have stimulated great research interest due to their unique properties.[71] The versatility in combination of metal ions and organic linkers has led to discovery of numerous number of MOFs. As of 2017, more than 20,000 MOFs were reported, and the number of MOFs have been growing exponentially.[71,72] The MOF structures can easily be controlled into one, two, or three-dimensions by varying the constituents. Moreover, precise control of the MOF morphology, size, and porosity is possible via diverse synthetic procedures. The ultra-high surface area (1,000 ~ 10,000 m^2 g^{-1}) MOFs offer makes them highly attractive over traditional porous materials such as zeolites or mesoporous carbons. Owing to these favorable features, MOFs have exhibited promising performances in a vast variety of applications, such as water treatment,[73] gas storage and separation,[74,75] sensors,[76] drug delivery,[77] and catalysis.[78–80].

Recently, advanced materials derived from metal organic frameworks (MOFs) through post-treatments such as calcination immerged as candidate materials with unimaginable opportunities.

The inorganic metal node and the organic linkers can serve as ideal precursors to prepare composite materials, while functioning as a structural template to control the resultant morphology. The MOF-derived materials displayed appealing performances when utilized as electrode materials in electrochemical systems. Studies indicate that MOF-derived materials fulfill several aspects required by optimized catalysts.

Firstly, the carbon matrix obtained from the organic linkers of the framework is able to serve as a highly conductive network and promote fast electron transfer.[81–85] Secondly, the metal components in MOFs can form corresponding metals or compounds and homogeneously distribute within the carbon matrix, inducing the in-situ formation of carbon frameworks uniformly decorated with transition metal/compound particles.[86–88] Third, the various features of the precursor MOFs (structure, size, morphology, porosity) can be preserved in the resulting materials after post-treatments.[89–91] Fourth, various non-metallic heteroatoms (e.g., O, S, N, P) confined in the organic linkers can be in-situ doped into the carbon matrix and create more active sites and also provide favorable environment for the growth of catalyst compounds such as transition metal oxides, nitrides, and carbides.[92–95] Fifth, and lastly, multiple transition metals can be easily inserted into the MOF and

produce multi-metallic catalyst of desired composition upon post-treatment.[96–98]

Owing to the advantages discussed above, the MOF-derived materials rose as promising designing tools for transition metal-based electrocatalysts. Some MOF-derived electrocatalysts have shown significantly enhanced performances comparable to the noble-metal-based electrocatalysts. Table 3 and 4 shows a list of previously reported MOF-derived transition metal-based catalysts for HER and OER, respectively.

Table 3 Summary of MOF-derived catalyst materials for HER.

Catalyst	MOF	Electrolyte	HER overpotential at 10 mA·cm^{-2} (mV)	Tafel slope [mV dec^{-1}]	Ref.
PtFeCo@CN	$Co_3[Fe(CN)_6]_2$	0.5 m H_2SO_4	45	32	[99]
MoCN-3D	ZIF-8	0.5 m H_2SO_4	89	51.4	[100]
		1 m KOH	122	78.4	
MoC_x nano-octahedrons	NENU-5	0.5 m H_2SO_4	142	53	[101]
		1 m KOH	151	59	
Mo_2C/C	MIL-53 (Al)	1 m KOH	165	63.6	[102]
MoS_2/3D-NPC	Al–PCP	0.5 m H_2SO_4	210	51	[103]
Fe_3C/Mo_2C@NPGC	MIL-100 (Fe)	0.5 m H_2SO_4	98	45.2	[104]
$Zn_{0.3}Co_{2.7}S_4$	Zn,Co–ZIF	0.5 m H_2SO_4	80	47.5	[105]
Ni_2P	Ni–BTC	0.5 m H_2SO_4	172	62	[106]
CoPd@NC	$Co_3[Co(CN)_6]_2$	0.5 m H_2SO_4	80	31	[107]
CoP_3	ZIF-67	0.5 m H_2SO_4	78	53	[108]
CoP hollow polydedrons	ZIF-67	0.5 m H_2SO_4	159	59	[109]
nanoMoC@GS(700)	$Mo_3(BTC)_2$	0.5 m H_2SO_4	132	46	[110]
CoP/rGO-400	ZIF-67	0.5 m H_2SO_4	105	50	[111]
		1 m KOH	150	38	
CoP CPHs	ZIF-67	0.5 m H_2SO_4	133	51	[112]
$Co_{0.59}Fe_{0.41}P$	Co/Fe–PBAs	0.5 m H_2SO_4	72	52	[113]

Table 4 Summary of MOF-derived catalyst materials for OER.

Catalyst	**MOF**	**Electrolyte**	**OER overpotential at 10 mA·cm^{-2} (mV)**	**Tafel slope [mV dec^{-1}]**	**Ref.**
Co_3O_4@C–MWCNTs	ZIF-9	1 m KOH	320	62	[114]
CoP/rGO-400	ZIF-67	1 m KOH	340	66	[111]
Co_3O_4C–NA	Co-naphthalene-dicarboxylate	0.1 m KOH	290	70	[85]
Ni1Co_4S@C-1000	ZIF-67	0.1 m KOH	280	64	[115]
Co–CNT–PC	ZIF-67	0.1 m KOH	315	73.8	[116]
Co–MOF@CNTs (5 wt%)	$Co(PhIm)_2·(DMF)·(H_2O)$	1 m KOH	340	69	[117]
CoP hollow polydedrons	ZIF-67	1 m KOH	400	57	[109]
Zn-doped $CoSe_2$/CFC	Zn,Co–ZIF	1 m KOH	356	88	[118]
FeNi@N–CNT	Zn/Fe/Ni–ZIF	1 m KOH	300	47.7	[119]

1.3 Perspective and outlook

To date, a variety of TMN/TMON have been reported as promising catalyst materials for water electrolysis. To optimize the catalytic performance, synthetic strategies such as morphological structure design and electronic-structure manipulation has been actively studied. Most recently, MOFs arose as a promising method for catalyst design owing to the high surface area and cage-like pores that can effectively isolate metal components. The typical 3D structure and porosity of MOFs are attractive features of MOF-derived TMN/TMONs for their significant improvement in active sites access and charge transfer rate. Although some recently emerged MOF-derived TMN/TMON nanocatalysts have achieved remarkably improved performance in electrolysis compared to the previous reports, some challenges remain for future exploration of more advanced MOF-derived TMN/TMON electrocatalysts. In perspective of synthesis, the conventional synthetic strategies for MOFs are often unsatisfactory in terms of scalability and universality. For instance, only several typical MOFs in their standard forms (such as ZIF-67 or MIL-88B-NH3) have been investigated as precursors/templates for catalyst synthesis despite the extensive number of reported MOFs. It is expected that further expansion of materials design strategies will lead to the discovery of extensive amount of novel

electrocatalysts.

Another emerging strategy for catalyst optimization is electronic structure alteration via heteroatom doping and alloying. This approach is rapidly bringing up the catalytic performance of recently reported catalysts. Heteroatom doping (both metal and nonmetal) can induce better electrochemical performance via shifting of the d-band and oftentimes formation of more active sites. The multi-metal nitrides containing two or more metals alloyed together often possess the distinctive properties of each monometallic nitride and enable bifunctional activities for electrocatalysis. However, the approaches to achieve such alloyed metal nitrides can be complex and the precise composition difficult to harness. Remarkably, MOFs can be easily engineered in composition by simply incorporating hetero-components in the coordination stage as either metal nodes or organic linkers. Such component modulation may generate pathways for large-scale synthesis of novel TMN/TMONs that are unachievable by traditional pathways.

While the chemical inertness of TMN provide stability during electrochemical reactions, it may also be related to the shortage of active sites for electrochemical reactions. Thus, efficient methods to modify TMNs are needed. In this context, this thesis aims to explore some of the efficient catalyst modification methods and understand the

underlying mechanisms of TMN/TMONs in water electrolysis, in order to guide the synthesis of future materials. Further exploration of the modifications dependent mechanism with the help of theoretical and experimental characterizations will help define the optimal catalyst conditions and realize catalysts with industry-level performances in water electrolysis.

1.4 Dissertation overview

Three ways of improving the catalytic performance of transition metal-based catalysts are reviewed in the following two studies; 1) MOF-guided structure and morphology control; 2) introduction of secondary transition metal for optimal catalyst crystallinity; 3) nitridation for enhanced chemical stability and electrical conductivity. These approaches have proven effective for enhancement of water electrolysis over the course of electrochemical analysis.

The first study demonstrates a structural and electrochemical design of copper-based OER catalyst by controlling the growth kinetics of the precursor MOF and Fe doping followed by microwave-assisted nitridation. The growth kinetics of MOF could be controlled using solvent-dependent change in dissolution rate of the copper source and the deprotonation rate of organic linker. As a result of this study, exquisite urchin-shaped MOFs were obtained in aqueous medium, unlike most previously reported methods for CuMOF synthesis that use toxic DMF as solvent. Iron was chosen as the secondary metal dopant considering its previously reported excellent catalytic activity and abundance. Iron was successfully incorporated into the urchin-shaped MOFs without significant morphology changes, and the final catalyst derived urchin-shaped bimetallic MOF exhibited a greatly enhanced

OER activity compared to its unmodified counterparts, exhibiting current density increase from a mere 4.25 mA to 236.32 mA at an applied overpotential of 420 mV, marking a 5460.47 % increase. The impact of nitridation on the enhanced electrocatalytic performances was confirmed by significantly increased overpotentials of comparisons prepared in the absence of ammonia source.

The second study introduces a simple and energy-efficient synthesis route for MOF-derived FeMoON bifunctional catalyst and conduct in-depth study of its properties. MIL-88B synthesized via rapid microwave process served as the precursor MOF and the thermally transformed catalysts featured 5-10 nm nanoparticles confined in the initial porous microstructure, providing multiple active sites and pathway for electrolyte and gas transport. The effect of molybdenum incorporation and oxynitride formation on the electrochemical property and catalytic activity of FeMoON was investigated, and the results show that incorporation of Mo in optimal ratio significantly enhances the catalytic activity by tuning the sluggish Volmer step; and that N-doping significantly boosts water-splitting activity by enhancing charge transfer behavior. Two modifications combined, the optimized FeMoON alkaline water electrolyzer shows catalytic behavior surpassing that of the commercial Pt/C||RuO_2 electrolyzer (1.81 V and 1.89 V, respectively, for

current density of 100 mA cm^{-2}). Moreover, FeMoON electrolyzer could bear 1000 cycles of accelerated degradation and 20 hours of constant applied voltage without deterioration in current density, indicating good stability.

In summary, two types of bimetallic transition metal nitride/oxynitride were proposed in reaction to the ever growing demand for efficient electrocatalyst for green hydrogen production. Rapid and energy efficient synthesis methods were introduced to prepare bimetallic MOFs and their transformed bimetallic nitride/oxynitride catalysts. The resulting catalysts were closely evaluated for water electrolysis and demonstrated good performance. Based on the presented results, CuFeN/CNT and FeMoON are proposed as promising catalyst materials for water electrolysis.

Chapter 2. Bimetallic transition metal nitride/oxynitride-based catalysts for water electrolysis

Part 1. CuFeN/CNT composite derived from kinetically modulated urchin-shaped MOF for highly efficient OER catalysis

2.1.1 Motivation

Amidst the ever-growing demand for energy and rapidly deteriorating environment, sustainable energy source is in desperate need. While abundant research is being carried out to replace traditional fossil fuels, molecular hydrogen is considered as one of the most promising sustainable energy source. Electrochemical water splitting is a well-known method to produce high-purity hydrogen and oxygen via cathodic hydrogen evolution reaction (HER) and anodic oxygen evolution reaction (OER), where a water molecule breaks into hydrogen and oxygen at an applied potential of 1.23V.[120–122] However, OER in practice requires greater potential than the theoretical value due to its four-electron-associated multistep reaction which is relatively sluggish in comparison with a two-electron transfer reaction of HER.[123,124] Moreover, as current state-of-the-art catalysts are composed of costly

and scarce precious metals such as Ru and Ir, commercial implementation of the OER catalysts are greatly limited.[125,126] For this reason, considerable research efforts have been invested to develop low-cost transition metal alternatives that display comparable OER kinetics, and came to significant progress lately.[98,127–132]

Over the past few years, first row transition metals (Fe, Co, Ni) and their derivatives were widely studied for OER and achieved outstanding performance and stability; comparable or even superior to those of precious metals; while Cu based catalysts were relatively neglected. This could be owing to the intrinsic lack of stability of copper in aqueous environment and air that leads to oxidation and ion leaching of the metal itself.[133–135] However, the shortcomings in stability can be complemented by adding a dopant or a protective layer, or enhancing chemical inertness through nitridation.[136–138] Being one of the earth-abundant and inexpensive metals, copper is worth investigating for its catalytic property and structural design to maximize its advantages.[139]

Among the already existing transition metal-based electrocatalysts such as oxides, carbides, nitrides, oxynitrides, selenides, phosphides, and hydroxides, transition metal nitrides and oxynitrides (TMN, TMON) are notable for their inherently high chemical stability and conductivity.[138,140–145] A recent pioneering report on Cu_3N for

water splitting by Driess's group demonstrated catalytic activity and stability exceeding that of RuO_2 and IrO_2.[146] Sun's group reported a much enhanced electrocatalytic property by employing Ni and Cu together in a bimetallic nitride, a coinciding result to the previous reports on significantly improved OER activity upon secondary transition metal doping.[138,147,148]

Regarding structural design, metal-organic frameworks (MOFs), organic-inorganic hybrid crystalline materials with porous nanostructure and confined metal sites, are excellent candidates owing to their remarkably high surface area and flexible tunability.[129,149,150] MOFs derived nanocatalysts often proved to be highly efficient owing to the open active sites and reduced mass transfer resistance rendered by the hierarchical porosity of MOFs. More than 20,000 different MOFs have been reported so far and thousands of compounds are studied each year.[151] Each type of MOF has its own distinct properties but it should be noted that the property of MOFs do not only depend on the type of material, but also its size, shape, and microstructure.[150] Therefore, it is a necessity for modern synthetic chemistry to achieve control over the morphology of MOFs.

There are several reports on MOF morphology and size modulation methods, including template method,[151,152] sonochemical

method,[153] surfactant assisted method,[154] pH method,[155] solvent variation method,[150,156] and more. Among them, variation of solvent is perhaps the simplest tuning method that gives dramatically different size and morphology. A number of research using this approach has been carried out, including the Al-MOF morphology study in DMF/H_2O bi-solvent system from Guo's group,[157] CuMOF porosity survey in H_2O/EtOH bi-solvent system,[158] and Ni-MOF surface area investigation[159] and Co-MOF capacitance study in DMF/EtOH/H_2O tri-solvent system by Chun's group[159] and Wang's group,[150] respectively. These reports clearly demonstrated that the adequate choice of solvent or mixed solvent could greatly improve the nature of the product MOF for desirable applications. However, the reported solvent-controlled morphologies are still quite crude and unrefined. This is because the general mechanism of the solvent variation method is altering the deprotonation rate of the organic linkers, while the metal ions move freely without any constraint. Self-sacrificial template method is an efficient way of controlling the rate of metal ion release, despite the additional synthesis step. Cai et al. reported the preparation of a well-aligned MOF array using Co, Cu, Ni oxide and hydroxide nanowire array as template.[129] Zhan et al. demonstrated fabrication of ultrathin CuMOF nanosheets from copper oxide nanocubes.[151] As such,

template method enables a more meticulous manipulation of MOF morphology.

Considering these factors, we herein report a structural and electrochemical design of copper-based OER catalyst by controlling the growth kinetics of the precursor MOF and secondary metal doping followed by microwave-assisted nitridation. The growth kinetics of MOF could be controlled using solvent-dependent change in dissolution rate of both the copper source and the deprotonation rate of organic linker. Iron was chosen as the secondary metal dopant considering its previously reported excellent catalytic activity and abundance. The final catalyst derived from the morphology-controlled bimetallic MOF exhibited a greatly enhanced OER activity compared to its unmodified counterpart, exhibiting current density increase from a mere 4.25 mA to 236.32 mA at an applied overpotential of 420 mV, marking a 5460.47 % increase.

2.1.2 Experimental section

2.1.2.1 Reagents

Copper sulfate pentahydrate ($CuSO_4 \cdot 5H_2O$, 99.0%), iron chloride hexahydrate ($FeCl_3 \cdot 6H_2O$, 99.0%), and sodium citrate ($Na_3C_6H_5O_7$, 99.0%) were purchased from Sigma Aldrich. Sodium carbonate (Na_2CO_3), and glucose ($C_6H_{12}O_6$, 99.8%) were purchased from Samchun

Chemicals (South Korea). All chemicals were used without further purification.

2.1.2.2 Apparatus

The electrochemical impedance spectroscopy (EIS) was measured using ZIVE SP1. X-ray diffraction (XRD) patterns were recorded by a powder X-ray diffractometer (SmartLab, Rigaku, Japan) with a Cu target and a scan rate of $5°\cdot min^{-1}$. X-ray photoelectron spectroscopy (XPS) analysis was conducted using Axis-HIS spectrometer at constant energy of 20 eV with Al irradiation of 12 kV and 18 mA.

2.1.2.3 Preparation of Cu_2O nanoparticles

Briefly, 1.5 mmol sodium citrate, 0.24 mmol sodium carbonate, 0.68 mmol $CuSO_4 \cdot 5H_2O$, and 2 mmol glucose were dissolved in 15 mL H_2O, followed by addition of 15 mL EtOH into the solution. The homogeneous clear blue solution was then placed into a domestic microwave oven (Samsung MS23F301TAR, 700 W). After microwave irradiation for 60 seconds, bright orange solution of Cu_2O nanoparticles was obtained. After cooling in cold water bath, the sediments were centrifuged and washed with H_2O/EtOH three times. The obtained bright orange precipitate was dried in a vacuum oven.

2.1.2.4 Preparation of CuFeO nanoparticles

Identical procedure to the preparation of Cu_2O nanoparticles described above was used, except that 10, 30, 50, 70, and 90 mol % of 0.68 mmol $CuSO_4 \cdot 5\ H_2O$ was replaced with $FeCl_3 \cdot 6\ H_2O$. The color of the obtained precipitates grew darker as the mol % of Fe salt increased.

2.1.2.5 Preparation of CuMOF urchins (CuMOF-H_2O)

50 mg Cu_2O and excessive amount of H_2BDC was first dispersed in 30 mL H_2O, then placed into a domestic microwave oven. After microwave irradiation for 120 seconds, the color of the solution changed from whitish orange to turbid yellow. The obtained solution was cooled in cold water bath, then stirred for three hours in open air at room temperature. The solution gradually changed its color from turbid yellow to whitish green and finally to whitish blue over the first hour. After full conversion of Cu_2O into CuMOF, the sediments were centrifuged and washed once with DMF and twice with H_2O/EtOH mixture. CuMOF-DMF sheets and CuMOF-EtOH core-shell structures were prepared with by replacing the 30 mL H_2O with DMF and EtOH, respectively.

2.1.2.6 Preparation of CuFeMOF urchins

Identical procedure to the preparation of CuMOF urchins described above was used, except that Cu2O was replaced with CuFeO-10, CuFeO-30, CuFeO-50, CuFeO-70, and CuFeO-90 nanoparticles.

2.1.2.7 Preparation of CuMOF/CNT/NH_4HCO_3 sponge

The above CuMOF urchins were first dispersed in 5mL 0.2 wt. % CNT aqueous solution, followed by addition of 5 mL 2.5 M NH4HCO3 aqueous solution. The mixture was vortexed vigorously and quickly subjected to liquid nitrogen, followed by lyophilization. Oxidized CNT was prepared via acid-treatment as described in literature.[160]

2.1.2.8 Preparation of CuFeMOF/CNT/NH_4HCO_3 sponge

Identical procedure to the preparation of CuMOF/CNT/NH4HCO3 sponge described above was used, except that CuMOF urchins were replaced with CuFeMOF-10, CuFeMOF-30, CuFeMOF-50, CuFeMOF-70, and CuFeMOF-90.

2.1.2.9 Preparation of CuN/CNT catalysts

For the preparation of CuN/CNT catalyst, the CuMOF/CNT/NH4HCO3 sponge was placed in a crucible together with

a piece of carbon cloth, and then was enclosed in a 100 mL vial inside an Ar filled glovebox. The vial was placed into a domestic microwave and irradiated for 30 seconds to prepare CuN/CNT composite.

2.1.2.10 Preparation of of CuFeN/CNT catalysts

Identical procedure to the preparation of CuMOF/CNT/NH_4HCO_3 sponge described above was used, except that CuMOF/CNT/NH_4HCO_3 sponge was replaced with CuFeMOF/CNT/NH_4HCO_3 sponges described above

2.1.2.11 Electrochemical measurements

Electrochemical measurements were performed utilizing Autolab potentiostat (Metrohm, Netherlands). All electrochemical tests were performed in a typical three-electrode setup in 1 M KOH. The as-prepared catalysts, Hg/HgO electrode and graphite rod were used as working, reference and counter electrode, respectively. Typical preparation of the working electrodes is as follows: 5mg catalyst dispersed in 980 μL ethanol with 20 μL Nafion solution and sonicated for 30 minutes to give a homogeneous ink. Then 200 μL of the as-prepared ink was drop-casted onto 1 cm^2 nickel foam (NF) and dried under an IR lamp. The RuO_2 reference material was identically prepared

on NF. All the LSV profiles were measured at a scanning rate of 5 mV s^{-1} and were iR corrected. The interfacial charge-transfer resistance (Rct) of the analytes was investigated using EIS. The EIS measurements were carried out from 0.1 to 100 kHz at a potential of 1.65 V vs. RHE with an amplitude of 10 mV. Cycling stability was tested by observing LSV polarization curve before and after 1,000 continuous CV cycles at a scan rate of 100 mV s^{-1}. Long-term stability was evaluated using chronopotentiometry at a constant current density of of 50mA cm^{-2}. Electrochemical impedance spectroscopy (EIS, ZIVE SP1) was conducted within the frequency range of 10^{-2} to 10^{5} Hz at 1.65 V. The electric potentials in all the presented electrochemical data have been converted to the reversible hydrogen electrode (RHE) scale according to Nernst equation: $E_{RHE} = E_{Hg/HgO} + 0.059 \cdot pH + 0.14$.

2.1.3 Results and discussion

Figure 8 depicts a schematic diagram of robust microwave-assisted process for the preparation of CuFeN/CNT electrocatalysts. The bimetallic CuFeN/CNT catalyst was realized after optimizing the synthesis condition of single metallic CuN/CNT and its precursor (CuMOF). A schematic illustration of CuMOF morphology control is presented in Figure 9.

To begin with, quasi-spherical Cu_2O nanoparticles with an average size of ~500 nm were synthesized by mixing copper salt with sodium citrate, sodium carbonate, and glucose as surfactant, pH regulating agent, and reducing agent in ethanol/water solution followed by brief microwave irradiation, as illustrated in Figure 9. Note that the synthesis process is green by employing non-toxic reagents and energy efficient microwave heating method. The acquired Cu_2O template particles were dispersed in H_2BDC solutions with different solvents then briefly irradiated with microwave to aid quick nucleation on the surface of the templates. The irradiated solutions were then stirred until completion of growth, which was evident by the color change of the mixture from orange to yellowish green, then to blue. It is noteworthy that the role of brief microwave irradiation is quite significant as MOF growth takes more than 24 hours in its absence. Moreover, large spindle-shaped MOFs are obtained

instead of urchin-shaped MOFs when grown without microwave irradiation. The morphology and composition of the as-prepared CuMOFs were fully characterized by XRD, SEM, and TEM. Figure 10 shows SEM images and optical images of the time dependent growth of CuMOF in DMF, ethanol, and water. Within the first hour, the Cu_2O templates show significant morphology changes in DMF and water implying MOF formation while only small MOF crystals are observed on the surface of the Cu_2O template in ethanol. Thin sheet-like morphology is observed for MOF in DMF while a sea urchin-like structure is observed in water. After three hours of growth, smaller sea urchin-like structure is observed in ethanol growth solution, while the MOFs in DMF and water undergo no significant change from the first hour. From the color changes of the growth solution as shown in the right column of Figure 10, it can be seen that transformation commences within the first hour in DMF and H_2O as the color changes to green and yellow, respectively, and comes to completion after 3 hours as no further color change is observed after 5 hours. However, no significant color change is spotted in the ethanol growth solution, implying that transformation may have occurred limited to the surface while the template remains in the core. In order to confirm the degree of

conversion and purity of the as-synthesized CuMOFs, X-ray powder diffraction (XRD) was analyzed.

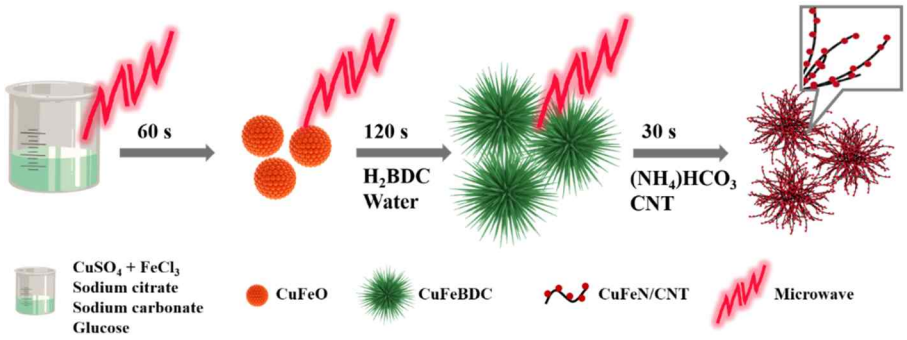

Figure 8 A schematic illustration of the overall formation process of CuFeN/CNT.

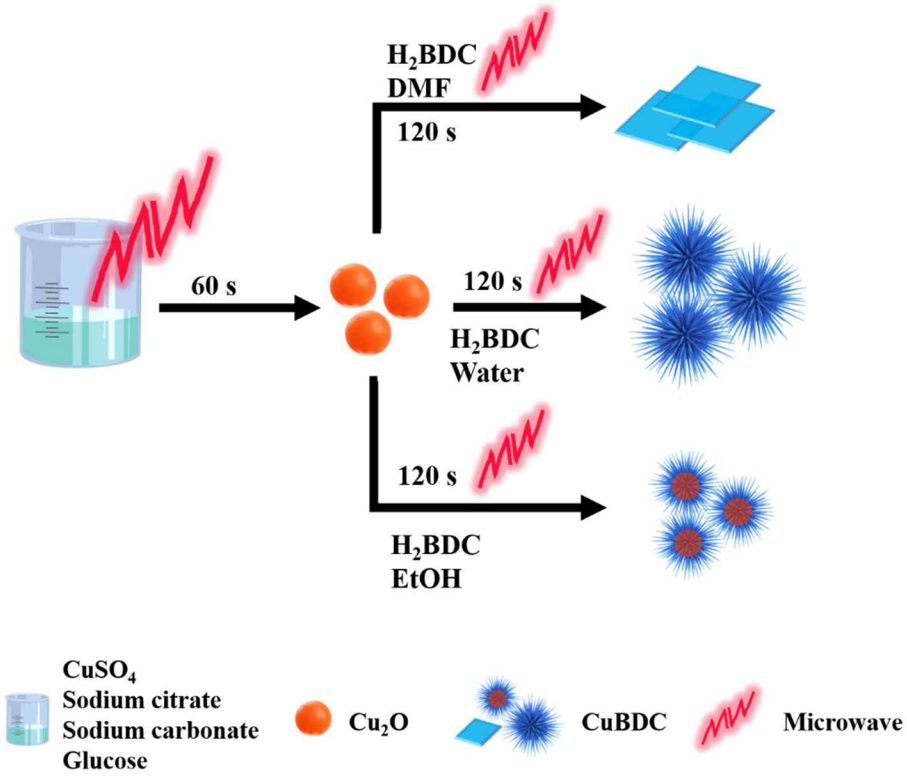

Figure 9 Growth of Cu2O templated CuMOFs in different solvents.

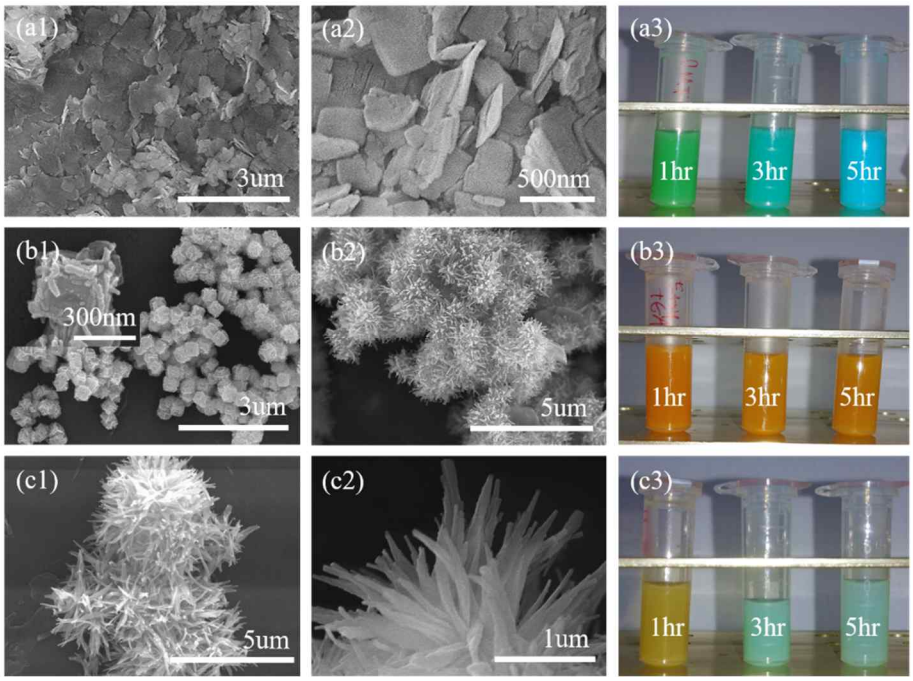

Figure 10 SEM images of CuMOF grown in (a) DMF, (b) EtOH, (c) H_2O after 1 hour (a1, b1, c1) and 3 hours (a2, b2, c2). Optical images of CuMOF growth solution in (a3) DMF, (b3) EtOH, and (c3) H_2O at 1 hour, 3 hours, and 5 hours.

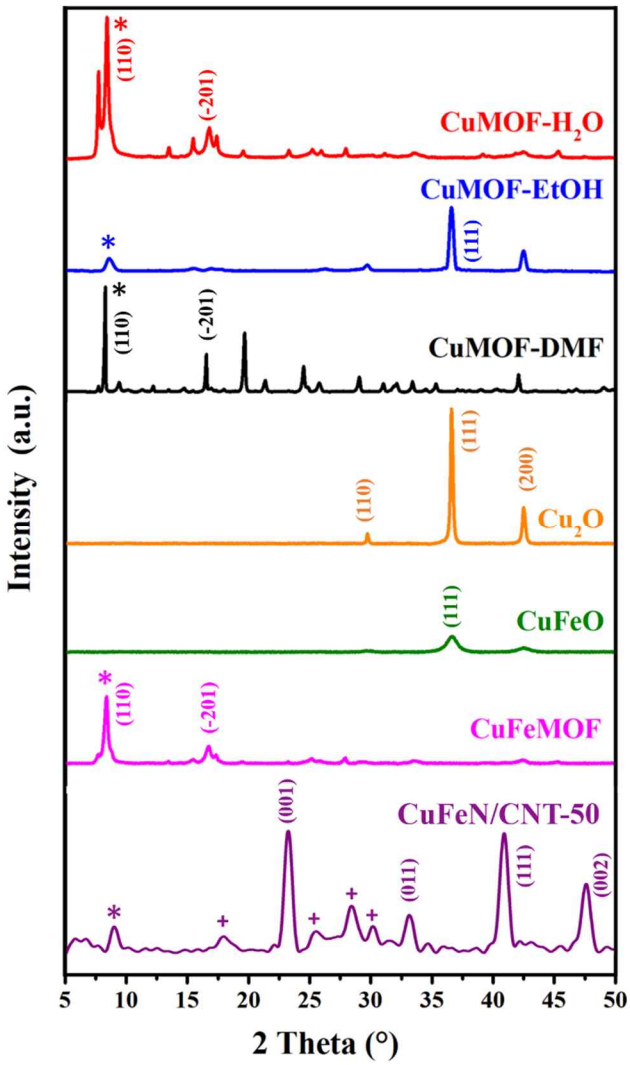

Figure 11 XRD patterns of CuMOF-H_2O, CuMOF-EtOH, CuMOF-DMF, Cu_2O, CuFeO, CuFeMOF, and CuFeN/CNT-50 from top to bottom (* CuMOF, + Triuret).

Figure 11 shows XRD patterns of CuMOF grown in DMF, EtOH, and H_2O for 3 hours. The sharp and clear diffraction peaks shown in CuMOF-H_2O and CuMOF-DMF samples indicate good crystallinity of the prepared MOFs. The prominent peaks at around 8 and 17° are the typical peaks of Cu-BDC MOFs respectively assigned to (110) and (-201) planes, which are in in good agreement with previously reported diffraction pattern of desolvated CuMOF.[161,162] CuMOF-EtOH sample on the other hand exhibits very weak CuMOF peaks and sharp Cu_2O diffraction peaks at ~30, 36, and 43° respectively assigned to (110), (111), and (200) planes, confirming the Cu_2O core-MOF thorny shell hypothesis. TEM analysis of CuMOFs grown in different solvent conditions are also in agreement with the above conclusion, showing transparent urchin and sheet-like structure for H_2O and DMF growth solvents and dark opaque core covered in transparent thorny shell-like morphology for EtOH growth solvent (Figure 12).

Such difference in morphology and composition of CuMOF grown in different solvents is endowed to oxidative dissolution rate of copper oxide particle and deprotonation rate of H_2BDC in each solvent. Dissolution of copper oxide particle goes through gradual oxidative release of Cu^+ from the surface of the particle followed by oxidation of Cu^+ into Cu^{2+} by the dissolved oxygen.[151] It is known that copper is

easily oxidized in aqueous medium and remains relatively stable in organic solvents.[133,163–166] On the other hand, solubility of H_2BDC is dependent on the solvent's ability to deprotonate. Therefore, H_2BDC readily deprotonates in DMF with high Brønsted basicity and shows low dissolution in relatively acidic water and ethanol.[167] It is clear that faster conversion rate of Cu_2O to MOF in H_2O and DMF over EtOH is due to faster coordination between Cu^{2+} and BDC^{2-} from active Cu^{2+} leaching in H_2O and rapid H_2BDC deprotonation in DMF. The different MOF shapes resulting from different growth solvent comes down to two possible reasons: (1) change in MOF network such as obstruction of CuMOF coordination caused by coordination with solvent molecules, and (2) solvent dependent change in morphology of the intermediate phase of copper source. The following models are proposed as possible dissolution routes of cuprite.

$$Cu_2O + 2\ H^+ \rightleftharpoons 2\ Cu^+ + H_2O \quad (1)$$

$$Cu_2O + H_2O \rightleftharpoons 2\ CuOH \quad (2)$$

$$2\ CuOH + H_2O + ½\ O_2 \rightleftharpoons 2\ Cu(OH)_2 \quad (3)$$

$$2\ Cu(OH)_2 + 4\ H^+ \rightarrow 2\ Cu^{2+} + 4\ H_2O \quad (4)$$

$$Cu_2O + ½\ O_2 \rightleftharpoons 2\ CuO \quad (5)$$

$$CuO + 2\ H^+ \rightleftharpoons Cu^{2+} + H_2O \quad (6)$$

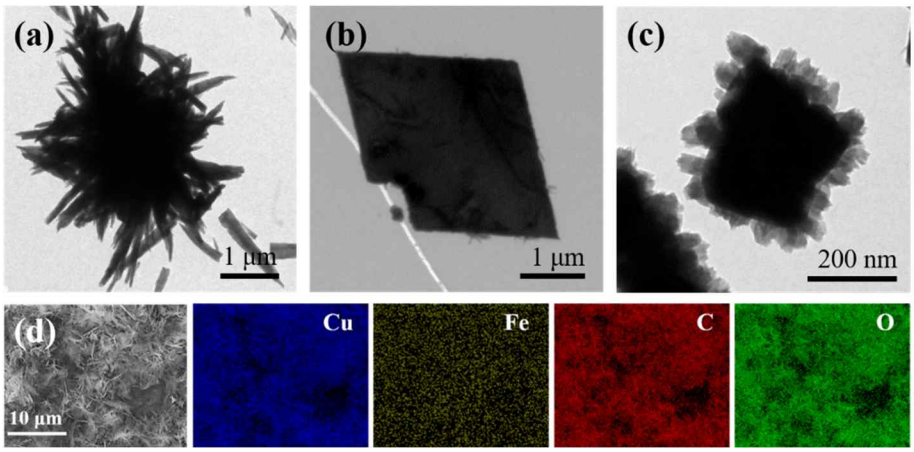

Figure 12 TEM image of (a) CuMOF-H_2O, (b) CuMOF-DMF, (c) CuMOF-EtOH, and (d) EDX elemental mapping of CuMOF-H_2O.

According to literature, neutral species such as $Cu(OH)_2$ and Cu(OH) are dominant over copper ion species in mildly alkaline conditions at ambient temperature.[163] Considering the anisotropic nature of copper hydroxides that usually grow into platelets or spindle-shaped morphology, formation of the urchin-shaped CuMOFs may be explained by a theory that it arose from the hydroxide intermediate phase in mildly alkaline water and ethanol growth solutions. Moreover, the conformity in the XRD spectra between CuMOF-H_2O and CuMOF-DMF disproves dramatic obstruction of metal-linker coordination. However, this theory cannot be completely discarded because of the strong peak at 7.6 degree that appears only in XRD spectra of CuMOF-H_2O. Additionally, Cu_2O templated CuMOF growth in H_2O/DMF mixed solvent was also observed. The transition took place immediately after microwave heating process due to rapid coordination between free Cu ions swimming in water and active ligands deprotonated in DMF, resulting in large box-shaped layered MOF crystals within a few minutes (Figure 13).

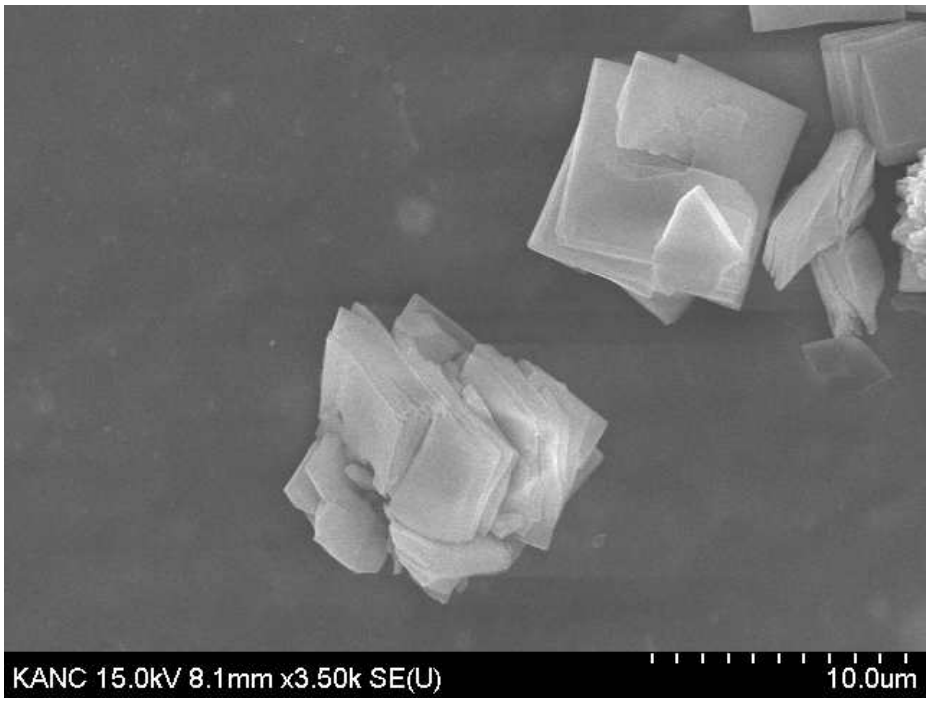

Figure 13 SEM image of CuMOF-H_2O/DMF.

The as-prepared CuMOF MOFs in four different morphologies were integrated with CNT and underwent microwave assisted thermal process in ammonia rich media to form Cu_3N/C-DMF, Cu_3N/CNT-H_2O, Cu_3N/CNT-EtOH, and Cu_3N/CNT-H_2O/DMF catalysts. The collected catalysts were tested for electrocatalytic performance and properties toward OER (Figure 14). As expected, CuMOF-H_2O derived Cu_3N/CNT-H_2O showed noticeably enhanced catalytic performance compared to that of Cu_3N/C-DMF, Cu_3N/CNT-EtOH, and Cu_3N/CNT-H_2O/DMF, showing that the morphology of the precursor MOF has a significant impact on catalytic property. We speculate that the thorny MOF structure with large specific surface area enables faster nucleation leading to formation of smaller catalysts and a more thorough nitridation compared to easily stackable sheet structure or large cubic structure that hinders quick and even distribution of heat and ammonia gas during the thermal conversion process. Based on the above results, the urchin like CuMOF-H_2O was chosen as the optimal precursor structure and was further engineered by Fe-doping. On the side note, Cu_3N/GO-H_2O sample was prepared by substituting CNT with graphene oxide to investigate the significance of CNT in the synthesis process. As shown in Figure 15, Cu_3N/CNT-H_2O shows higher activity toward OER over Cu_3N/GO-H_2O. The poor catalytic performance of Cu_3N/GO-H_2O could

be owing to the reduced number of active sites and disturbed gas transport due to the GO sheets over the urchin structure, whilst Cu_3N/CNT-H_2O maintains the fully exposed urchin structure.

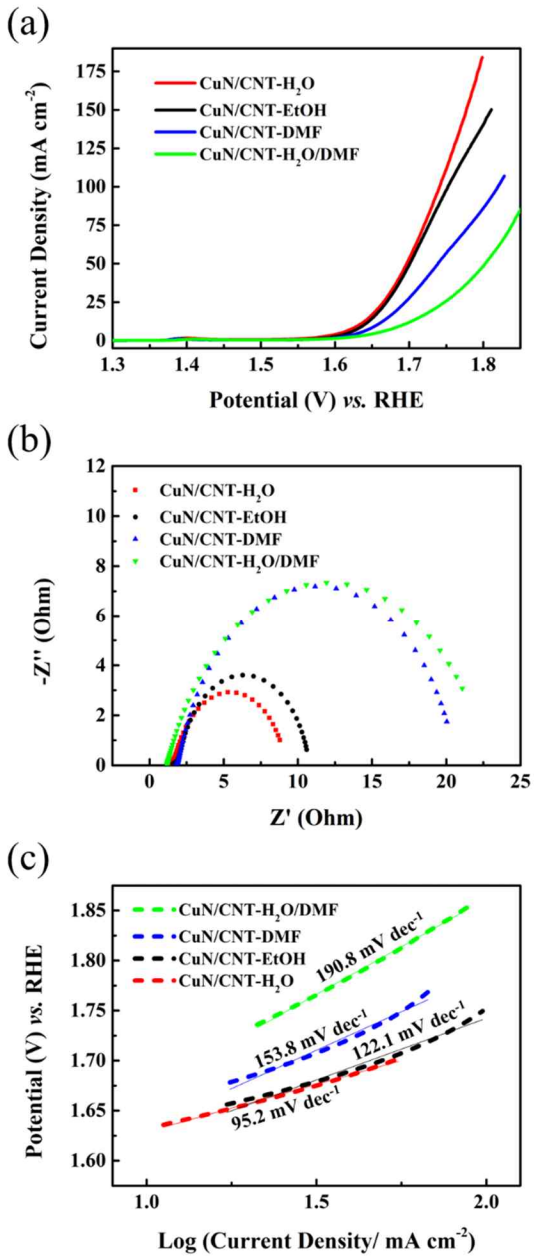

Figure 14 Electrochemical characterizations of CuMOF-H_2O, CuMOF-DMF, and CuMOF-EtOH for OER. (a) iR-corrected polarization curves, (b) EIS characterization, (c) Tafel curves.

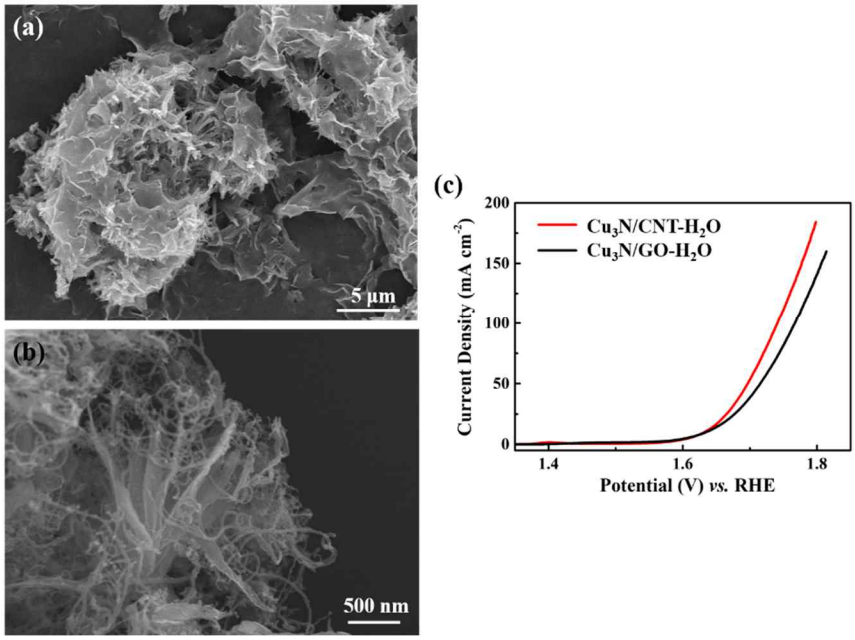

Figure 15 SEM images of $Cu_3N/GO\text{-}H_2O$ (a) and $Cu_3N/CNT\text{-}H_2O$ (b) and their LSV polarization curve towards OER.

Fe-doped CuMOF was prepared by replacing a percentage of copper salt with iron salt during Cu_2O template synthesis. The iron salt percentage was controlled from 0 to 10, 30, 50, 70, and 90%, where each sample is denoted as Cu_2O, CuFeO-10, CuFeO-30, CuFeO-50, CuFeO-70, and CuFeO-90. The as-prepared CuFeO templates were rough surfaced nanoparticles of sizes ranging from 300~500 nm depending on the ratio of Fe salt (Figure 16). Upon Fe ion doping in Cu_2O, the conversion rate of oxide template into MOF greatly accelerated due to the following possible factors: 1. Increase in Cu dissolution rate due to larger surface area to volume ratio coming from the rough surface, and 2. Fe redox potential assisted rapid oxidation of Cu^+ to Cu^{2+}. The XRD spectra of Cu_2O and CuFeO show that while crystal structure remains the same upon Fe incorporation, crystallinity greatly decreases. Loss in crystallinity is another factor that may accelerate metal oxide to MOF conversion by rapid dissociation of the crystal. The resulting CuFeMOFs (CuFeMOF-10, CuFeMOF-30, CuFeMOF-50, CuFeMOF-70, and CuFeMOF-90) still maintained the urchin-like morphology without significant structural changes (Figure 17). Uniform incorporation of Fe in CuFeMOF-50 was confirmed using Energy dispersive X-ray (EDX) spectroscopy. XRD pattern of CuFeMOF-50 remained consistent with that of CuMOF-H_2O.

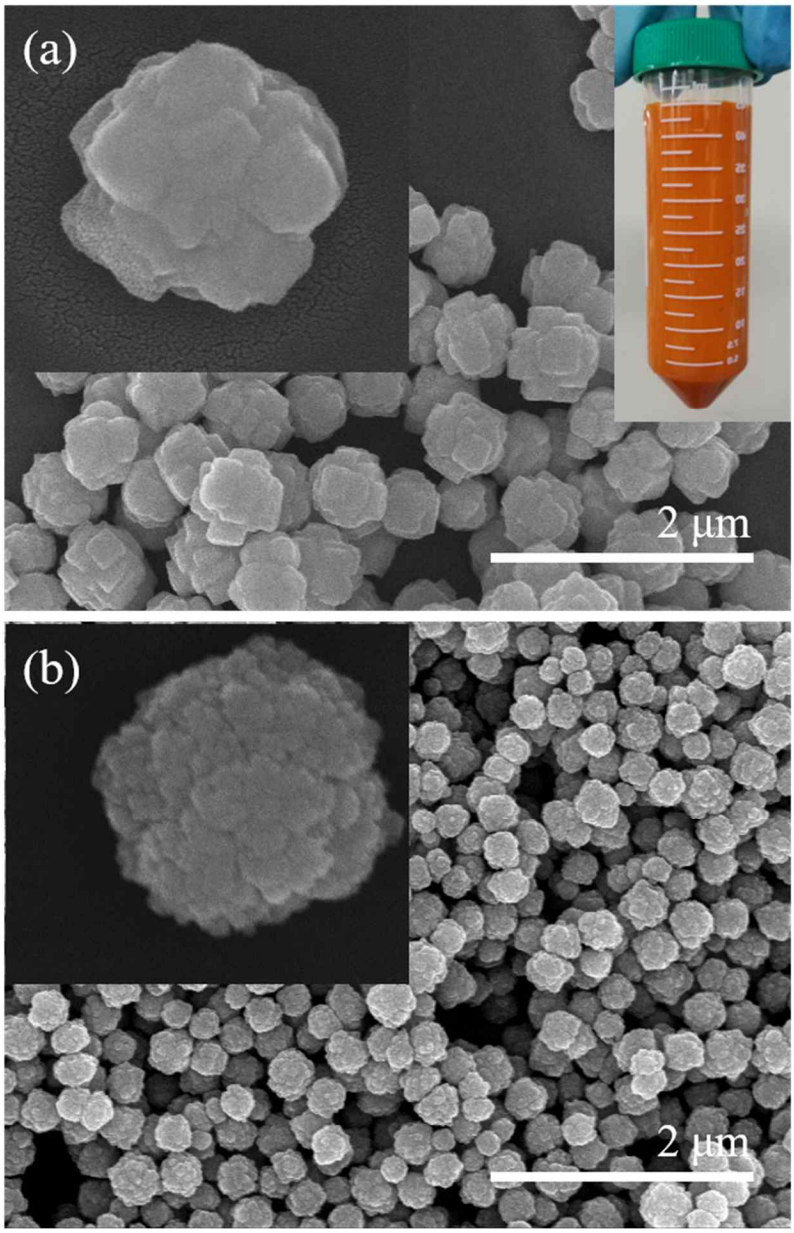

Figure 16 SEM images of (a) Cu_2O and (b) CuFeO. The insets in (a) are enlarged SEM images of Cu_2O and optical image of Cu_2O solution. The inset in (b) is an enlarged SEM image of CuFeO to show the change in surface roughness.

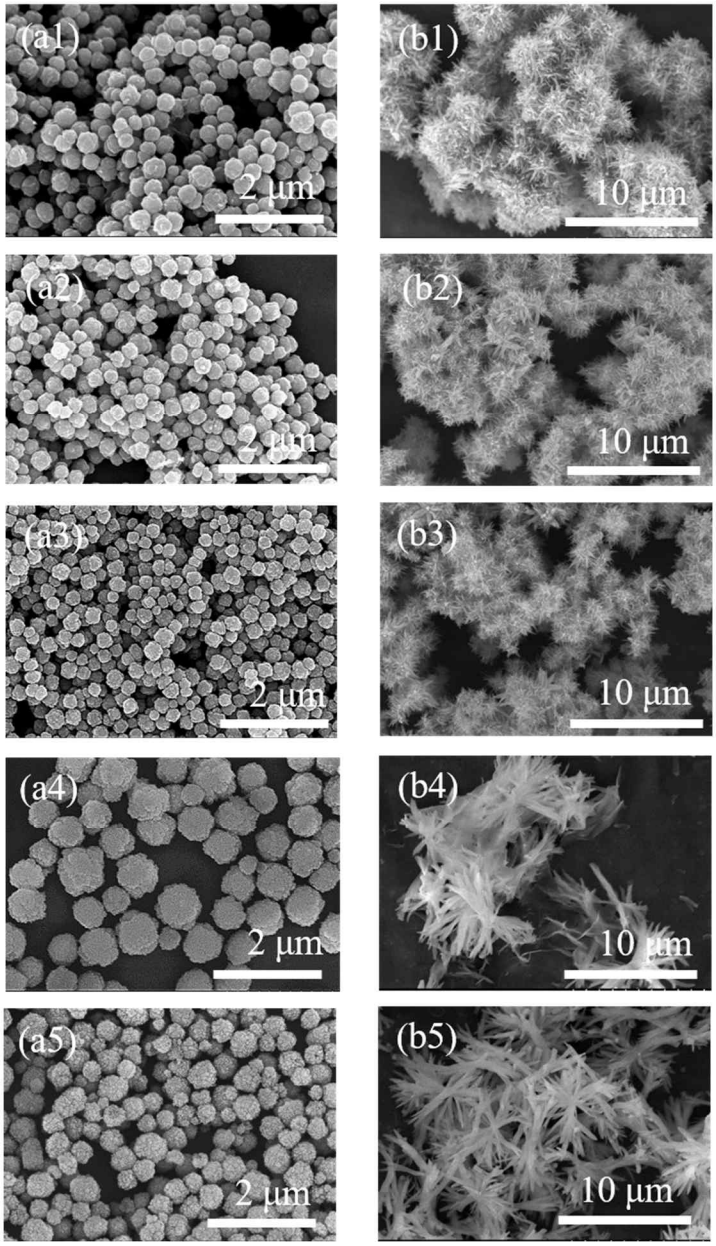

Figure 17 SEM images of (a1) CuFeO-10, (a2) CuFeO-30, (a3) CuFeO-50, (a4) CuFeO-70, (a5) CuFeO-90, (b1) CuFeMOF-10, (b2) CuFeMOF-30, (b3) CuFeMOF-50, (b4) CuFeMOF-70, and (b5) CuFeMOF-90.

The as-prepared CuFeMOFs were again integrated with CNT and NH_4HCO_3 and underwent microwave-assisted nitridation to form CuFeN/CNT catalysts. Integration was achieved by dispersing CuFeMOF in CNT solution with an excessive amount of NH_4HCO_3 followed by lyophilization. NH_4HCO_3 was chosen as the N source for its slightly alkaline property in solution to prevent MOF destruction caused by BDC^{2-} linker protonation. Its low decomposition temperature also provides the reactants with an ammonia rich atmosphere almost simultaneously with microwave irradiation. The as-prepared CuFeMOF/CNT/NH_4HCO_3 sponge was then subjected to microwave irradiation in an Ar filled vial in the presence of carbon cloth (CC).

Electric arc was observed within the first 5 seconds, followed by the occurrence of intense plasma within the reaction media, as shown in Figure 18. In electron rich solid materials such as carbon-based solids, microwave irradiation induces free electrons to oscillate collectively and result in great amount of heat through Joule heating within the grain or arcing at phase boundaries.[168] During collective electron oscillation, sharp edges on the microwave susceptors (CC and CNT) produce a concentrated electric field that causes ionization of the surrounding argon atmosphere, leading to the observed blue plasma.[169] The electric arc and plasma observed during the microwave serve as visual indication

of microwave-assisted thermal reaction taking place. After 30 seconds of microwave irradiation, CuFeN was obtained in a dark brownish black powder form. The role of CC was crucial in this rapid reaction as no reaction was observed in its absence. CC functioned as a microwave susceptor to create immense amounts of heat rapidly. The created heat first catalyzed thermal reduction of oxidized CNT into reduced CNT, then CC and reduced CNT both functioned as microwave susceptors to create and transfer large amount of heat evenly within the reactants. In the absence of CNT, only the parts in direct contact with CC were transformed while the rest remained unreacted. The produced heat decomposed ammonium bicarbonate and urea into ammonia and ensured even nitridation reaction of the precursor MOF. Detailed construction of the reactor is depicted in Figure 19. The duration of microwave exposure was experimentally controlled and settled to 30 seconds to ensure complete conversion of the reactants. The collected catalysts were labeled CuFeN/CNT-10, CuFeN/CNT-30, CuFeN/CNT-50, CuFeN/CNT-70, and CuFeN/CNT-90, where the numbers are denoted to Fe reactant percentage, and were tested for electrocatalytic performance toward OER.

OER evaluation was carried out in a typical three-electrode electrochemical cell using Hg/HgO as reference electrode and graphite

rod as counter electrode in alkaline media. The linear sweep voltammetry (LSV) polarization curves of CuFeN/CNT with different Fe percentages, pristine NF, and commercial RuO_2 are shown in Figure 20. The catalytic performance of CuFeN/CNT noticeably increases as the percentage of Fe increases from 0 to 50, and decreases as Fe further increases. CuFeN/CNT-50 sample shows the highest catalytic performance with a current density as high as 200 mA an overpotential of 414 mV, which is a comparable result to that of precious metal catalyst RuO_2 (205 mA). Moreover, at overpotentials higher than 414 mV, the catalytic performance of CuFeN/CNT-50 exceeds that of RuO_2.

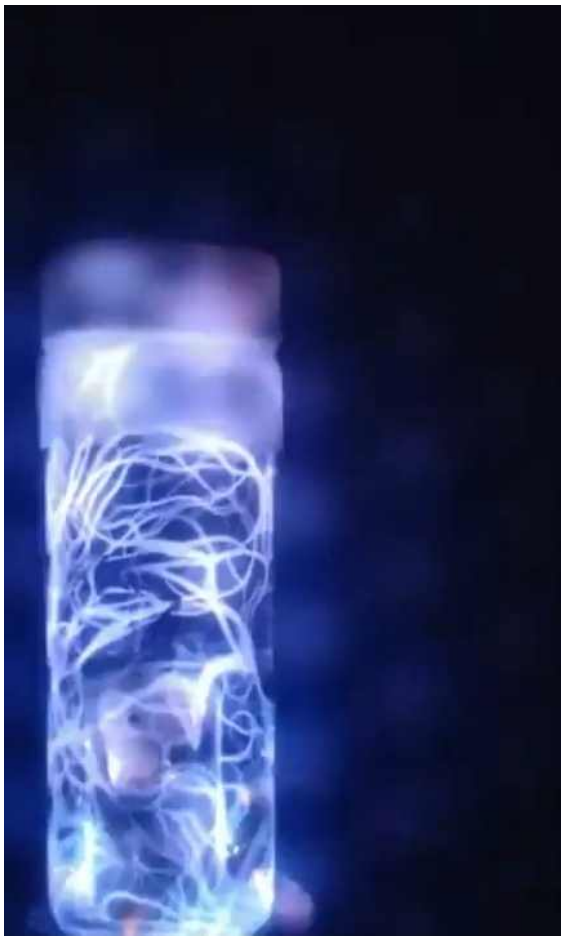

Figure 18 An optical image of the electric arc in the reaction vial upon a few second microwave irradiation.

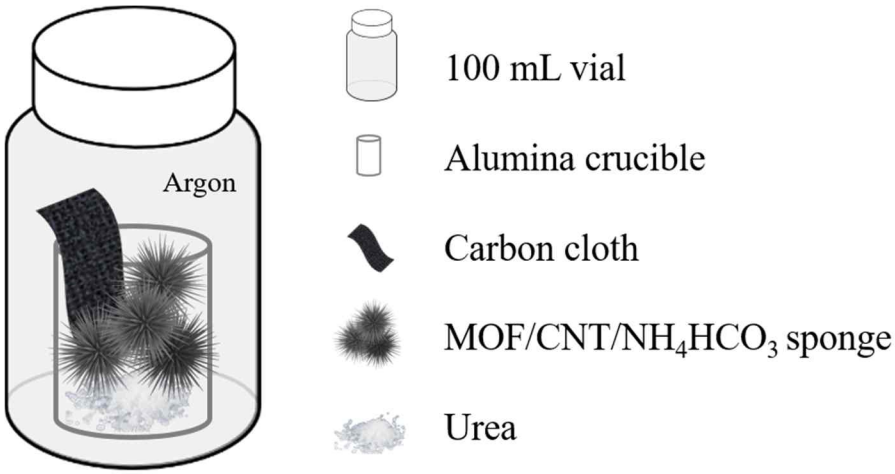

Figure 19 Illustrative image of the reactor and the components for microwave-assisted thermal conversion.

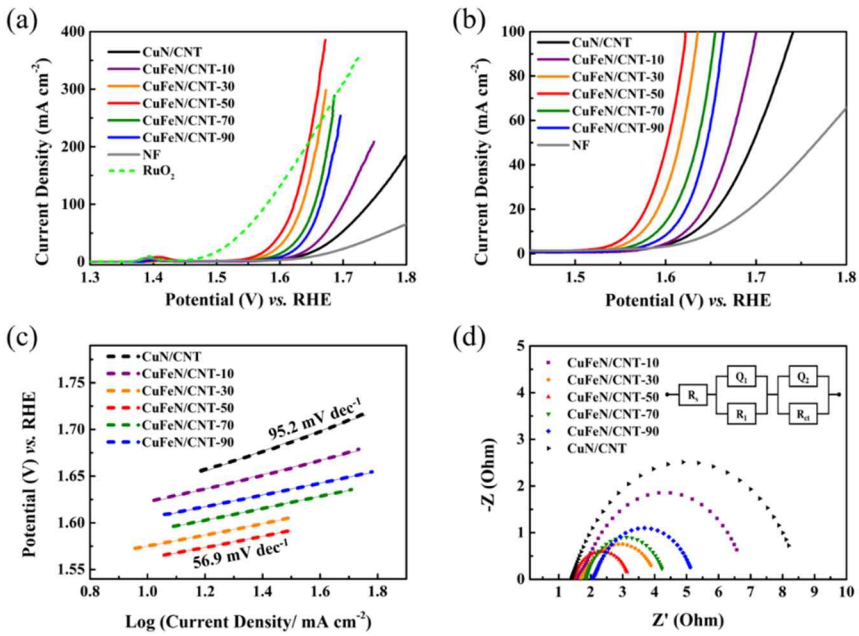

Figure 20 Electrochemical characterizations of CuFeN/CNT for OER. (a) LSV polarization curves in comparison with RuO_2, (b) LSV polarization curves compared at 100mA (c) Tafel curves, (d) EIS characterization.

At a fixed current density of 100 mA, the overpotentials of CuFeN/CNT catalysts in varying Fe percentage are 392 mV (50%), 405 mV (30%), 425 mV (70%), 434 mV (90%), 470 mV (10%), and 510 mV (0%) (Figure 20b). This increasing and decreasing trend of overpotential can be confirmed by Tafel slope study shown in Figure 20c, where CuFeN/CNT-50 has the smallest value of 56.9 mV dec^{-1} compared to those of CuFeN/CNT-30 (57.1 mV dec^{-1}), CuFeN/CNT-70 (60.8 mV dec^{-1}), CuFeN/CNT-90 (61.4 mV dec^{-1}), CuFeN/CNT-10 (71.4 mV dec^{-1}), and CuN/CNT (95.2 mV dec^{-1}). This trend is even clearer in electrochemical impedance spectroscopy (EIS) analysis (Figure 20d). The circuit model employed for EIS fitting is shown in Figure 21. The solution resistance (R_s) and the charge transfer resistance (R_{ct}) can be derived from the semicircles in the Nyquist plot. CuFeN/CNT-50 marks the smallest R_{ct} of 1.74 Ω while those of lower and higher Fe content increase up to 7 Ω. From the generally low Rct value of all the catalysts, good overall electrical conductivity is suggested, possibly owing to well-connected CNT network and highly conductive metal nitride species. These results demonstrate that the OER kinetics and activity is in good agreement with the LSV polarization curves.

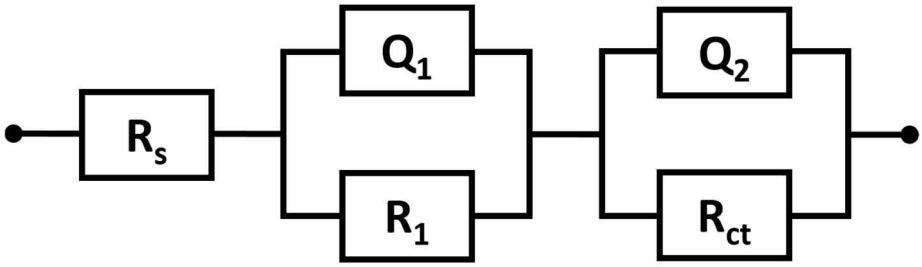

Figure 21 Equivalent circuit model for EIS fitting.

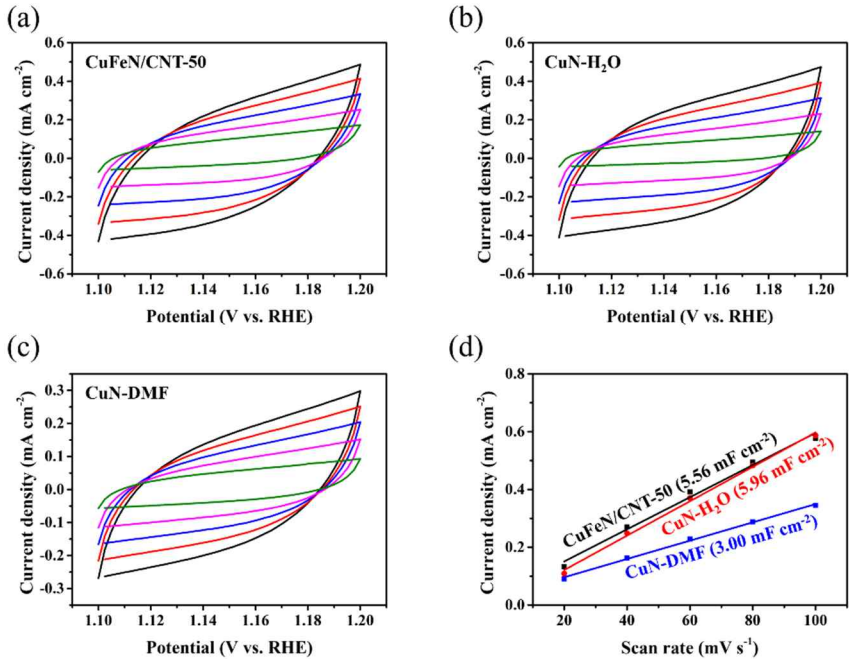

Figure 22 CV curves at scan rates 20, 40, 60, 80 and 100 mV s^{-1} measured in 1M KOH for CuFeN/CNT-50 (a), CuN-H_2O (b), and CuN-DMF (c); and their capacitive current differences at 1.15 V as a function of scan rates (d).

The above results indicate that Fe incorporation has a great influence on the electrocatalytic performance of CuFeN/CNT. In order to identify the origin behind the much-enhanced OER performance upon Fe incorporation, the electrochemically active surface areas (ECSA) of CuFeN/CNT-50 and CuN-H_2O were evaluated by conducting cyclic voltammetry in the region of 1.1 to 1.2 V vs. RHE at various scan rates followed by linear fitting of the capacitive currents to scan rates (Figure 22). The obtained linear slope of CuFeN/CNT-50 is 5.56 mF cm^{-2} while CuN-H_2O shows a similar value of 5.96 mF cm^{-2}, indicating that the ~14-fold increase in current density at 1.67 V vs. RHE is highly owing to the superior intrinsic catalytic activity of CuFeN/CNT-50. On the other hand, the linear slope of the sheet-like CuN-DMF sample is only half the value of the urchin-shaped CuN-H_2O (3 mF cm^{-2}), which is proportionate to the twofold difference in current density at 1.8 V vs. RHE (Figure 22 c, d). This result clarifies that while catalyst morphology is directly related to the ECSA; incorporating iron does not affect the ECSA but strongly enhances the intrinsic catalytic property towards OER.

To investigate the impact of nitridation on the enhanced electrocatalytic performances, CuFeO/CNT and CuFe/CNT catalysts were prepared in the absence of NH_4HCO_3 in air and argon gas filled atmosphere, respectively.

As shown in Figure 23a, LSV polarization curves of the as-prepared CuFeO/CNT and CuFe/CNT catalysts show significantly larger overpotentials compared to CuFeN/CNT catalyst, confirming that nitridation also contributes significantly to the enhanced catalytic property.

Stability being another important criterion in catalyst evaluation, CuFeN/CNT-50 was subjected to accelerated degradation by running 1000 continuous CV scans at a scan rate of 0.1 V s^{-1}. Shown in Figure 23b is the OER polarization curve of CuFeN/CNT-50 showing good stability even after 1000 rapid scans. Long-term stability was evaluated via chronopotentiometry at constant current density of 50mA for 20 hours (Figure 23c). CuFeN/CNT-50 showed an overall stable potential response with only 1.86% deviation from the initial potential, showing remarkable stability for a non-in situ grown catalyst.

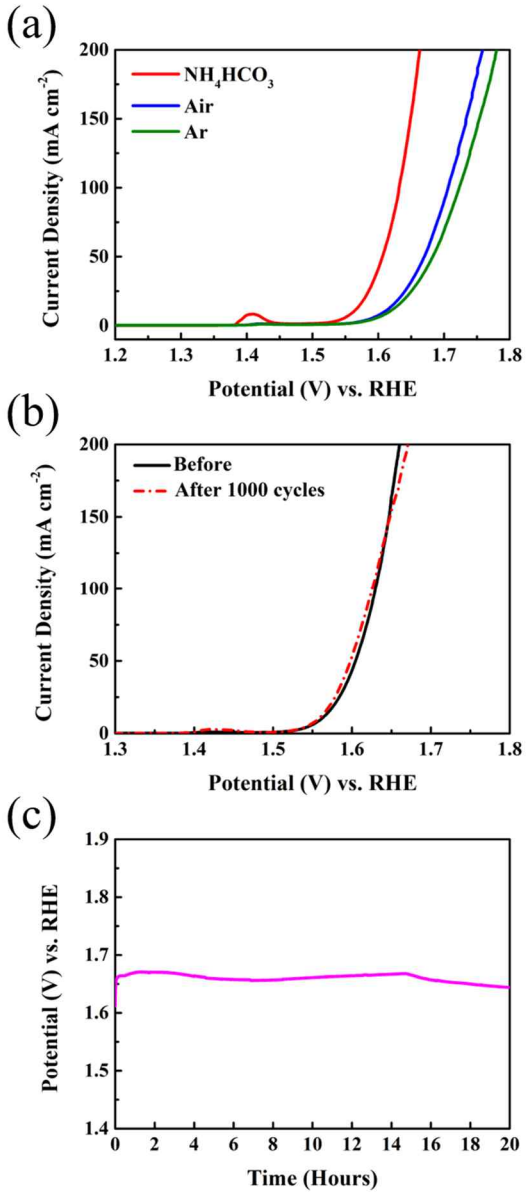

Figure 23 (a) LSV polarization curves of CuFeN, CuFeO, and CuFe prepared in ammonia, air, and argon atmosphere. (b) OER polarization curves of CuFeN/CNT before and after 1000 durability test cycles. (c) Chronopotentiometry at a constant current density over 20 hours.

The morphology and composition of CuFeN/CNT-50 was studied using SEM, TEM, EDX, ICP-AES, XRD, and XPS. As shown in the SEM images (Figure 24a, c), urchin structures covered in intertwined CNT fibers forming a network and small particles were observed together with a few larger clusters of small particles. TEM images confirm the well-preserved urchin structure embedded in tangled CNT bundles, together with ~15 nm catalyst nanocrystals grafted and well exposed on the surface of CNT fibers (Figure 24b, d). The urchin structure composited with tangled CNT network contains numerous pores that should give easy access for the electrolyte and quick escape routes for gas bubbles. Even distribution of all elemental components were confirmed using TEM-EDX analysis (Figure 24e).

As it is clear from the electrochemical studies of catalysts prepared in varying Fe to Cu ratio that the amount of Fe incorporation has a great influence on the electrocatalytic performance of CuFeN/CNT, the precise composition of Fe in CuFeN.CNT-50 was investigated using ICP-AES. The ICP-AES result identified Fe to Cu ratio as 9.1 to 0.9, suggesting that only 20 % of the initial iron reactant successfully substitutes copper during the synthesis process.

The XRD pattern of CuFeN/CNT-50 is displayed in Figure 25. The prominent peaks at around 23, 33, 41, and 47° can be assigned to the

(001), (011), (111), and (002) planes of copper nitride (Cu_3N). A broad peak around 26° can be attributed to the carbon peak of CNT. The shorter peaks at 18, 26, 28, and 29° are assigned to triuret, the product of pyrolysis of urea. It is worthy to note that all the Cu_3N peaks show slight shifting toward lower angles (Figure 25b). Shifting in XRD peak position often occur due to defect-oriented lattice distortions, direction towards lower angle indicating compressive strain within the lattice while shifting towards higher angle indicate tensile strain within the lattice.[170–172] Considering the smaller crystal ionic radii of Fe ($r_{ion}(Fe^{2+})=0.75$ Å, $r_{ion}(Fe^{3+})=0.69$ Å) compared to that of Cu ($r_{ion}(Cu^{1+})=0.91$ Å), the Fe-substituted Cu_3N may be subjected to compressive strain within the lattice, displaying a peak shift towards lower angle.[173] Thus, we can assume from the XRD result that CuFeN exists in the form of Fe doped within the Cu_3N lattice structure. The XRD peaks are relatively broad and weak in intensity, implying that the CuFeN particles are amorphous. The HR-TEM image of a single catalyst particle shows no definite lattice structure, confirming the amorphous property of the catalyst (Figure 26).

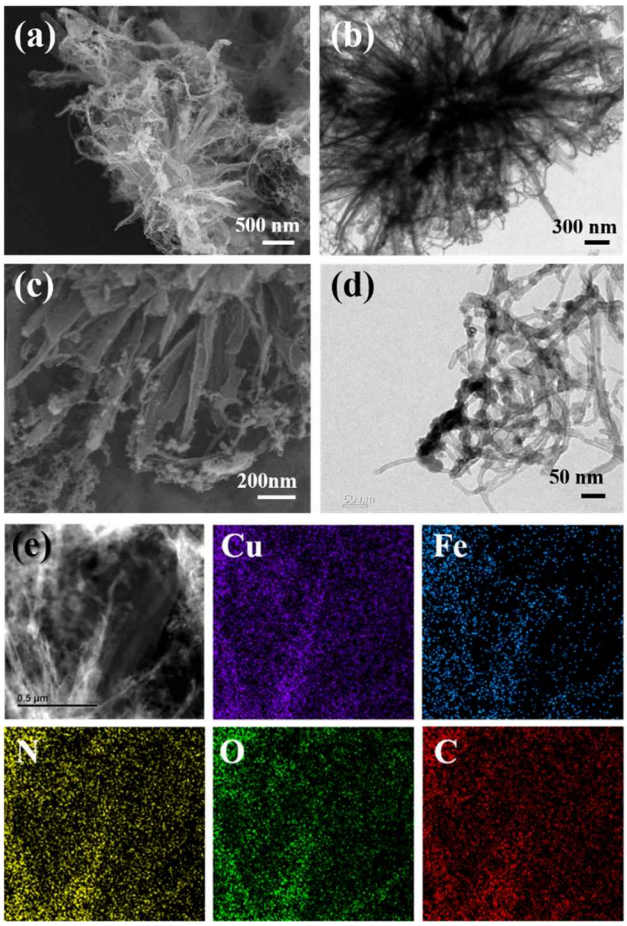

Figure 24 SEM (a, c) and TEM (b, d) images of CuFeN/CNT-50. (e) TEM-EDX elemental mapping images of CuFeN/CNT-50, showing uniform distribution of Cu, Fe, N, O, and C.

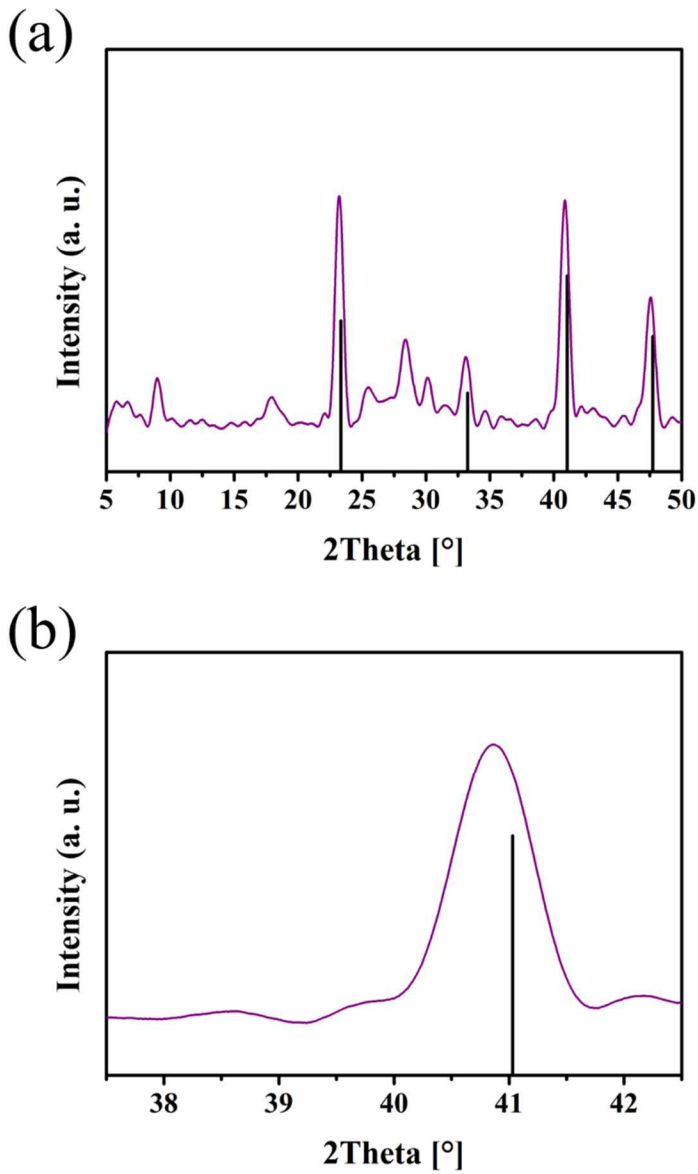

Figure 25 The experimental XRD pattern of the CuFeN/CNT-50 corresponding to the standard copper (I) nitride peaks (ICSD # 98-002-5675) (a), and an enlarged view of the XRD scan around 41°(b).

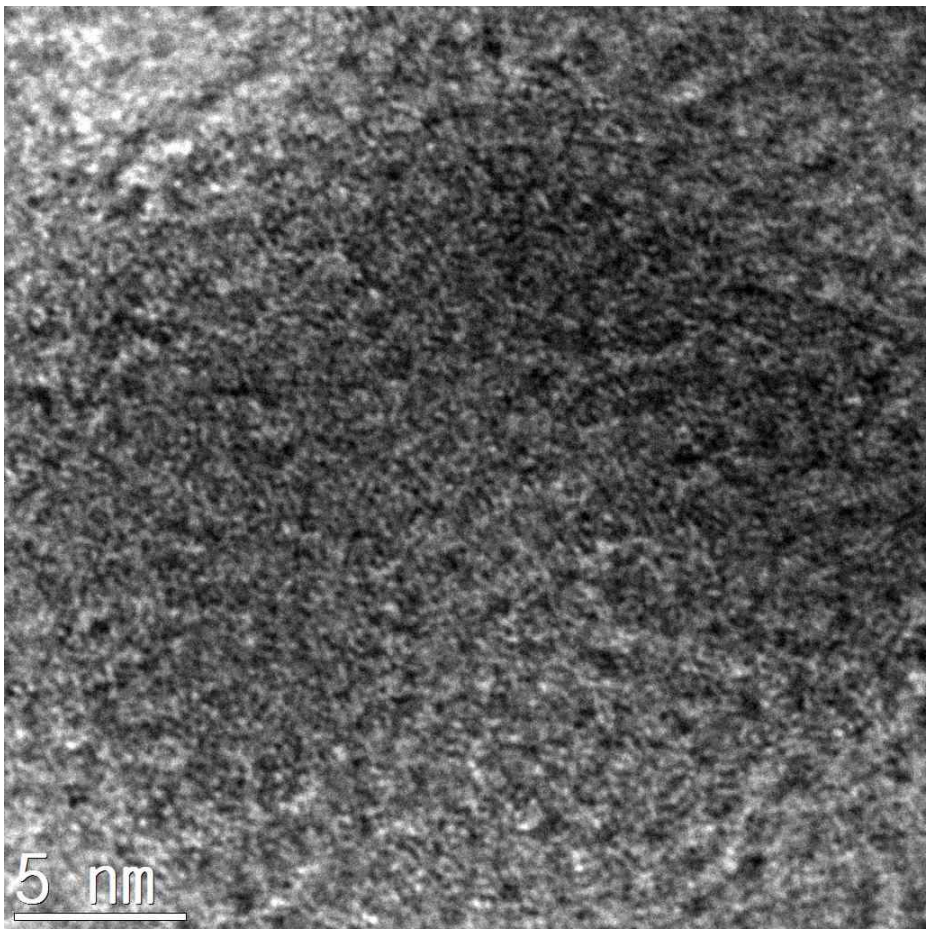

Figure 26 HR-TEM image of a single CuFeN/CNT-50 catalyst particle.

Detailed surface electronic states of all the elements in CuFeN/CNT-50 were investigated by XPS before and after OER. As observed in Figure 27, the XPS survey reveals several peaks at around 934, 720, 531, 399, and 285 eV, corresponding to the Cu 2p, Fe 2p, O 1s, N1s, and C 1s, respectively. The atomic ratio between Cu to Fe measured from XPS peaks for CuFeN/CNT was around 73 to 27. Refer to Table 5 for detailed composition of CuFeN/CNT. Deconvoluted peaks of Cu 2p, Fe 2p, O 1s, and N1s before and after OER are displayed in Figure 28a and b, respectively.

Prior to OER, the dominant Cu 2p3/2 and Cu 2p1/2 peaks centered at 932.8 and 952.6 eV are binding energies for Cu^{+}.[139] Smaller but still clear peaks centered at 934.3 and 954.5 eV together with the two well-known shake-up satellites suggest the presence of divalent copper species (Cu^{2+}) over the surface of the catalyst.[151,174] Fe incorporation is confirmed by four deconvoluted Fe 2p peaks, where the two larger peaks at 712 and 723.6 eV are ascribed to Fe^{2+} and the smaller peaks at 715.2 and 727.5 eV are binding energy of Fe^{3+}.[97] Ns1 peak at around 400 eV is fitted into two components, a significant metal-N bond peak at 399.1 eV and a small peak at 401.6 eV representing physisorbed nitrogen species among the grains.[136] O 1s spectrum consists of four chemically distinct components, where the peak centered at 529.9 eV is

ascribed to the binding energy of M-O, 531 eV to M-OH, 532 eV to C=O, and 533eV to adsorbed H_2O.[124,144] Strong C 1s peak at 285 eV is from the addition of CNT in microwave-assisted nitridation step.[142] Overall, XPS results verify successful doping of Fe and overall nitridation in CuFeN/CNT via microwave assisted nitridation of CuFeMOF.

After OER, surface electronic states of CuFeN/CNT changed due to oxidation of the metallic species. Changes in dominant oxidation state from Cu^{+} to Cu^{2+} and Fe^{2+} to Fe^{3+} are observed in deconvoluted spectra of Cu 2p and Fe 2p post-OER. Large increase in M-OH and M-O peaks as well as decrease in M-N peak intensity is observed. Based on the results of the above analysis, it can be speculated that upon OER activation, the outermost layer of CuFeN nanocrystals are oxidized into metal oxide/hydroxide shell, which most likely serves as the active center for OER.

Judging from the TEM, SEM, XRD and XPS data, we can infer that the CuFeN nanocrystals are well-distributed within and on the surface of the urchin-like porous structure/CNT composite, and the low charge transfer resistance and long-term stability data gathered from EIS and chronopotentiometry support this prediction.

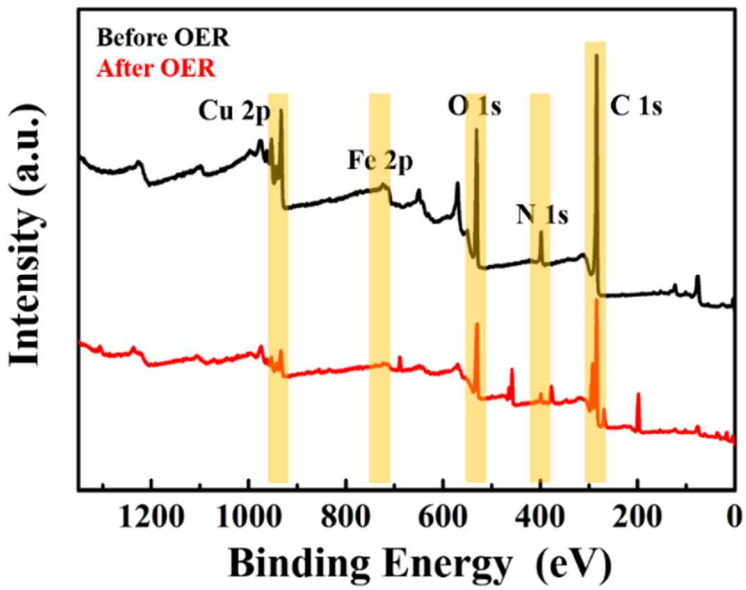

Figure 27 XPS survey of CuFeN/CNT-50 before and after OER.

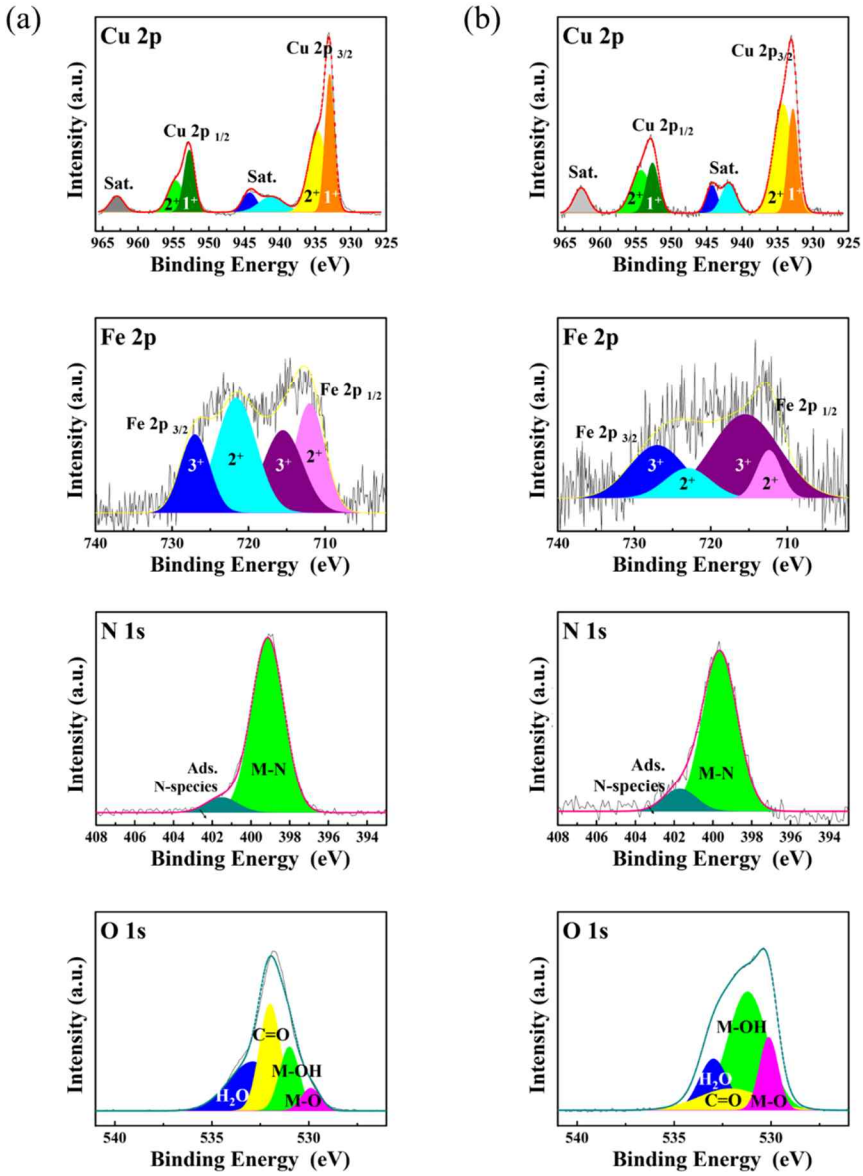

Figure 28 XPS spectra of CuFeN/CNT-50 prior to (a) and post (b) OER.

Table 5 Summary of XPS peaks for CuFeN/CNT

Elements	Atomic Percentage (%)
C1s	68.7
N1s	6.4
O1s	17.95
Fe2p	1.86
Cu2p	5.1

Table 6 Comparison of OER activity for CuFeN/CNT-50 with the previously reported Cu-based electrocatalysts.

Catalyst	**morphology**	**Overpotential (mV)/ current density (mA cm^{-2})**	**electrolyte**	**Tafel slope/ mV dec^{-1}**	**Ref**
CuO	Dendritic nanostructure	290 mV/ 10 mA cm^{-2} ~500 mV/ 100 mA cm^{-2})	1M KOH	64	[175]
HS-CuO/C	Dendritic nanostructure	482 mV/ 100.0 mA cm^{-2}	1M KOH	66.3	[176]
Cu_3P/CF	Cedar-like array	412 mV/ 50 mA cm^{-2}	0.1M KOH	63	[177]
Cu_2Se (ED-2)	Nanostructured granules	320 mV/ 10 mA cm^{-2} 390 mV/ 100 mA cm^{-2}	1M KOH	48.1	[178]
$CuCo_2S_4$ NS	Nanosheet	310 mV/ 10 mA cm^{-2}	1M KOH	86	[179]
Cu_3P NB/Cu	Nanobundle	380 mV/ 10 mA cm^{-2} 520 mV/ 50 mA cm^{-2}	1M KOH	72	[180]

Cu_3P-450	Microsheet	370 mV/ 120 mA cm^{-2}	1M KOH	84	[181]
CuO-EA	Film	475 mV/ 10 mA cm^{-2}	1M KOH	90	[182]
CuO	Nanoflower	400 mV/ 100 mA cm^{-2}	1M KOH		[183]
CuBr/Co@CuO	Hollow nanocorals	400 mV/ 100 mA cm^{-2}	1M KOH	67	[184]
Cu_3N −CuO	Core-shell nanocubes	430 mV/ 100 mA cm^{-2}	1M KOH	118.5	[185]
Cu_3N NA/CF	Nanowire array	298 mV/ 20 mA cm^{-2} ~512 mV/ 350 mA cm^{-2}	1M KOH	87	[174]
$NiCuO_x$	Nanoparticles	~630 mV/ 5 mA cm^{-2}	1M Na2CO3	120	[186]
$CuCo_2O_4$	Nanoflower	288 mV/ 10 mA cm^{-2} ~510 mV/ 100 mA cm^{-2}	1M KOH	64.2	[187]

$CuCo_2O_4$–SSM	Hollow spherical particles	400 mV/ 10 mA cm^{-2}	1M KOH		[188]
$CuRhO_2$		410 mV/ 10 mA cm^{-2}	1M KOH		[189]
$NiCoSe_2$@NiO@$CoNi_2S_4$@CoS_2	Coin-shaped plates	~510 mV/ 100 mA cm^{-2}	1M KOH	159.1	[190]
CuN/CNT-H_2O	Nanoparticles/ CNT network	510 mV/ 100 mA cm^{-2}	1M KOH	95.2	This work
CuFeN/CNT-50	Nanoparticles/ CNT network	390 mV/ 100 mA cm^{-2} 437 mV/ 350 mA cm^{-2}	1M KOH	56.9	This work

Overall, this research covered a strategic optimization of copper-based OER catalysts derived from MOFs. To the best of our knowledge, this is the first report on morphology variation of Cu-based MOF using solvent-dependent coordination kinetics of metal ions and organic linkers. As a result of this study, exquisite urchin-shaped MOFs were obtained in aqueous medium, unlike most previously reported methods for CuMOF synthesis that use toxic DMF as solvent. Iron was successfully incorporated into the urchin-shaped MOFs without significant morphology changes, and its derivate CuFeN/CNT composites exhibited considerable enhancements in OER activity. At a set current density of 80 mA, the overpotential value decreased by 121 mV upon morphology control and further decreased by 108 mV upon optimal Fe doping, indicating the importance of both structural design and synergistic composition in catalyst optimization. The optimal catalyst CuFeN/CNT-50 exhibited a current density as high as 350 mA cm^{-2} at an overpotential of 437 mV, which is a comparable value to the previously reported copper-based electrocatalysts (Table 6). Moreover, the all-microwave-assisted preparation process minimizes use of toxic organic solvent and consumption of large amounts of energy and inert gas. The versatility of this synthesis method enables low-cost and sustainable synthesis of MOFs and the derived materials for catalysis and extended applications.

2.1.4 Conclusion

In summary, we have investigated the kinetically controlled growth of Cu-based MOF in DMF, ethanol, and H_2O and observed three distinctly different morphologies including sheet, core-shell, and urchin-like structure. Subsequently, the Cu-based MOFs were integrated with CNT and nitridated via 30-second microwave irradiation. The urchin-shaped MOF-derived CuN/CNT catalyst showed superior OER activity over those derived from crude-shaped MOFs owing to its superior surface area that enables more thorough nitridation, formation of smaller catalyst particles due to faster nucleation, and free electrolyte movement through the pores. The catalytic property of the urchin-shaped MOF derived CuN/CNT could be further enhanced by Fe doping in the MOF precursor. The resulting CuFeN/CNT composite exhibited greatly enhanced OER activity, affording high current densities exceeding that of RuO_2 at overpotentials higher than 414 mV. The result highlights the importance of both structural design and synergistic composition for high-performance electrocatalysts. The described synthetic approach is facile and environmentally benign and may be extended to other transition metal-based MOFs for various catalytic applications.

Part 2. Transformation of microwave synthesized highly uniform FeMo-MIL-88B nanorod to oxynitride derivate for overall water splitting reaction

2.2.1 Motivation

Due to aggressive fossil fuel combustion over the past two centuries, fuel depletion is predicted within the next century.[191] However, whilst depletion could become a critical issue in a few decades, there is another more pressing issue to fossil fuel: climate change. The carbon dioxide and other greenhouse gases emitted from fossil fuel combustion are the primary contributors to climate change. For this reason, there is an urgent demand for sustainable energy sources such as hydrogen. Hydrogen seems like the perfect alternative as it is harmless to the environment and has a high mass energy density (142 MJ kg^{-1}).[192][193] Nevertheless, ~95 % of industrial hydrogen gas is produced through coal gasification and steam reforming, which not only require enormous amounts of energy, but also leads to excessive carbon emissions.[12] Therefore, low-energy and emission-free hydrogen production method is necessary.

Electrochemical hydrolysis or water electrolysis is an emission-free and sustainable route for high-purity hydrogen production.[194–197]

However, the sluggish kinetics that consume higher energy than theory and the costly and scarce state-of-the-art catalysts composed of noble metals render water electrolysis completely impractical in commercial applications.[198][126] Subsequently, great efforts have been made in designing low-cost transition metal alternatives, including metal oxides[199], carbides[200], nitrides[201], oxides[202], oxynitrides[57], phosphides[203], sulfides[204], selenides[205], and more. Among them, metal nitrides and oxynitrides are particularly noteworthy for their high electrical conductivity, corrosion-resistance, mechanical stability, and enhanced charge transfer rate.[58,206–209]

Previous reports showed that carefully designed iron-based nitrides serve as efficient low-cost OER catalysts in alkaline media. Yu et al. reported a nanoporous iron nitride film deposited on graphene/Ni foam that demonstrates extraordinarily high performance for OER with a current density of nearly 800 mA cm^{-2} at an overpotential of 370 mV and Tafel slope of 44.5 mV dec^{-1}.[210] However, the HER activity of iron nitride was meek compared to the OER activity, and required further engineering with secondary and tertiary metal doping to enhance its performance.[211] Similar result was observed in the work of Chen et al., where the iron-nickel nitride nanoparticles show poor electrocatalytic HER activity compared to its superior OER performance.[212] To

address this problem, Liu et al. doped Mo into iron-nickel nitride nanosheets and achieved a bifunctional catalyst with greatly enhanced HER activity that matches its OER activity.[213] Thus, incorporation of a secondary metal in the electrocatalysts have been observed to give a notable improvement in the electrochemical performance owing to increased number of active sites and reduced charge transfer resistance. Molybdenum has been reported multiple times as a good supplementary transition metal for HER enhancement, as it is known to have excellent hydrogen adsorption property and has been determined by density functional theory to accelerate the sluggish Volmer step in its metal alloys.[70,214]

As such, compositional manipulation for synergistic catalytic promotion is a significant factor in rational design of catalyst. Another major engineering element to consider is structural manipulation for more accessible active sites. One of the widely recognized strategy to structural manipulation is self-templated pyrolysis of metal-organic frameworks (MOFs)[129]. MOF is a class of porous materials composed of inorganic-organic hybrid that offers attractive structural properties including extremely large internal surface area, ultrahigh porosity, and flexible tunability.[152,215–219] The MOF derivates often contain numerous active sites owing to the small and evenly distributed catalysts

confined in the original morphology of the pristine MOF.[220] The organic ligand pyrolized into carbon matrix can serve as conductor and protector, and the internal cavities not only enable additional contact between the active sites and the electrolyte, but also provide facile transport of the evolved gases.[149,221]

With reference to the above-mentioned factors, we herein introduce a simple and energy-efficient synthesis route for MOF-derived FeMoON bifunctional catalyst and conduct in-depth study of its properties. The FeMoON shows a superior HER activity to the single iron oxynitride counterpart in alkaline electrolyte, exhibiting extremely high current density exceeding 750 mA cm^{-1} at an overpotential of 400 mV. In addition, FeMoON shows enhanced OER activity as well, affording current density exceeding 850 mA cm^{-1} at a low overpotential of 364 mV and Tafel slope of 41.5 mV dec^{-1} in 1 M KOH. When combined into an alkaline water electrolyzer, FeMoON outperforms Mo-free FeON and commercial noble metals.

2.2.2 Experimental section

2.2.2.1 Reagents

Iron (III) chloride hexahydrate ($FeCl_3 \cdot 6H_2O$), urea (NH_2CONH_2), N,N-Dimethylformamide (DMF), potassium hydroxide (KOH) were purchased from Samchun. Terephthalic acid (H_2BDC) was purchased from JUNSEI, sodium molybdate dihydrate ($Na_2MoO_4 \cdot 2H_2O$), and Nafion (5 wt%) was purchased from Sigma-Aldrich. Nickel foam (NF) was cleaned by immersing in 1 M hydrochloric acid solution, ethanol, and acetone in order for 15 minutes each. Deionized water was used in all the experiments.

2.2.2.2 Apparatus

Morphology analysis was carried out using field-emission scanning electron microscope (FESEM, Hitachi S-4800) and energy-filtering transmission electron microscopy (EFTEM). Composition was analyzed using the energy-dispersive X-ray spectroscopy (EDS) and high-resolution transmission electron microscopy (HRTEM) (LIBRA 120). The electrochemical impedance spectroscopy (EIS) was measured on ZIVE SP1. X-ray diffraction (XRD) patterns were recorded by a powder X-ray diffractometer (SmartLab, Rigaku, Japan) with a Cu target and a scan rate of $5° \cdot min^{-1}$. X-ray photoelectron spectroscopy (XPS) analysis

was conducted using the Axis-HIS spectrometer at constant energy of 20 eV with Al irradiation of 12 kV and 18 mA. Thermogravimetric analysis (TGA) was performed using a TGA/DSC 1 analyzer (Mettler Toledo) with a heating rate of 4 ℃·min^{-1} in nitrogen gas, and Raman spectroscopy was performed using a DXR2xi (Thermo, USA).

2.2.2.3 Preparation of Fe-MIL-88B

In order to synthesize Fe-MIL-88B, 0.72 g $FeCl_3 \cdot 6H_2O$ and 0.3g H_2BDC was firstly dissolved in 10 ml H_2O and 10 ml DMF and labeled as solution A and B, respectively. The two solutions were then mixed under vigorous stirring for 10 min. The turbid bright-yellow solution was placed in the microwave oven and heated for 60 seconds to form a turbid orange solution. The orange precipitate was washed three times with water and ethanol and dried in a vacuum oven.

2.2.2.4 Preparation of FeMo-MIL-88B

FeMo-MIL-88B was synthesized by adding $Na_2MoO_4 \cdot 2H_2O$ to the above-mentioned method. In brief, 0.3 g $Na_2MoO_4 \cdot 2H_2O$ was dissolved in solution A, and mixed with Solution B under vigorous stirring for 10 min. After microwave irradiation for 60 seconds, the obtained orange precipitate was washed and dried in a vacuum oven.

2.2.2.5 Preparation of FeMoON

The as-prepared FeMo-MIL-88B was placed in a tube furnace together with 3 g urea in the upper stream of the gas flow. Thermal nitridation was conducted at 400 °C for 2 hours. FeON was prepared identically using Fe-MIL-88B as the precursor.

2.2.2.6 Electrochemical measurements

All electrochemical tests were carried out using a three-electrode system on Autolab electrochemical workstation at room temperature. A piece of catalyst-loaded NF (1 cm^2) served as the working electrode, graphite rod as the counter electrode, and Hg/HgO electrode was used as the reference electrode in 1 M KOH electrolyte. A typical preparation of the working electrodes is as follows: 5mg catalyst is first dispersed in 980 μL ethanol with 20 μL Nafion solution and sonicated for 30 minutes to give a homogeneous ink. Then 50 μL of the as-prepared ink was drop-casted onto nickel foam (1.0 cm^2 in area) and dried under an IR lamp. RuO_2 and Pt/C reference materials were identically prepared on NF. Linear sweep voltammetry (LSV) tests were adopted to assess the activity of the electrocatalysts for HER and OER at a scan rate of 5 mV s^{-1}. Electrochemical impedance spectroscopy (EIS) were determined for

frequencies ranging from 0.1 to 100,000 to Hz and with amplitudes of 10 mV at 1.65 V vs. RHE for OER and -0.29 V vs. RHE for HER. The OER and HER long-term stability measurements of the catalysts were conducted at overpotentials of 331 mV and 320 mV, respectively. All tested electric potentials were expressed in reversible hydrogen electrode (RHE) scale according to the Nernst equation: $E_{RHE} = E_{Hg/HgO} + 0.14V + 0.059 \cdot pH$.

2.2.3 Results and discussion

A schematic illustration of the overall preparation process is depicted in Figure 29. Briefly, rod-shaped FeMo-MIL-88B precursor was first prepared via 60-second microwave-assisted solvothermal route and was subjected to soft pyrolysis in presence of urea. Solid urea was placed in the upstream of FeMo-MIL-88B precursor in a horizontal tube furnace to serve as ammonia gas source upon thermal decomposition of urea. The temperature of the furnace was raised to 400 °C at a rate of 4 °C min^{-1} and held for two hours. Finally, the as-prepared rod-shaped hierarchical FeMoON catalyst was collected and subjected to in-depth analysis and electrochemical evaluations.

As illustrated in Figure 30, a typical MIL-88B crystal structure is trimeric iron octahedra regularly linked to oxygen atoms of benzene-dicarboxylate linkers (H_2BDC). Considering that molybdenum is incorporated in the form of oxyanion $[MoO_4]^{2-}$, we presume that $[MoO_4]^{2-}$ function as the anionic linker and coordinate with the positive Fe^{3+} ion in competition with BDC^{2-}, based on the publication of Liu et al. that describes $[MoO_4]^{2-}$ and triazole anionic ligand coordinating with Zn cations to form a porous network.[222] The molecular structure of Fe-MIL-88B and the proposed molecular structure of FeMo-MIL-88B is illustrated in Figure 30a and b. Considering the approximate molecular

size difference of molybdate (3.8 Å) and terephthalate (6.8 Å), the smaller molybdate-incorporated MIL-88B structure is speculated to result in shrunken hexagonal structures compared to that of pristine terephthalate-coordinated MIL-88B structure. The morphological features of Fe-MIL-88B and FeMo-MIL-88B with different Mo content ranging from 0.1 to 0.4 g were observed using SEM (Figure 30c-g). All the samples show well-defined hexagonal rods with pointed ends, which is a characteristic morphology of MIL-88B. Rod width decrease is noticeable as Mo content increases, which can be explained by the shrunken hexagonal structure resulting from the shortened anion linker length, as hypothesized above.

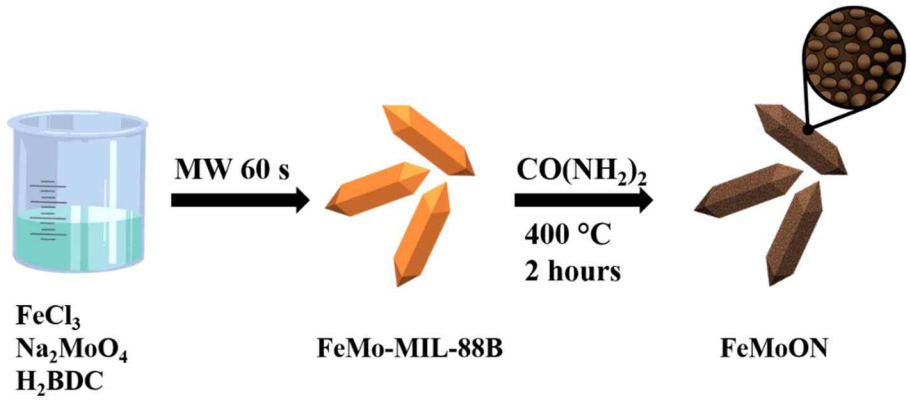

Figure 29 A schematic illustration of the overall formation process of FeMoON.

The X-ray diffraction (XRD) characterization confirms that the crystal structure of Fe-MIL-88B and FeMo-MIL-88B prepared via microwave-assisted solvothermal method have similar diffraction pattern, and are in good agreement with previously reported literatures (Figure 31).[216,223] Thermogravimetric analysis (TGA) was conducted to gain insight into the thermal decomposition demeanor of FeMo-MIL-88B micro rods (Figure 32). TGA was conducted in nitrogen atmosphere at heating rate of 4 °C per minute. Weight loss was observed in two steps, where the first sector between 25 and 400 °C can be ascribed to the removal of adsorbed solvent molecules and reaction between the metal nodes and the oxygen of ligand; and the steep second sector from around 400 to 500 °C can be assigned to complete structural decomposition of FeMo-MIL-88B. Based on the TGA result, 400 °C was chosen as calcination temperature to ensure crystal formation and prevent structural collapse.

Shown in Figure 33 are the XRD patterns of the calcined FeMoON and the standard diffractions of monoclinic β-$FeMoO_4$ (ICSD # 98-004-3013). All the FeMoON peaks coincide with those of β-$FeMoO_4$ without any crystalline impurity, suggesting successful transformation of FeMo-MIL-88B into metal oxynitride. No additional peak related to nitrogen was observed, implying that N doping has not significantly affected the

lattice structure. However, a careful observation of the few distinguishable peaks including the prominent (220) peak reveals a slight shift in peak positions toward higher angle (Figure 33b). In particular, the dominant peak relevant to (220) phase shifted from 26.16 to 26.29, suggesting a reduction in d-spacing from 3.4 Å to 3.38 Å. It is well established that defect-oriented lattice distortions often cause shift in XRD peak position, direction depending on the type of strain within the lattice i.e., compressive strain toward lower angle and tensile strain toward higher angle.[170–172] Considering the higher crystal ionic radii of N ($r_{ion}(N^{3-})=1.32$ Å) compared to that of O ($r_{ion}(O^{2-})=1.26$ Å) [173], the N-substituted β-$FeMoO_4$ lattice may be subjected to tensile strain as a result of crystallite expansion. Thus, we conclude that FeMoON has been successfully doped with nitrogen while retaining the β-$FeMoO_4$ lattice structure. Diffractions of FeON is shown in Figure 34.

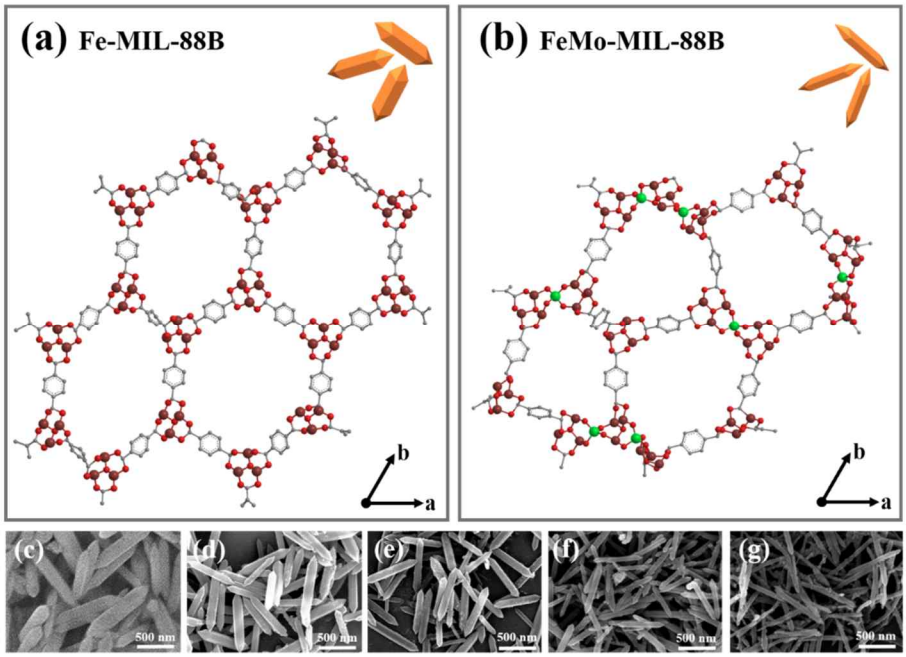

Figure 30 3D illustration of Fe-MIL-88B (a) and FeMo-MIL-88B (b) chemical structure viewed along c-axis: Fe, burgundy; O, red; C, gray; H, hidden for clarity. (c-g) SEM images of Fe-MIL-88B and FeMo-MIL-88B in the order of increasing Mo composition: (c) Fe-MIL-88B, (d) FeMo-MIL-88B(0.1), (e) FeMo-MIL-88B (0.2), (f) FeMo-MIL-88B (0.3), and (g) FeMo-MIL-88B (0.4).

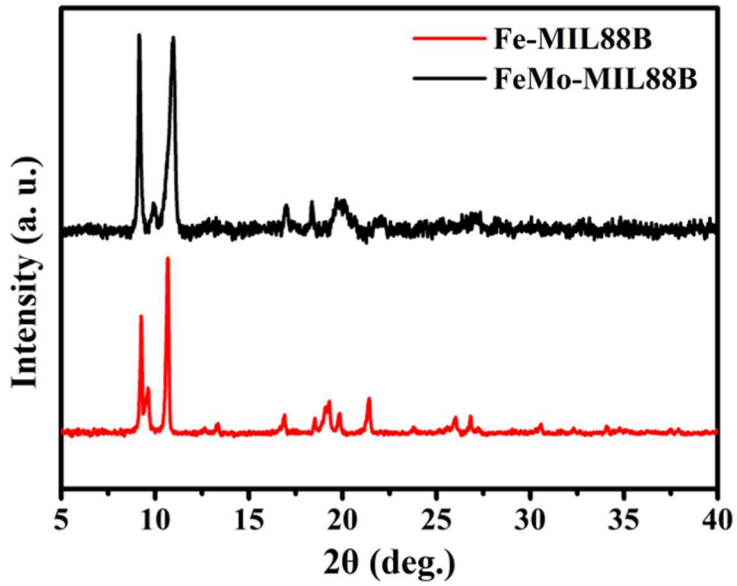

Figure 31 XRD patterns of Fe-MIL-88B and FeMo-MIL-88B.

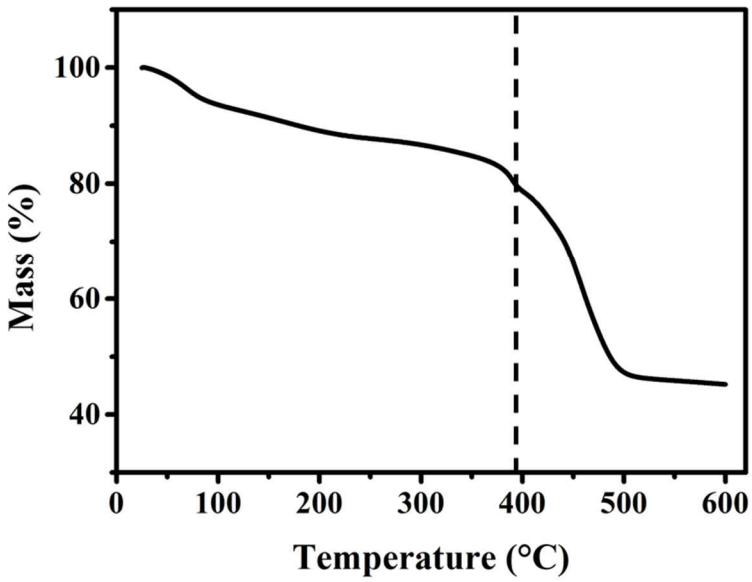

Figure 32 TGA curve of FeMo-MIL-88B.

SEM and TEM observations in Figure 35a-c verify that FeMoON retains the rod-shape of its precursor MIL-88B. The rough-surfaced porous rods were lined with 5-10 nm nanoparticles well isolated from each other. Figure 35f shows the high-resolution TEM (HRTEM) image of a single nanoparticle. The marked lattice fringes of the dominant phase with *d*-spacing of 3.38 Å matches with the aforementioned d-spacing value calculated from the shifted (220) peak in XRD. D-spacing was calculated using Bragg's law: $\lambda=2d\sin\Theta$. Energy Dispersive X-ray Spectroscopy (EDS) elemental mapping and TEM line scan have been conducted to study the distribution of elements within the material (Fig 35d, e). Both EDS mapping and line scan indicates porosity and uniform distribution of Fe, Mo, N, O, and C over the rod-shaped structure. This leads us to conclude that the final structure of FeMoON catalyst is nanoparticles encapsulated in carbon shell bound into porous rod structures. The porous structure composed of tiny individual nanoparticles encapsulated in carbon shell endows the material with large catalytic surface area and good conductivity as well as efficient pathway for electrolyte and gas.

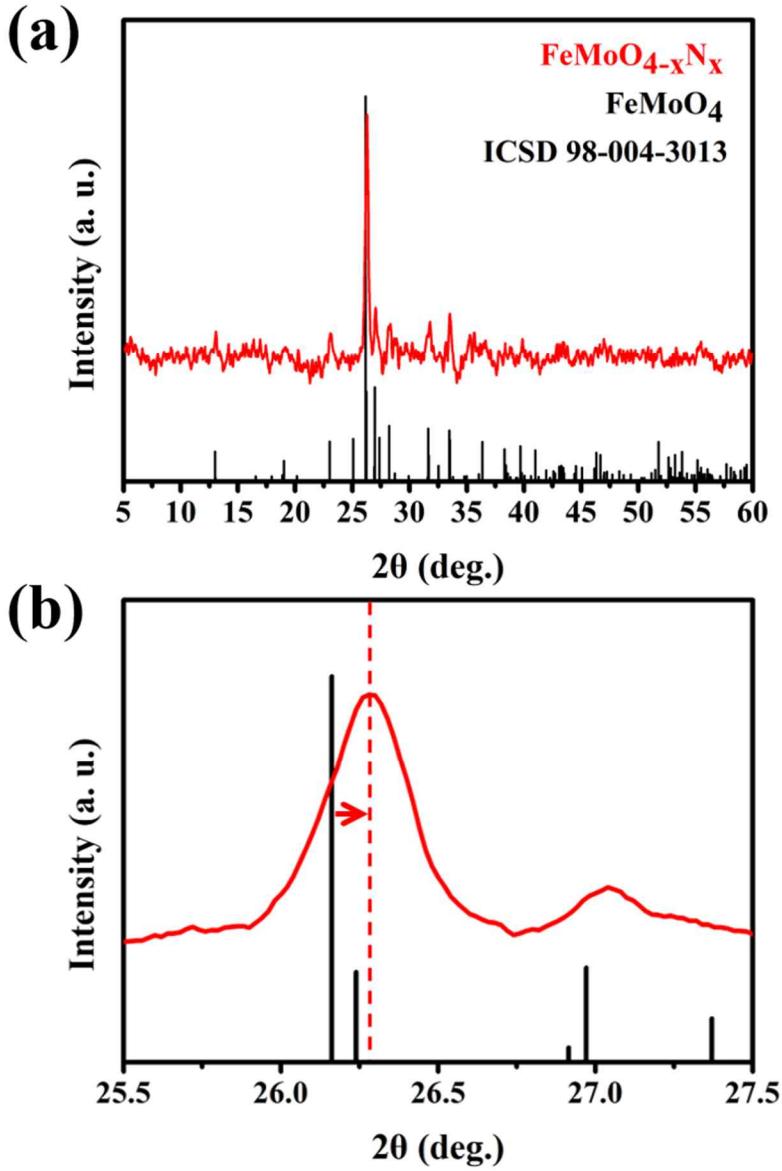

Figure 33 (a) XRD pattern of FeMoON. Standard data: ICSD No. 98-004-3013. (b) Enlarged XRD peak to show shifting of (220) peak.

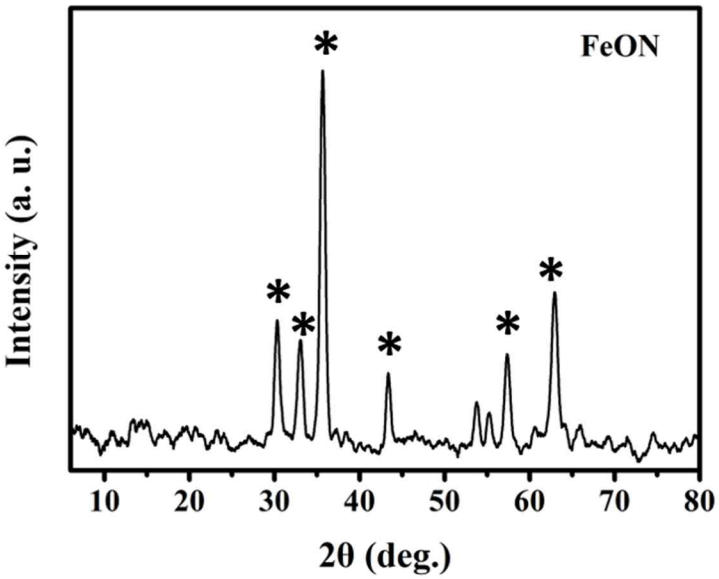

Figure 34 Diffractions of FeON. *: standard Fe_2O_3 peaks identified from ICSD # 98-024-7036 (magnetite) and # 98-016-1291 (hematite).

The surface compositions and the chemical states of FeMoON was investigated by XPS. The survey XPS spectrum displayed in Figure 36 once again confirms that the main elements in FeMoON are Fe, Mo, N, O, and C, coinciding with the EDS analysis. The atomic surface composition acquired from XPS measurements was Fe 8.5%, Mo 3.4%, O 37.2%, N 14.3%, and C 36.6% (Table 7) The atomic ratio of Fe to Mo is similar to the reactant ratio, indicating that most of the Mo reactant took part in the construction of MIL-88B. The Fe to Mo ratio was further confirmed with ICP-AES as 2.5:1, coinciding precisely with the XPS result (Table 8). The nitrogen content was quite high for a product of low-temperature soft-urea calcination, possibly owing to the intrinsic porosity of the MIL-88B that enables thorough nitridation within the structures. Deconvoluted peaks of Fe 2p, Mo 3d, N 1s, O1s, and C 1s are displayed in Figure 37. Fe exists in two oxidation states, where the smaller peaks at 710.5 and 723.9 eV are ascribed to Fe^{2+} oxidation state; and the two larger peaks at 712 and 725.6 eV to Fe^{3+}.[212,224] Mo 3d peaks are deconvoluted into two major components, attributed to dominant Mo^{6+} oxidation state (232.3 and 235.5 eV) and the weaker Mo^{5+} oxidation state (231.5 and 234.4 eV).[225,226] The N 1s XPS spectrum shows a main component at 398.4 eV attributed to metal-N bond and minor broad peaks at 395.3 and 401.1 assigned to N–H groups

and Mo 3p3/2, respectively.[225,226] The four peaks of O 1s spectrum at 530.2, 531.4, 531.9, and 533.2 eV are each attributed to the lattice metal–O bond, hydroxylated surface OH groups, chemisorbed oxygen, and carbonyl groups, respectively. As for the C 1s spectrum, C-C/C=C and C-OH peaks were observed at 284.4 eV and 286.3 eV, respectively.

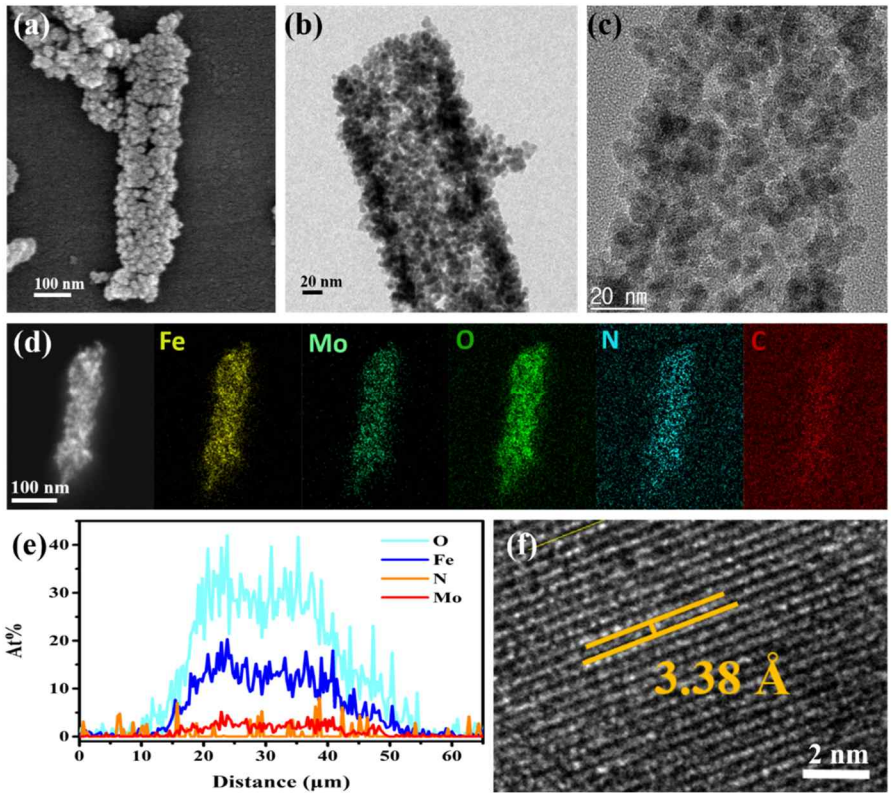

Figure 35 SEM (a) and TEM (b, c) images, EDS elemental mapping (d), TEM line scan in expressed in atomic percentage (e), and HR-TEM image (f) of FeMoON.

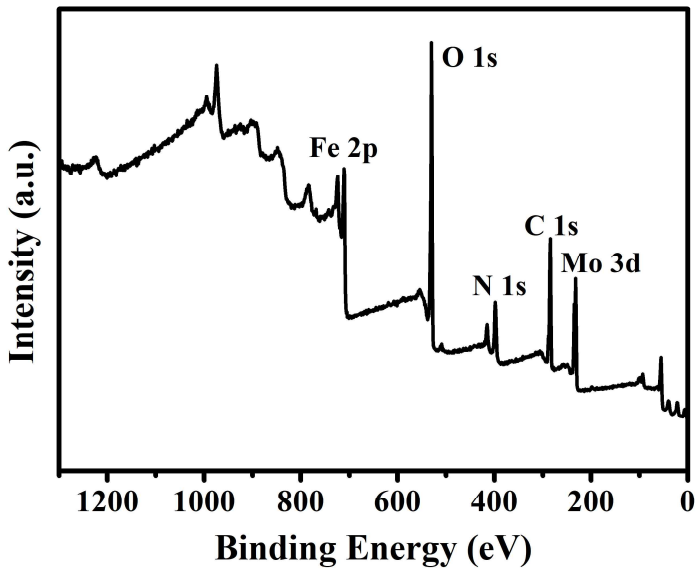

Figure 36 XPS elemental survey of FeMoON.

Table 7 Summary of FeMoON composition measured from XPS.

Elements	Atomic Percentage (%)
Mo3d	3.4
Fe2p	8.5
N1s	14.3
O1s	37.2
C1s	36.6

Table 8 ICP-AES concentration of elements in samples (ppm=mg/kg)

Sample ID	**Fe**	**Mo**
FeMoON	335946.17	226620.99

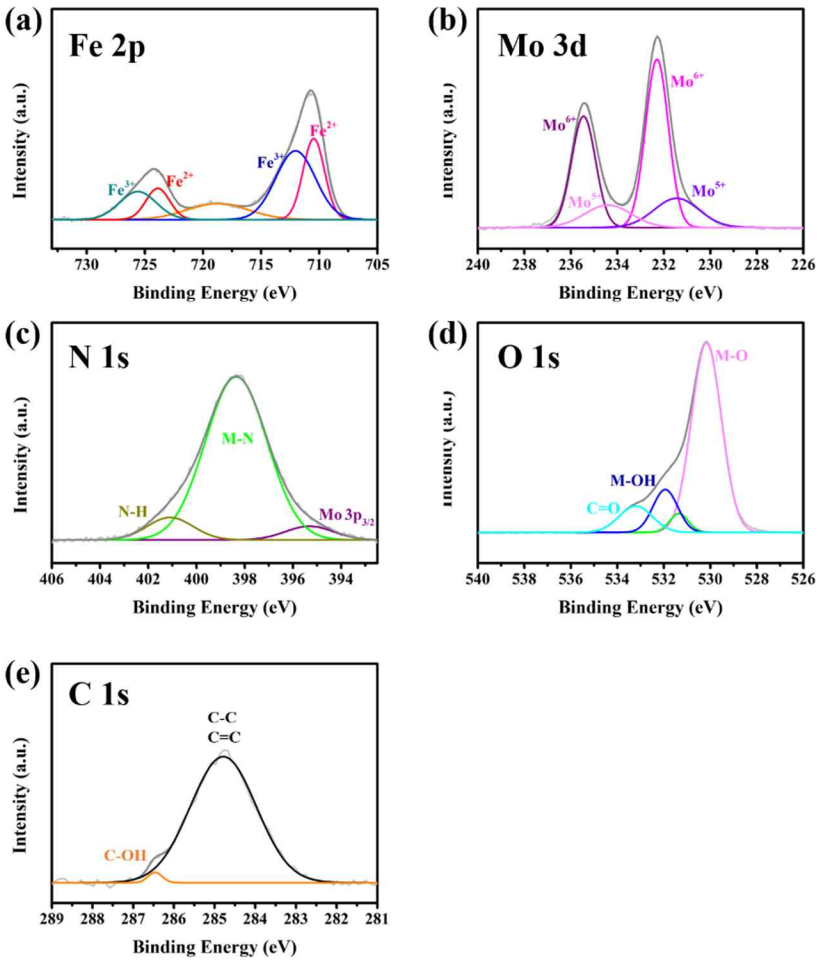

Figure 37 XPS high resolution scan of (a) Fe 2p, (b) Mo 3d, (c) N 1s, (d) O 1s, and (e) C 1s.

The electrocatalytic performances of FeMoON and various comparisons were evaluated in 1.0 M KOH using a typical three-electrode electrochemical cell for both HER and OER. The linear sweep voltammetry polarization (LSV) FeMoON were first conducted to find the optimal amount of Mo. FeMoON with varying Mo content was first evaluated by linear sweep voltammetry (LSV) polarization curves to find the optimal composition (Figure 38). Within a range of 0 to 0.4 g, 0.3 g Mo showed the best performance for both HER and OER and therefore was chosen as the standard amount for FeMoON. The optimized FeMoON was then compared for its electrocatalytic performances with FeON, commercial noble metal catalysts (HER: Pt/C, OER: RuO_2), and bare nickel foam to examine the influence of Molybdenum incorporation. The iR-corrected linear sweep voltammogram (LSV) curves, Tafel slope, and EIS Nyquist plot of all samples for HER and OER are presented in Figure 39 and 40, respectively. The HER activity of both FeON, and FeMoON is significantly higher than that of Ni foam and weaker than that of commercial Pt/C. Nevertheless, it is evident that Mo-incorporation strongly enhances the catalytic activity. At a set overpotential of 400 mV, FeMoON affords a high current density of -750 mA while FeON affords a mere -76 mA. Tafel plots were obtained using a steady-state polarization technique to analyze the catalytic kinetics of

the materials in HER and OER (Figure 41).[227] Tafel slopes represent the potential difference required for 10-fold increase or decrease of the current density. The Tafel slope of FeMoON has a lower value of 73.4 mV dec^{-1} than that of FeON (113.1 mV dec^{-1}), indicating that FeMoON is more favorable for HER kinetics.

In alkaline media, there are two generally accepted HER mechanism: Volmer-Tafel and Volmer-Heyrovsky.

$H_2O + e^- \rightarrow H_{ads} + OH^-$ (Volmer)

$2H_{ads} \rightarrow H_2$ (Tafel)

$H_{ads} + H_2O + e^- \rightarrow H_2 + OH^-$ (Heyrovsky)

General explanation of Volmer pathway is that water molecules adsorb and electrochemically dissociate on the surface of the catalyst, turning into adsorbed hydrogen intermediates (H_{ads}) and OH^- species. When the adjacent H_{ads} are more likely to chemically combine and produce hydrogen gas, the HER mechanism mainly follows Volmer-Tafel mechanism and the Tafel slope would theoretically be less than 40 mV dec^{-1}.[20,228,229] On the other hand, when the H_{ads} and a nearby water molecule accept an electron from the electrocatalysts to form hydrogen gas and OH^-, the mechanism is Volmer-Heyrovsky with Tafel slope less than 116 mV dec^{-1}.[230] Considering the Tafel slope of FeMoON being

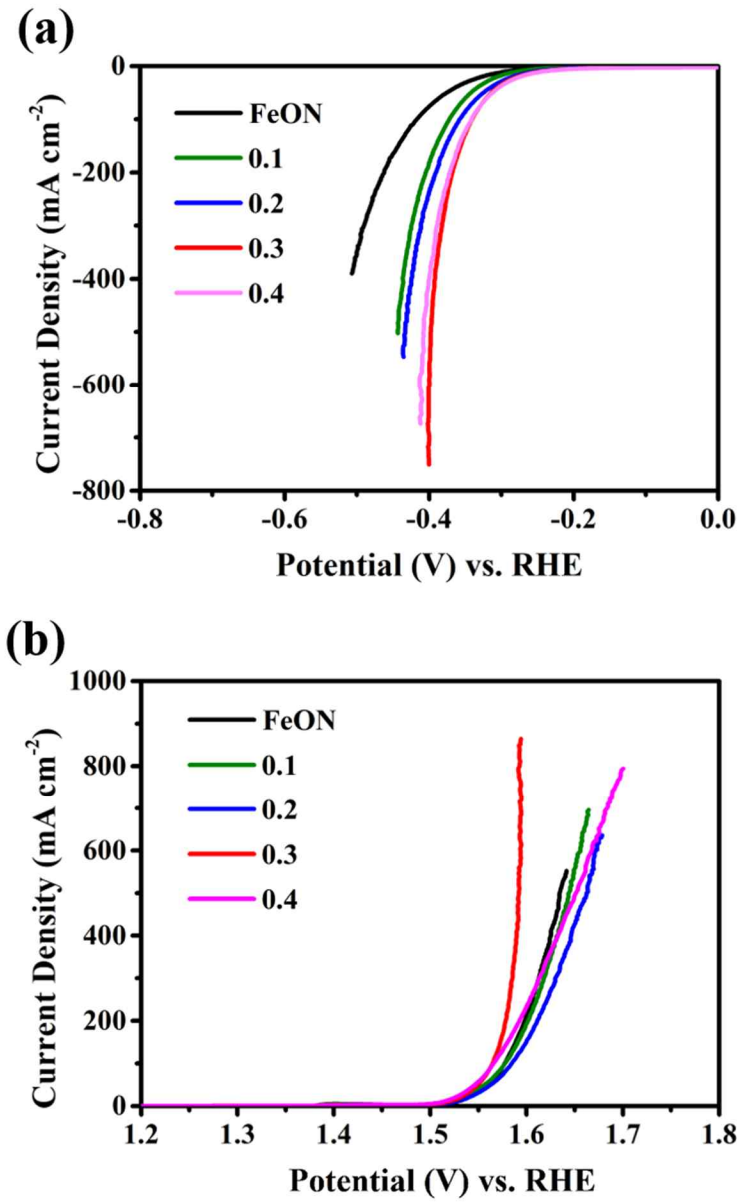

Figure 38 LSV polarization curves of FeON and FeMoON prepared with different Mo contents (0.1, 0.2, 0.3, 0.4 g).

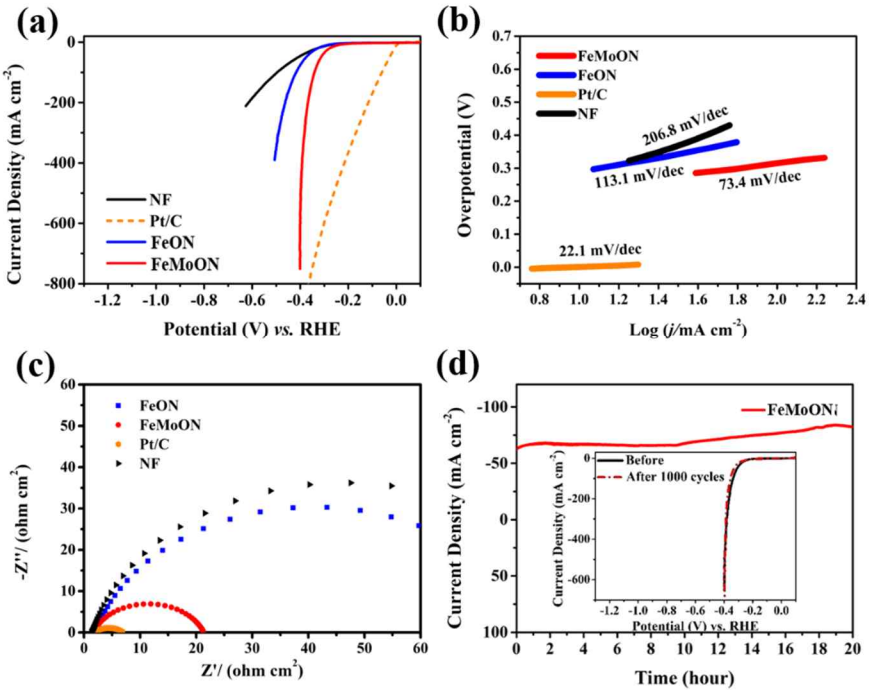

Figure 39 Electrochemical evaluations of FeMoON for HER conducted in 1.0 M KOH. (a) Polarization curves, (b) Tafel plots, and (c) EIS Nyquist plots in comparison with FeON, Pt/C, and NF. (d) Long-term stability test under an applied voltage of -0.29 V. (inset) Polarization curves of the FeMoON before and after 1000 CV cycles.

102.1 mV dec^{-1} from the experimental data, it can be inferred that the main hydrogen production mechanism is Volmer-Heyrovsky.

Electrochemical impedance spectroscopy (EIS) was conducted to study the electron-transfer kinetics at the bias voltage of -300 mV. The semicircles of the Nyquist plots show that the charge transfer resistance (R_{ct}) of FeMoON is much smaller than that of FeON, indicating a more efficient charge transfer process (Figure 39c). Durability test was carried out by the LSV measurement prior to and post subjecting the catalyst to 1000 continuous CV scans at a scan rate of 100 mV s^{-1}. As shown in the inset of Figure 39d, no significant degradation was observed relative to the initial curve. The stability of the FeMoON catalyst was evaluated by long-term chronoamperometry under an overpotential of 330 mV. The current density–time curve demonstrated a stable and flat demeanor for the first 10 hours followed by a gradual increase in current density for the next 10 hours. The result implies that FeMoON catalyst remains stable for up to 10 hours and may undergo further activation from then on.

Besides HER activity, electrochemical activity of FeMoON towards OER was also determined in a standard three-electrode system identical with the HER tests above. RuO_2 was employed as the commercial noble metal electrocatalyst measured for comparison. Figure40a shows the iR-

corrected LSV polarization curves of FeMoON, FeON, Ni foam, and RuO_2. Compared to the poor OER activity of Ni foam (overpotential of 550 mV at 100 mA cm^{-2}), both FeON and FeMoON show much enhanced activity (overpotential of 340 mV and 330 mV, respectively, at 100 mA cm^{-2}) comparable to that of RuO_2 (overpotential of 338 mV at 100 mA cm^{-2}). Moreover, it is noteworthy that the polarization curves of both FeMoON and FeON exhibit a steep rise across the RuO_2 curve, requiring significantly lower overpotentials for higher current densities (FeMoON (358 mV) < FeON (389 mV) < RuO_2 (523 mV) for current density of 375 mA). It is therefore evident that both FeMoON and FeON has better OER activity than the commercial RuO_2 catalyst and that Mo doping gives positive effect on OER activity, though not as significantly as in HER. Figure 40b shows Tafel slopes plotted from the corresponding polarization curves. Both FeMoON (41.5 mV dec^{-1}) and FeON (68.1 mV dec^{-1}) show much smaller slope compared to RuO_2 (94.7 mV dec^{-1}) and Ni foam (111.5 mV dec^{-1}), confirming the superior kinetics of FeMoON over comparisons.

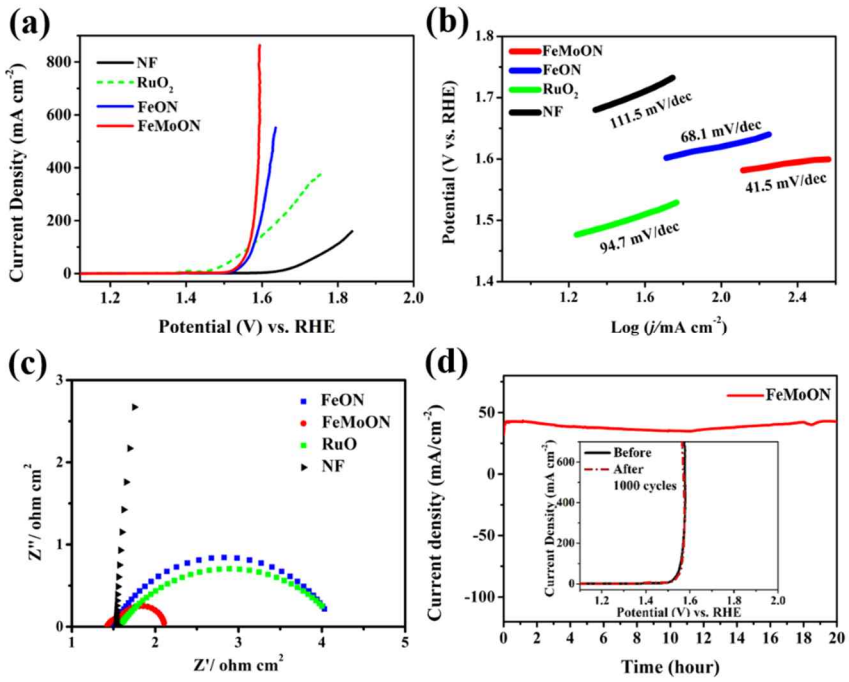

Figure 40 Electrochemical evaluations of FeMoON for OER conducted in 1.0 M KOH. (a) Polarization curves, (b) Tafel plots, and (c) EIS Nyquist plots in comparison with FeON, RuO_2, and NF. (d) Long-term stability test under an applied voltage of 1.65 V. (inset) Polarization curves of the FeMoON before and after 1000 CV cycles.

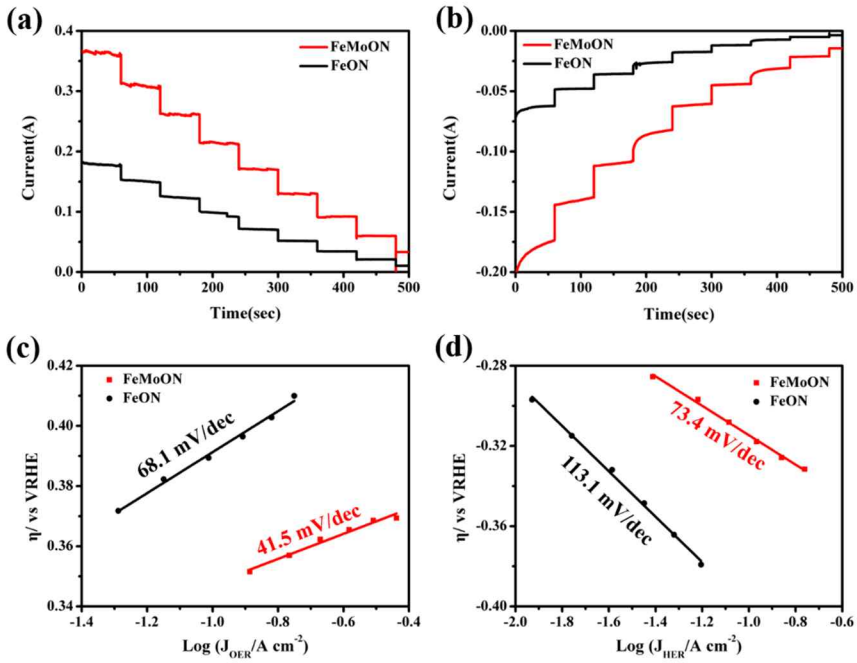

Figure 41 Steady-state polarization for FeMoON and FeON conducted at 20 mV potential steps for OER (a) and HER (b). Reaction order plot of FeMoON and FeON for OER (c) and HER (d).

The rate-determining step of OER can also be determined from Tafel plots.[230,231] When the Tafel slope is ~ 120 mV dec^{-1}, the formation of OH_{ads} intermediate and O_{ads} on the electrode are rate-determining steps. When the Tafel slope is ~40 mV dec^{-1}, the formation of OOH_{ads} on the electrode by the reaction between O_{ads} and hydroxide is the rate-determining step. Finally, when the Tafel slop is as low as 15 mV dec^{-1}, reaction between OOH_{ads} and hydroxide to produce oxygen is regarded as the rate-determining step. From the Tafel slope of 41.5 mV dec^{-1} for FeMoON, it can be inferred that the formation of OOH_{ads} resulting from the reaction between O_{ads} and hydroxide is the main rate-determining step.

$$OH^- \rightarrow OH_{ads} + e^- \quad (4)$$

$$OH_{ads} + OH^- \rightarrow O_{ads} + H_2O + e^- \quad (5)$$

$$O_{ads} + OH^- \rightarrow OOH_{ads} + e^- \quad (6)$$

$$OOH_{ads} + OH^- \rightarrow O_2 + H_2O + e^- \quad (7)$$

The materials were further studied for the electron-transfer kinetics using EIS at 1.65 V. The Nyquist plot of FeMoON in Figure 40c shows a significantly lower charge transfer resistance than FeON as well as RuO_2, indicating a much enhanced electron transfer process owing to Mo

incorporation. Finally, FeMoON was tested for stability and durability. The time-dependent current density profile of FeMoON showed an overall stable current density response at a constant overpotential of 320 mV for over 20 hours (Figure 40d). Excellent durability was observed as well, as the polarization curve of FeMoON before and after 1000 accelerated CV scans showed a negligible difference.

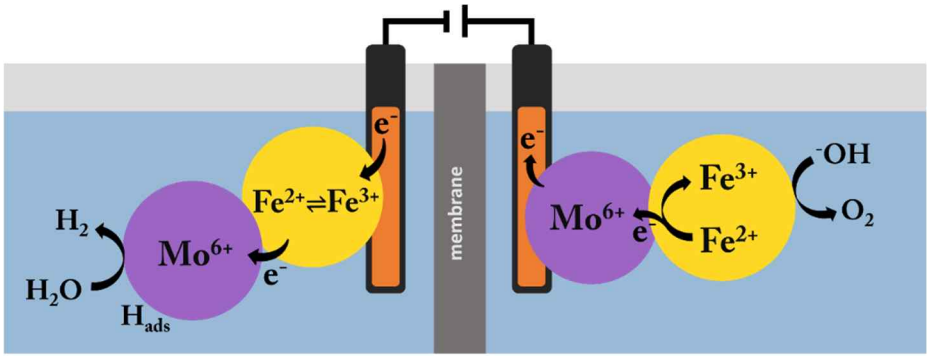

Figure 42 A schematic representation of the proposed mechanism.

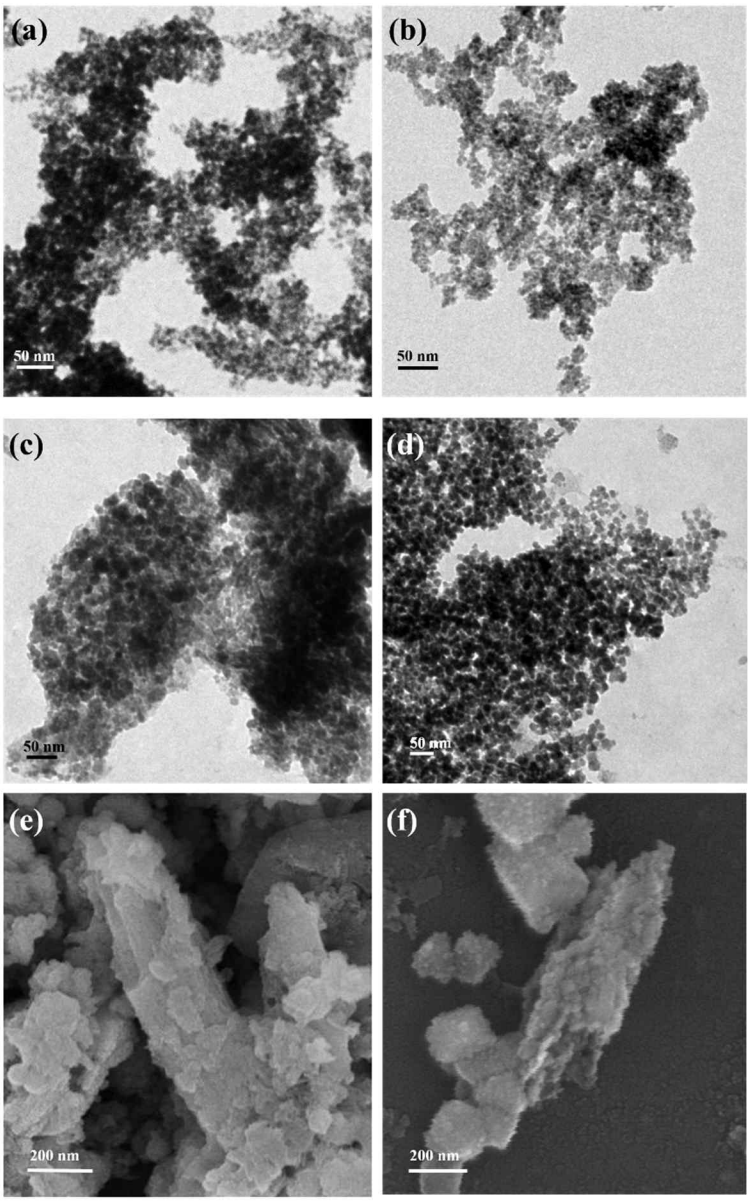

Figure 43 TEM images of FeMoON after a 1000 HER (a) and OER (b) cycles; TEM and SEM images of catalysts on the cathode (c, e) and the anode (d, f) after 10,000 seconds of constant applied current density of 200 mA cm^{-2}.

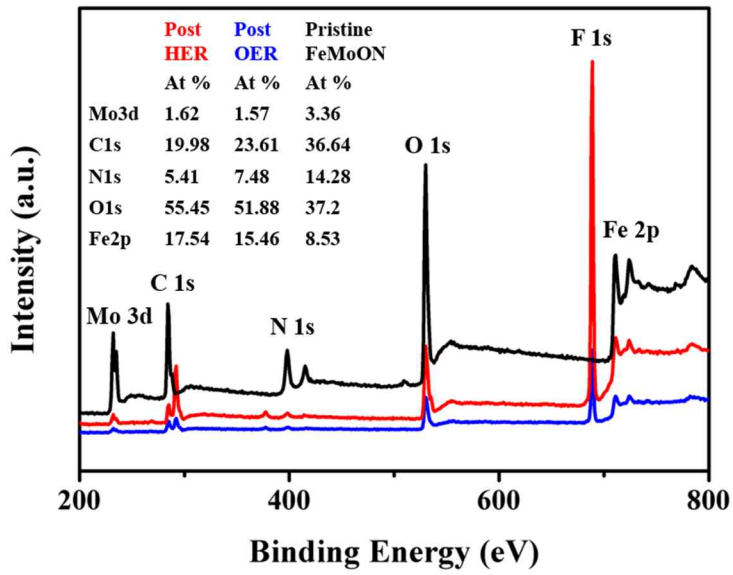

Figure 44 XPS survey of FeMoON in its pristine and post HER/OER.

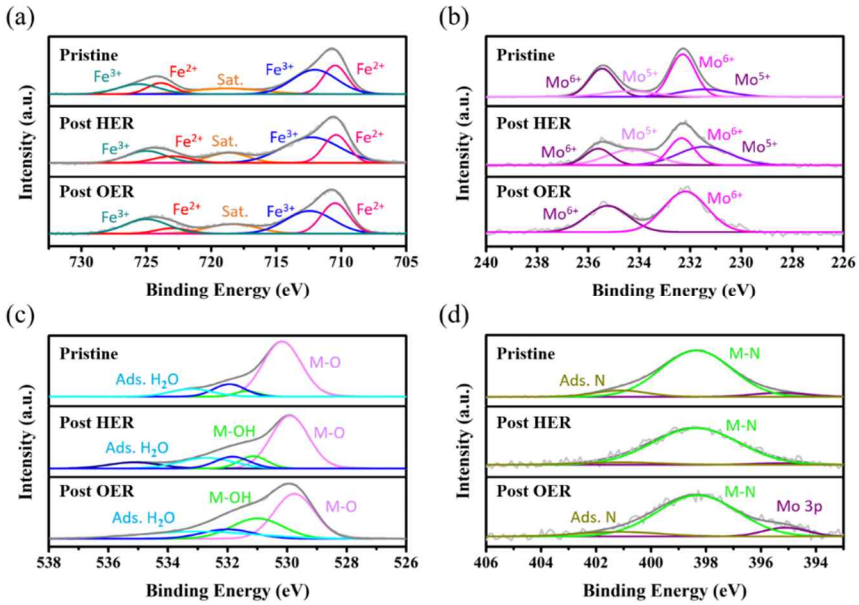

Figure 45 XPS high resolution scan of (a) Fe 2p, (b) Mo 3d, (c) N 1s, and (d) O 1s of FeMoN in pristine and post HER and OER.

The general results manifest that the FeMoON catalyst exhibits excellent catalytic activity and stability towards both HER and OER. The great enhancement in HER and OER performance of FeMoON upon Mo incorporation can be explained with the well-established theories described in the literature. Figure 42 depicts a schematic representation of the proposed mechanism. An optimal HER site of a catalyst would have the Gibbs free energy of hydrogen adsorption close to zero, and it has been demonstrated in previous studies that Mo-dopants effectively reduce the ΔG_{H^*} value to near zero and facilitate free hydrogen adsorption, thus significantly enhancing the HER activity of the catalyst. [70,214,232,233]

As for OER, the mechanism is rather indirect. 3d block Transition metals of high valence state are generally considered as the catalytically active sites for OER for their ability to buffer the multi-electron process of OER.[234–236] Preceding studies have shown that higher valence metals such as Mo^{6+} can induce re-distribution of charges by taking electrons from the neighboring 3d metals. This facilitates oxidation of the 3d metal and lower the oxidation barrier.[236–238] DFT predictions indicated that lower oxidation barrier in 3*d* metals gives higher OER activity.[236,239] Based on these findings, we speculate that the electronic structure of Fe have been modified upon introduction of the

high-valence Mo^{6+} to attain an optimal adsorption energy for the OER intermediates.

The morphologies of FeMoON after a 1000 HER and OER cycles shown in Figure 43 demonstrate fractional disruption in microstructure where the porous micro-rods are partially torn open, but the individual catalyst nanoparticles remain small and well bound to each other without significant signs of aggregation or expansion, most likely owing to the protective carbon shells. Upon intense activation for 10,000 seconds at high constant applied current density of 200 mA cm^{-2}, significant signs of disruption in the microstructure is observed (Figure 43 c-f). The roughened surface is attributed to partial corrosion under alkaline conditions. Nevertheless, TEM images of the catalyst post intense activation still show individual catalyst particles well established in shape and size. Structural characterization of the catalysts post intense activation display significant changes on the surface morphology. This surface reconstruction was further investigated using XPS. XPS surface composition before and after activation is compared in Figure 44. The changes in Fe to Mo ratio is noticeable, implying a significant decrease in Mo from 2.5:1 in pristine to around 10:1 post reactions. Partial leaching of Mo is suspected to have taken place during continuous activation, leading to creation of vacancies and defects that induce

reconstruction of Fe species to form hydroxides and oxyhydroxides on the surface.[240] Figure 45 shows the comparison of the electronic structures (XPS spectra of Fe 2p, Mo 3d, N1s, and O1s) post HER and OER. Slight changes in the oxidation state was observed in Fe 2p and Mo 3d graphs, where the Fe^{3+} peak grew larger after HER and more significantly after OER, and Mo^{5+} peak enlarged after HER and disappeared after OER. The appearance of a large peak at ~531 eV in the O 1 s spectrum is evidence to formation of metal hydroxide after OER, which is a well-known active species in OER. From the observation of N 1s peaks post reactions we can infer that the nitrogen-metal bond stays intact during the HER processes and is partially oxidized after the OER processes, evidenced by the decrease in M-N peak intensity that brings out the Mo 3p peak post OER.

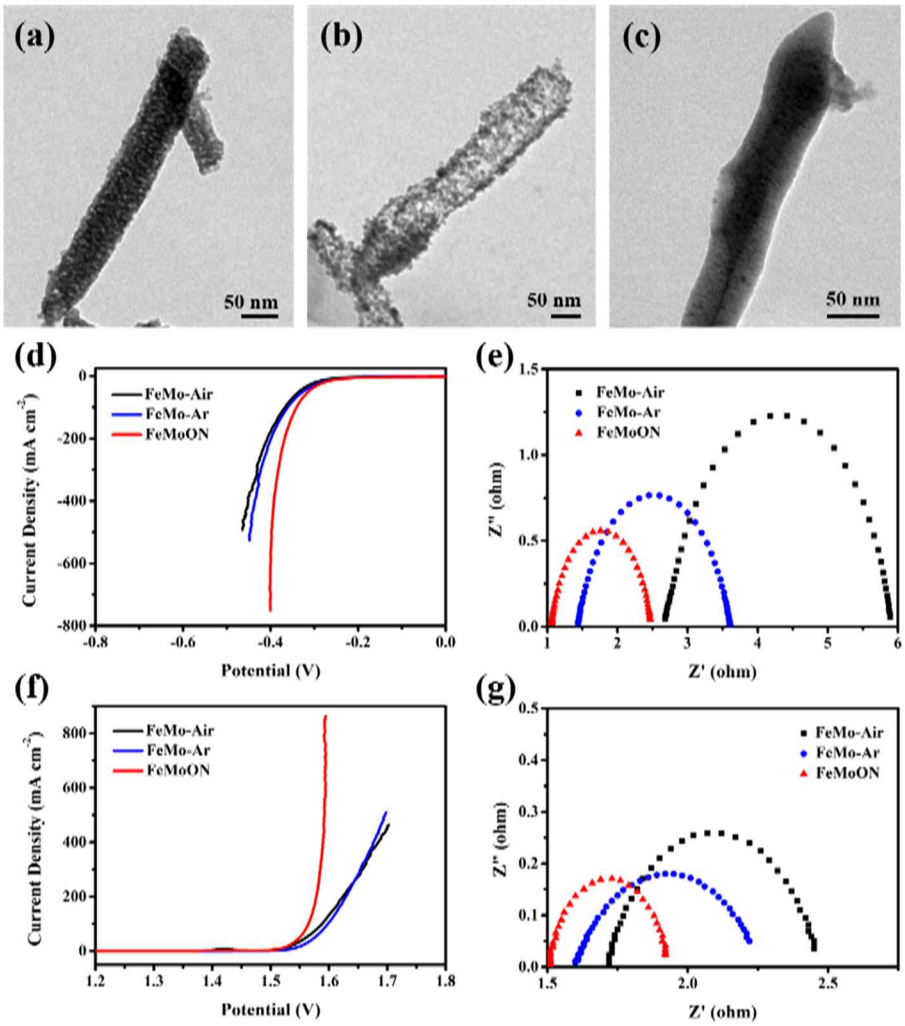

Figure 46 TEM images of FeMo-Air (a), FeMoON (b), FeMo-Ar (c), and their LSV polarization curves (d, f) and Nyquist plots (e, g) for HER (d, e) and OER (f, g).

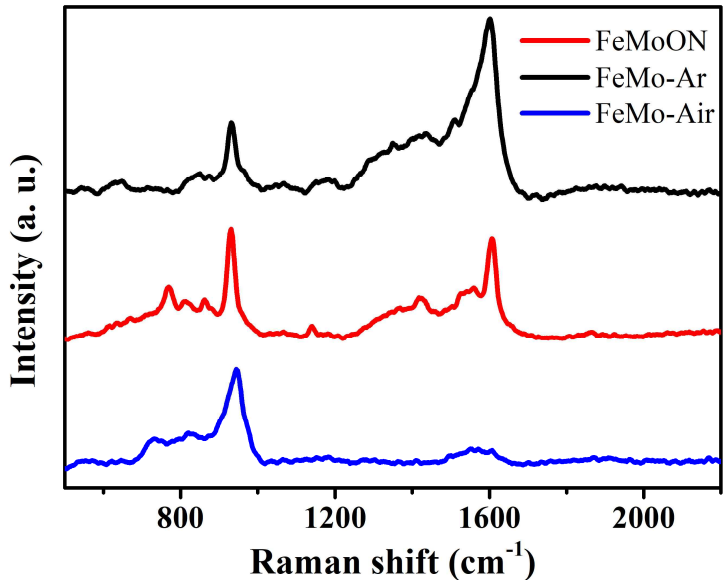

Figure 47 Raman spectra of FeMo-Air, FeMo-Ar, and FeMoON.

In order to clarify the significance of the oxynitride species, FeMo-MIL-88B calcinated in air and argon flow in the absence of urea, denoted as FeMo-Air and FeMo-Ar, were evaluated in comparison with FeMoON (Figure 46). The morphology of FeMo-Air and FeMo-Ar observed from TEM resembles that of FeMoON dimension-wise however, differs greatly in nanoscale; where FeMo-Air is a mesoporous metal oxide rod with pore size of ~5 nm, and FeMo-Ar shows very small metal oxide nanoparticles smaller than 5 nm encapsulated in a thick carbonaceous rod. Figure 47 shows Raman spectra of FeMo-Air, FeMo-Ar, and FeMoON in the range of 500–2200 cm^{-1}. The strong peaks observed around 926 cm^{-1} can be assigned to β-$FeMoO_4$, indicating β-$FeMoO_4$ is the main component in all three atmospheres, consistent with the XRD data.[241] The broad peak at around 1400 cm^{-1} and the sharp peak at 1598 cm^{-1} in FeMo-Ar and FeMoON spectra can be ascribed to the D band and the G band of carbon derived from the organic linkers. The prominent carbon peaks in FeMo-Ar diminishes greatly in FeMoON owing to NH_3-induced chemical decomposition.[86,242] From this result we can infer that FeMo-Ar is large part graphitic carbon that may boost conductivity, FeMoON is oxynitride particles partially coated with graphitic carbon or encapsulated in thin carbon shells, and FeMo-Air is pure oxidic catalysts without any conductive aid.

Shown in Figure 46 d-g are LSV polarization curves and EIS Nyquist plots of FeMo-Air and FeMo-Ar in HER and OER. It is evident that calcination atmosphere plays a significant role in enhancing the catalytic activity of FeMoON, judging from the significantly smaller overpotentials and Nyquist plots compared to those of FeMo-Air and FeMo-Ar, for both HER and OER. Same trend in catalytic property was observed for Fe-MIL-88B derived FeON, Fe-Air, and Fe-Ar (Figure 48). We conclude that the greatly enhanced activity is a synergistic result of oxynitride species and carbon conductive species. Summaries of EIS measurements for FeMoON, FeON, and FeO in HER and OER can be found in Table 9 and 10, respectively. Based on these results, we conclude that the greatly enhanced activity is a synergistic result of oxynitride species and carbon conductive species.

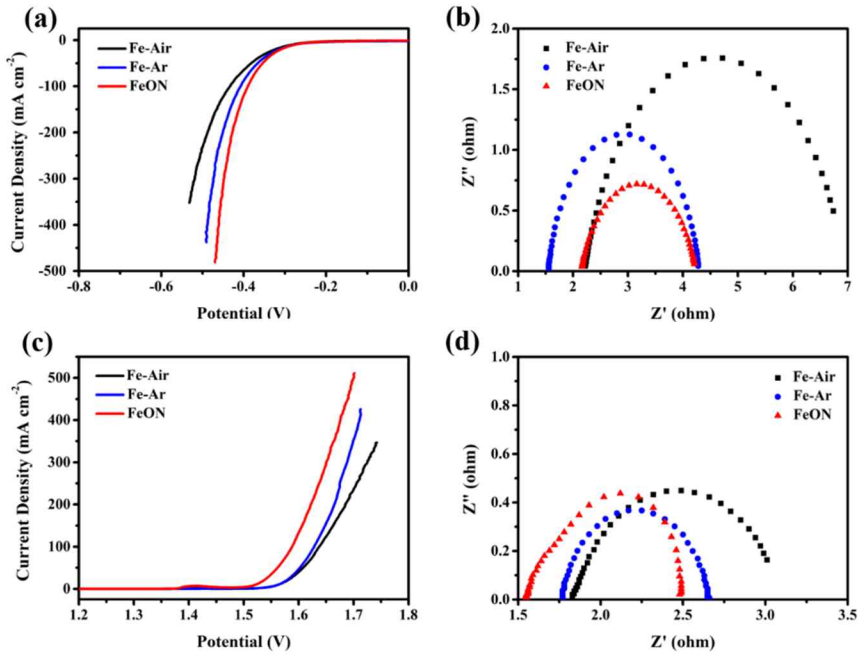

Figure 48 LSV polarization curves (a, c) and Nyquist plots (b, d) of FeON, Fe-Air, and Fe-Ar for HER (a, b) and OER (c, d).

Table 9 EIS summary of FeMoON, FeON, and FeO for HER.

Sample	R_s (Ω/cm^2)	Q_1 (mF/cm^2)	R_1 (Ω/cm^2)	Q_2 (mF/cm^2)	R_{ct} (Ω/cm^2)
FeMoON	1.06	136	0.21	849.5	1.42
FeON	2.15	756.6	2.09	756.6	2.09
FeO	2.17	73.2	65.4	817.1	4.70

Table 10 EIS summary of FeMoON, FeON, and FeO for OER.

Samples	R_s (Ω/cm^2)	Q_1 (mF/cm^2)	R_1 ($m\Omega/cm^2$)	Q_2 (mF/cm^2)	R_{ct} (Ω/cm^2)
FeMoON	1.49	1069	274.7	833.4	0.15
FeON	1.56	894.7	962.0	974.7	0.83
FeO	1.83	777.2	1230	548.6	1.46

Inspired by the satisfying bifunctional characteristics, FeMoON was assembled into a two- electrode alkaline water electrolyzer and was tested for overall water splitting. As plotted in Figure 49, FeMoON electrolyzer attains a high current density of 75 mA cm^{-2} at an applied potential of only 1.8 V, marking a 3.75 times higher value than that of Mo free FeON (20 mA cm^{-2} at 1.8 V). This performance is superior to FeON || FeON and even the commercial RuO2 || Pt/C at current densities higher than 60 mA cm^{-2}. The polarization curves acquired in various scan rates showed almost identical curves within a range of 1 mV s^{-1} to 100 mV s^{-1}, indicating good catalytic activity regardless of the sweep speed (Figure 50). Finally, the gaseous products from the FeMoON || FeMoON pair were collected for Faradaic efficiency evaluation to verify that the amount of gas caused by the flow of current was proportional to the amount of electricity passed. The Faradaic efficiency was calculated by comparing the amount of measured hydrogen and oxygen generated by amperostatic coulometry with calculated hydrogen and oxygen using the below equation, assuming 100% Faradaic efficiency. The FeMoON || FeMoON pair was subjected to a constant applied current at 0.1 A for 10 minutes. The collected gases amounted to 3.5 mL oxygen and 6.5 mL hydrogen, giving 100% and 94% FE, respectively.

$FE = z*n*F/Q$

FE = Faradaic efficiency

z= mol of electrons required to generate a mol of O_2 or H_2

n= mol of H_2 or O_2

F = 96485 (C mol^{-1})

Q = total number of charges passed

Oxygen was found to yield a 100% Faradaic efficiency while hydrogen was calculated to yield 94%. The 6% difference may be related to the side reactions such as surface corrosion of the catalyst. [202]

It is evident from the stability and durability evaluations that the FeMoON || FeMoON electrolyzer can remain stable over 20 hours at a constant applied voltage of 1.8 V and 1000 rapid CV cycles (inset of Figure 49b), indicating that FeMoON || FeMoON system is fit for effective overall water splitting. Compared with the leading transition metal-based electrocatalysts presented in other studies, the FeMoON shows decent performance in HER, OER, and overall water splitting (Table 11).

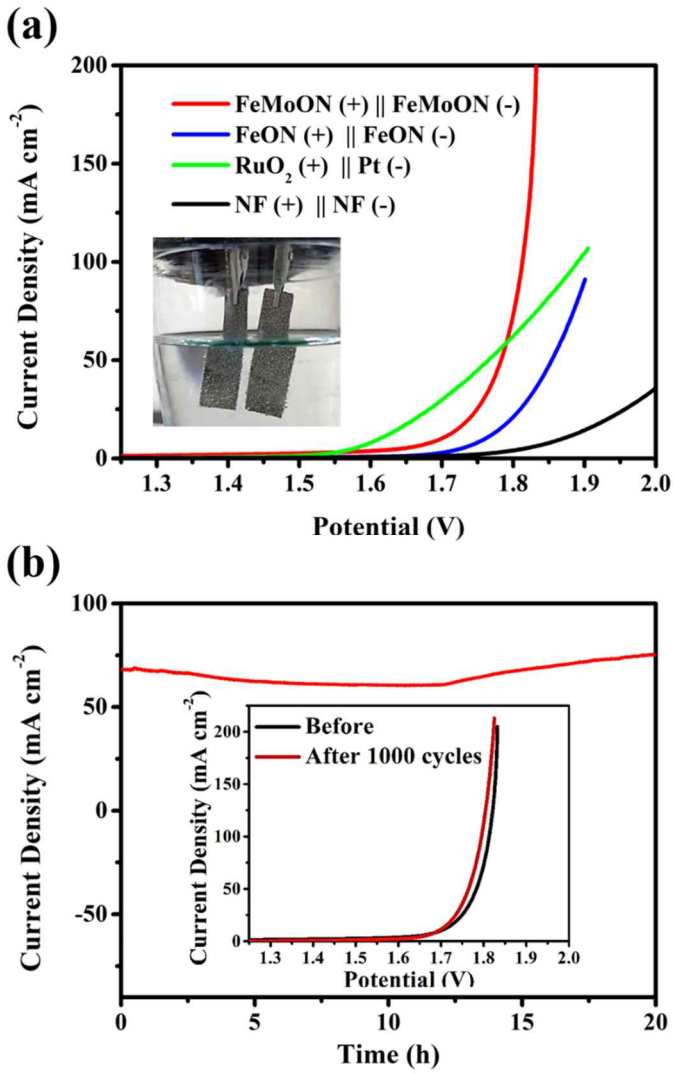

Figure 49 Overall water-splitting performance and stability test of the FeMoON conducted in 1 M KOH. (a) Polarization curve for overall water splitting with FeMoON, FeON, noble metal pair, and Ni foam electrode as both the anode and cathode. (b) Long-term stability test under an applied voltage of 1.8 V. Polarization curves of FeMoON before and after 1000 CV cycles (inset).

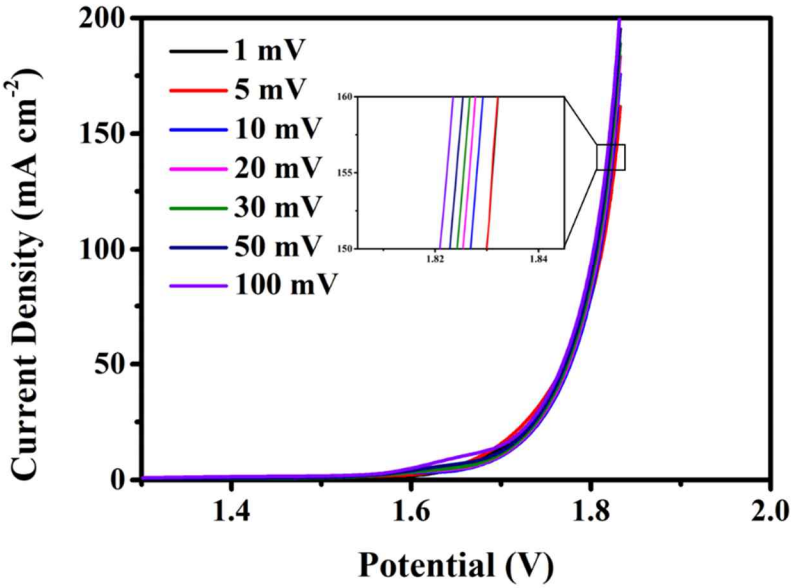

Figure 50 Polarization curves of different sweep speeds from 1 to 100 mV s^{-1}.

Table 11 Summary of HER, OER, and overall water splitting activity of recently reported transition metal-based bifunctional electrocatalysts in comparison with this work.

Bifunctional catalyst	η for HER @ j (mV@mA cm^{-2})	η for OER @ j (mV@mA cm^{-2})	Overall water splitting voltage (V@mA cm^{-2})	Ref.
FeMoON	**340@100** **500@750**	**330@100** **360@850**	**1.73 @20** **1.83@200**	**This work**
NiFeMo	238@10	45@10	~1.8@90	[70]
Fe-Mo-S /Ni_3S_2@NF	144@10 266@100	300@100	1.51@20	[243]
CoS_x/Ni_3S_2 @NF	139@10	373@100	1.57@10	[244]
Fe_2Ni_2N	180@10	~250@45	1.65@10	[245]
Co_4N-$VN_{1-x}O_x$	118@100	263@10	1.64@10	[246]
$MoS_2-Ni_3S_2$ HNRs/NF	98@10	341@100	1.50@10	[247]
Ni_3S_2-NGQDs/NF	218@10	370@100	1.58@10	[248]
Ni_3FeN	69@10	250@20	1.55@10	[213]
Mo-W-S-2@Ni_3S_2-NF	98@10	285@10	1.62@10	[249]
Fe_2N/Fe_3N	146@10	307@10	1.67@10	[211]
$N-Ni_3S_2$/NF	110@10	330@100	1.48@10	[250]
Mo-doped Ni_3S_2@NF	212@10	260@10	1.67@10	[251]

2.2.4 Conclusion

This study demonstrated a rapid microwave-assisted synthesis of uniform rod-like FeMo-MIL-88B microstructures and the excellent catalytic activity of its oxynitride derivate towards HER, OER, and overall water splitting. The catalysts transformed from MIL-88B were tiny nanoparticles confined in the initial porous microstructure, providing multiple active sites and pathway for electrolyte and gas transport. The effect of molybdenum incorporation and oxynitride formation on the electrochemical property and catalytic activity of FeMoON was investigated, and the results show that incorporation of Mo in optimal ratio significantly enhances the catalytic activity by tuning the sluggish Volmer step; and that N-doping significantly boosts water-splitting activity by enhancing charge transfer behavior. Two modifications combined, the optimized FeMoON alkaline water electrolyzer shows catalytic behavior surpassing that of the commercial Pt/C||RuO_2 electrolyzer (1.81 V and 1.89 V, respectively, for current density of 100 mA cm^{-2}). Moreover, FeMoON electrolyzer could bear 1000 cycles of accelerated degradation and 20 hours of constant applied voltage without deterioration in current density, indicating good stability. The result of the present work indicate that FeMoON has good prospect for practical application considering its low cost, ease in preparation,

attractive catalytic activity, and stability.

2.2.5 References

[1] J.B. Goodenough, Energy storage materials: A perspective, Energy Storage Mater. 1 (2015) 158–161. https://doi.org/10.1016/j.ensm.2015.07.001.

[2] A.K. Hossain, P.A. Davies, Pyrolysis liquids and gases as alternative fuels in internal combustion engines - A review, Renew. Sustain. Energy Rev. 21 (2013) 165–189. https://doi.org/10.1016/j.rser.2012.12.031.

[3] V.G. Milt, M.L. Pissarello, E.E. Miró, C.A. Querini, Abatement of diesel-exhaust pollutants: NO_x storage and soot combustion on K/La_2O_3 catalysts, Appl. Catal. B Environ. 41 (2003) 397–414. https://doi.org/10.1016/S0926-3373(02)00175-3.

[4] A.T. Evulet, A.M. ELKady, A.R. Branda, D. Chinn, On the Performance and Operability of GE's Dry Low NO_x Combustors utilizing Exhaust Gas Recirculation for PostCombustion Carbon Capture, Energy Procedia. 1 (2009) 3809–3816. https://doi.org/10.1016/j.egypro.2009.02.182.

[5] K. Holmberg, A. Erdemir, The impact of tribology on energy use and CO_2 emission globally and in combustion engine and electric cars, Tribol. Int. 135 (2019) 389–396. https://doi.org/10.1016/j.triboint.2019.03.024.

[6] E. Loiseau, L. Saikku, R. Antikainen, N. Droste, B. Hansjürgens, K. Pitkänen, P. Leskinen, P. Kuikman, M. Thomsen, Green economy and related concepts: An overview, J. Clean. Prod. 139 (2016) 361–371. https://doi.org/10.1016/j.jclepro.2016.08.024.

[7] A. Pfeiffer, R. Millar, C. Hepburn, E. Beinhocker, The '2°C capital stock' for electricity generation: Committed cumulative carbon emissions from the electricity generation sector and the transition to a green economy, Appl. Energy. 179 (2016) 1395–1408. https://doi.org/10.1016/j.apenergy.2016.02.093.

[8] J. Pretty, The Consumption of a Finite Planet: Well-Being, Convergence, Divergence and the Nascent Green Economy, Environ. Resour. Econ. 55 (2013) 475–499. https://doi.org/10.1007/s10640-013-9680-9.

[9] W.W. Clark, J. Rifkin, A green hydrogen economy, Energy Policy. 34 (2006) 2630–2639. https://doi.org/10.1016/j.enpol.2005.06.024.

[10] IEA (2019), The Future of Hydrogen, IEA, Paris https://www.iea.org/reports/the-future-of-hydrogen.

[11] M.-R. de Valladares, Global Trends and Outlook For Hydrogen, Int. Energy Agency, Paris, Fr. (2017).

[12] M.H.A. Demirel, Yasar, Michael J. Matzen, Technoeconomics and

Sustainability of Renewable Methanol and Ammonia Productions Using Wind Power-based Hydrogen, J. Adv. Chem. Eng. 5 (2015) 1000128. https://doi.org/10.4172/2090-4568.1000128.

[13] A. Haryanto, S. Fernando, N. Murali, S. Adhikari, Current status of hydrogen production techniques by steam reforming of ethanol: A review, Energy and Fuels. 19 (2005) 2098–2106. https://doi.org/10.1021/ef0500538.

[14] A. Boyano, A.M. Blanco-Marigorta, T. Morosuk, G. Tsatsaronis, Exergoenvironmental analysis of a steam methane reforming process for hydrogen production, Energy. 36 (2011) 2202–2214. https://doi.org/10.1016/j.energy.2010.05.020.

[15] P.D. Vaidya, A.E. Rodrigues, Glycerol reforming for hydrogen production: A review, Chem. Eng. Technol. 32 (2009) 1463–1469. https://doi.org/10.1002/ceat.200900120.

[16] IEA (2020), World Energy Model, IEA, Paris https://www.iea.org/reports/world-energy-model.

[17] S. Trasatti, Water electrolysis: Who first?, J. Electroanal. Chem. 476 (1999) 90–91. https://doi.org/10.1016/S0022-0728(99)00364-2.

[18] I.A. Gondal, Hydrogen integration in power-to-gas networks, Int. J. Hydrogen Energy. 44 (2019) 1803–1815. https://doi.org/10.1016/j.ijhydene.2018.11.164.

[19] IEA (2020), Hydrogen, IEA, Paris https://www.iea.org/reports/hydrogen.

[20] J.O. Bockris, E.C. Potter, The Mechanism of the Cathodic Hydrogen Evolution Reaction, J. Electrochem. Soc. 99 (1952) 169. https://doi.org/10.1149/1.2779692.

[21] M. Gennero, U. Nacional, A.C. Chialvo, U. Nacional, Hydrogen evolution reaction : Analysis of the Volmer-Heyrovsky-Tafel mechanism with a generalized adsorption model, 372 (2014) 209–223.

[22] F. Safizadeh, E. Ghali, G. Houlachi, Electrocatalysis developments for hydrogen evolution reaction in alkaline solutions - A Review, Int. J. Hydrogen Energy. 40 (2015) 256–274. https://doi.org/10.1016/j.ijhydene.2014.10.109.

[23] T. Reier, H.N. Nong, D. Teschner, R. Schlögl, P. Strasser, Electrocatalytic Oxygen Evolution Reaction in Acidic Environments – Reaction Mechanisms and Catalysts, Adv. Energy Mater. 7 (2017). https://doi.org/10.1002/aenm.201601275.

[24] F. Lu, M. Zhou, Y. Zhou, X. Zeng, First-Row Transition Metal Based Catalysts for the Oxygen Evolution Reaction under Alkaline Conditions: Basic Principles and Recent Advances, Small. 13 (2017) 1–18.

https://doi.org/10.1002/smll.201701931.
[25] McCafferty E., Thermodynamics of Corrosion: Pourbaix Diagrams.in: Introduction to Corrosion Science, in: Springer, New York, NY., 2010. https://doi.org/https://doi.org/10.1007/978-1-4419-0455-3_6.
[26] A. Savan, S. Cherevko, N. Kulyk, O. Kasian, B. Breitbach, S. Geiger, B.R. Shrestha, J.-P. Grote, K.J.J. Mayrhofer, S. Merzlikin, A. Ludwig, Oxygen and hydrogen evolution reactions on Ru, RuO_2 , Ir, and IrO_2 thin film electrodes in acidic and alkaline electrolytes: A comparative study on activity and stability, Catal. Today. 262 (2015) 170–180. https://doi.org/10.1016/j.cattod.2015.08.014.
[27] D. Xun, H. Hao, X. Sun, Z. Liu, F. Zhao, End-of-life recycling rates of platinum group metals in the automotive industry: Insight into regional disparities, J. Clean. Prod. 266 (2020) 121942. https://doi.org/10.1016/j.jclepro.2020.121942.
[28] Y. Yan, B.Y. Xia, B. Zhao, X. Wang, A review on noble-metal-free bifunctional heterogeneous catalysts for overall electrochemical water splitting, J. Mater. Chem. A. 4 (2016) 17587–17603. https://doi.org/10.1039/C6TA08075H.
[29] F. Lv, J. Feng, K. Wang, Z. Dou, W. Zhang, J. Zhou, C. Yang, M. Luo, Y. Yang, Y. Li, P. Gao, S. Guo, Iridium-Tungsten Alloy Nanodendrites as pH-Universal Water-Splitting Electrocatalysts, ACS Cent. Sci. 4 (2018) 1244–1252. https://doi.org/10.1021/acscentsci.8b00426.
[30] Y. Pi, Q. Shao, P. Wang, J. Guo, X. Huang, General Formation of Monodisperse IrM (M = Ni, Co, Fe) Bimetallic Nanoclusters as Bifunctional Electrocatalysts for Acidic Overall Water Splitting, Adv. Funct. Mater. 27 (2017) 1–8. https://doi.org/10.1002/adfm.201700886.
[31] L. Fu, X. Zeng, G. Cheng, W. Luo, IrCo Nanodendrite as an Efficient Bifunctional Electrocatalyst for Overall Water Splitting under Acidic Conditions, ACS Appl. Mater. Interfaces. 10 (2018) 24993–24998. https://doi.org/10.1021/acsami.8b08717.
[32] J. Feng, F. Lv, W. Zhang, P. Li, K. Wang, C. Yang, B. Wang, Y. Yang, J. Zhou, F. Lin, G.C. Wang, S. Guo, Iridium-Based Multimetallic Porous Hollow Nanocrystals for Efficient Overall-Water-Splitting Catalysis, Adv. Mater. 29 (2017) 1–8. https://doi.org/10.1002/adma.201703798.
[33] Y. Sun, B. Huang, Y. Li, Y. Xing, M. Luo, N. Li, Z. Xia, Y. Qin, D. Su, L. Wang, S. Guo, Trifunctional Fishbone-like PtCo/Ir Enables High-Performance Zinc-Air Batteries to Drive the Water-Splitting Catalysis, Chem. Mater. 31 (2019) 8136–8144. https://doi.org/10.1021/acs.chemmater.9b02892.
[34] J. Shan, T. Ling, K. Davey, Y. Zheng, S.Z. Qiao, Transition-Metal-

Doped RuIr Bifunctional Nanocrystals for Overall Water Splitting in Acidic Environments, Adv. Mater. 31 (2019) 1–7. https://doi.org/10.1002/adma.201900510.

[35] H. Duan, D. Li, Y. Tang, Y. He, S. Ji, R. Wang, H. Lv, P.P. Lopes, A.P. Paulikas, H. Li, S.X. Mao, C. Wang, N.M. Markovic, J. Li, V.R. Stamenkovic, Y. Li, High-Performance Rh_2P Electrocatalyst for Efficient Water Splitting, J. Am. Chem. Soc. 139 (2017) 5494–5502. https://doi.org/10.1021/jacs.7b01376.

[36] Q. Qin, H. Jang, L. Chen, G. Nam, X. Liu, J. Cho, Low Loading of RhxP and RuP on N, P Codoped Carbon as Two Trifunctional Electrocatalysts for the Oxygen and Hydrogen Electrode Reactions, Adv. Energy Mater. 8 (2018) 1–12. https://doi.org/10.1002/aenm.201801478.

[37] H. Sun, Z. Yan, F. Liu, W. Xu, F. Cheng, J. Chen, Self-Supported Transition-Metal-Based Electrocatalysts for Hydrogen and Oxygen Evolution, Adv. Mater. 32 (2020) 1–18. https://doi.org/10.1002/adma.201806326.

[38] IUPAC. Compendium of Chemical Terminology, 2nd ed. (the "Gold Book"). Compiled by A. D. McNaught and A. Wilkinson. Blackwell Scientific Publications, Oxford (1997)., (n.d.). https://doi.org/https://doi.org/10.1351/goldbook.

[39] P. Du, R. Eisenberg, Catalysts made of earth-abundant elements (Co, Ni, Fe) for water splitting: Recent progress and future challenges, Energy Environ. Sci. 5 (2012) 6012–6021. https://doi.org/10.1039/c2ee03250c.

[40] J. Wang, X. Yue, Y. Yang, S. Sirisomboonchai, P. Wang, X. Ma, A. Abudula, G. Guan, Earth-abundant transition-metal-based bifunctional catalysts for overall electrochemical water splitting: A review, J. Alloys Compd. 819 (2020) 153346. https://doi.org/10.1016/j.jallcom.2019.153346.

[41] L. Ma, X. Shen, H. Zhou, J. Zhu, C. Xi, Z. Ji, L. Kong, Synthesis of Cu_3P nanocubes and their excellent electrocatalytic efficiency for the hydrogen evolution reaction in acidic solution, RSC Adv. 6 (2016) 9672–9677. https://doi.org/10.1039/c5ra24427g.

[42] Y. Gong, H. Pan, Z. Xu, Z. Yang, Y. Lin, M. Zhang, ACo2O4 (A=Ni, Zn, Mn) nanostructure arrays grown on nickel foam as efficient electrocatalysts for oxygen evolution reaction, Int. J. Hydrogen Energy. 43 (2018) 14360–14368. https://doi.org/10.1016/j.ijhydene.2018.06.025.

[43] Y. Liu, S. Jiang, S. Li, L. Zhou, Z. Li, J. Li, M. Shao, Interface engineering of (Ni, Fe)S_2@MoS_2 heterostructures for synergetic electrochemical water splitting, Appl. Catal. B Environ. 247 (2019)

107–114. https://doi.org/10.1016/j.apcatb.2019.01.094.

[44] K. Wang, K. Sun, T. Yu, X. Liu, G.X. Wang, L. Jiang, G. Xie, Facile synthesis of nanoporous Ni-Fe-P bifunctional catalysts with high performance for overall water splitting, J. Mater. Chem. A. 7 (2019) 2518–2523. https://doi.org/10.1039/c8ta10856k.

[45] Y. Xu, Y. Yan, T. He, K. Zhan, J. Yang, B. Zhao, K. Qi, B.Y. Xia, Supercritical CO_2 -Assisted synthesis of $NiFe_2O_4$ /vertically-aligned carbon nanotube arrays hybrid as a bifunctional electrocatalyst for efficient overall water splitting, Carbon N. Y. 145 (2019) 201–208. https://doi.org/10.1016/j.carbon.2019.01.011.

[46] R. Elakkiya, R. Ramkumar, G. Maduraiveeran, Flower-like nickel-cobalt oxide nanomaterials as bi-functional catalyst for electrochemical water splitting, Mater. Res. Bull. 116 (2019) 98–105. https://doi.org/10.1016/j.materresbull.2019.04.016.

[47] F. Li, R. Xu, Y. Li, F. Liang, D. Zhang, W.F. Fu, X.J. Lv, N-doped carbon coated $NiCo_2S_4$ hollow nanotube as bifunctional electrocatalyst for overall water splitting, Carbon N. Y. 145 (2019) 521–528. https://doi.org/10.1016/j.carbon.2019.01.065.

[48] Q. Zhang, R.F. Webster, S. Cheong, R.D. Tilley, X. Lu, R. Amal, Ultrathin Fe-N-C Nanosheets Coordinated Fe-Doped CoNi Alloy Nanoparticles for Electrochemical Water Splitting, Part. Part. Syst. Charact. 36 (2019) 1–10. https://doi.org/10.1002/ppsc.201800252.

[49] Y. Wu, X. Tao, Y. Qing, H. Xu, F. Yang, S. Luo, C. Tian, M. Liu, X. Lu, Cr-Doped FeNi–P Nanoparticles Encapsulated into N-Doped Carbon Nanotube as a Robust Bifunctional Catalyst for Efficient Overall Water Splitting, Adv. Mater. 31 (2019) 1–9. https://doi.org/10.1002/adma.201900178.

[50] Z.Y. Wu, W.B. Ji, B.C. Hu, H.W. Liang, X.X. Xu, Z.L. Yu, B.Y. Li, S.H. Yu, Partially oxidized Ni nanoparticles supported on Ni-N co-doped carbon nanofibers as bifunctional electrocatalysts for overall water splitting, Nano Energy. 51 (2018) 286–293. https://doi.org/10.1016/j.nanoen.2018.06.071.

[51] Y. Gong, Y. Zhi, Y. Lin, T. Zhou, J. Li, F. Jiao, W. Wang, Controlled synthesis of bifunctional particle-like Mo/Mn-Ni_xS_y /NF electrocatalyst for highly efficient overall water splitting, Dalt. Trans. 48 (2019) 6718–6729. https://doi.org/10.1039/c9dt00957d.

[52] D. Gao, R. Liu, J. Biskupek, U. Kaiser, Y.F. Song, C. Streb, Modular Design of Noble-Metal-Free Mixed Metal Oxide Electrocatalysts for Complete Water Splitting, Angew. Chemie - Int. Ed. 58 (2019) 4644–4648. https://doi.org/10.1002/anie.201900428.

[53] Y.J. Tang, H.J. Zhu, L.Z. Dong, A.M. Zhang, S.L. Li, J. Liu, Y.Q. Lan, Solid-phase hot-pressing of POMs-ZIFs precursor and derived phosphide for overall water splitting, Appl. Catal. B Environ. 245 (2019) 528–535. https://doi.org/10.1016/j.apcatb.2019.01.007.

[54] S. Li, S. Sirisomboonchai, A. Yoshida, X. An, X. Hao, A. Abudula, G. Guan, Bifunctional CoNi/$CoFe_2O_4$ /Ni foam electrodes for efficient overall water splitting at a high current density, J. Mater. Chem. A. 6 (2018) 19221–19230. https://doi.org/10.1039/c8ta08223e.

[55] Y. Fang, Y. Xue, L. Hui, H. Yu, Y. Liu, C. Xing, F. Lu, F. He, H. Liu, Y. Li, In situ growth of graphdiyne based heterostructure: Toward efficient overall water splitting, Nano Energy. 59 (2019) 591–597. https://doi.org/10.1016/j.nanoen.2019.03.022.

[56] S. Dutta, A. Indra, Y. Feng, H.S. Han, T. Song, Promoting electrocatalytic overall water splitting with nanohybrid of transition metal nitride-oxynitride, Appl. Catal. B Environ. 241 (2019) 521–527. https://doi.org/10.1016/j.apcatb.2018.09.061.

[57] M. Higashi, K. Domen, R. Abe, Highly stable water splitting on oxynitride TaON photoanode system under visible light irradiation, J. Am. Chem. Soc. 134 (2012) 6968–6971. https://doi.org/10.1021/ja302059g.

[58] M. Yu, Y. Han, X. Cheng, L. Hu, Y. Zeng, M. Chen, F. Cheng, X. Lu, Y. Tong, Holey tungsten oxynitride nanowires: Novel anodes efficiently integrate microbial chemical energy conversion and electrochemical energy storage, Adv. Mater. 27 (2015) 3085–3091. https://doi.org/10.1002/adma.201500493.

[59] P. Wang, T. Jia, B. Wang, A critical review: 1D/2D nanostructured self-supported electrodes for electrochemical water splitting, J. Power Sources. 474 (2020) 228621. https://doi.org/10.1016/j.jpowsour.2020.228621.

[60] S. Gupta, M.K. Patel, A. Miotello, N. Patel, Metal Boride-Based Catalysts for Electrochemical Water-Splitting: A Review, Adv. Funct. Mater. 30 (2020). https://doi.org/10.1002/adfm.201906481.

[61] T. Meng, M. Cao, Transition Metal Carbide Complex Architectures for Energy-Related Applications, Chem. - A Eur. J. 24 (2018) 16716–16736. https://doi.org/10.1002/chem.201801912.

[62] M.S. Balogun, Y. Huang, W. Qiu, H. Yang, H. Ji, Y. Tong, Updates on the development of nanostructured transition metal nitrides for electrochemical energy storage and water splitting, Mater. Today. 20 (2017) 425–451. https://doi.org/10.1016/j.mattod.2017.03.019.

[63] I. Concina, Z.H. Ibupoto, A. Vomiero, Semiconducting metal oxide

nanostructures for water splitting and photovoltaics, Adv. Energy Mater. 7 (2017) 1–29. https://doi.org/10.1002/aenm.201700706.

[64] Y. Shi, B. Zhang, Recent advances in transition metal phosphide nanomaterials: Synthesis and applications in hydrogen evolution reaction, Chem. Soc. Rev. 45 (2016) 1529–1541. https://doi.org/10.1039/c5cs00434a.

[65] Y. Guo, T. Park, J.W. Yi, J. Henzie, J. Kim, Z. Wang, B. Jiang, Y. Bando, Y. Sugahara, J. Tang, Y. Yamauchi, Nanoarchitectonics for Transition-Metal-Sulfide-Based Electrocatalysts for Water Splitting, Adv. Mater. 31 (2019) 1–34. https://doi.org/10.1002/adma.201807134.

[66] M.E. Kreider, M.B. Stevens, Y. Liu, A.M. Patel, M.J. Statt, B.M. Gibbons, A. Gallo, M. Ben-Naim, A. Mehta, R.C. Davis, A. V Ievlev, J.K. Nørskov, R. Sinclair, L.A. King, T.F. Jaramillo, Nitride or Oxynitride? Elucidating the Composition-Activity Relationships in Molybdenum Nitride Electrocatalysts for the Oxygen Reduction Reaction, Chem. Mater. (2020). https://doi.org/10.1021/acs.chemmater.9b05212.

[67] J. Kibsgaard, I. Chorkendorff, Considerations for the scaling-up of water splitting catalysts, Nat. Energy. 4 (2019) 430–433. https://doi.org/10.1038/s41560-019-0407-1.

[68] X. Peng, Y. Yan, X. Jin, C. Huang, W. Jin, B. Gao, P.K. Chu, Recent advance and prospectives of electrocatalysts based on transition metal selenides for efficient water splitting, Nano Energy. 78 (2020) 105234. https://doi.org/10.1016/j.nanoen.2020.105234.

[69] C.T. Hsieh, C.L. Huang, Y.A. Chen, S.Y. Lu, NiFeMo alloy inverse-opals on Ni foam as outstanding bifunctional catalysts for electrolytic water splitting of ultra-low cell voltages at high current densities, Appl. Catal. B Environ. 267 (2020) 118376. https://doi.org/10.1016/j.apcatb.2019.118376.

[70] F. Qin, Z. Zhao, M.K. Alam, Y. Ni, F. Robles-Hernandez, L. Yu, S. Chen, Z. Ren, Z. Wang, J. Bao, Trimetallic NiFeMo for Overall Electrochemical Water Splitting with a Low Cell Voltage, ACS Energy Lett. 3 (2018) 546–554. https://doi.org/10.1021/acsenergylett.7b01335.

[71] H. Furukawa, K.E. Cordova, M. O'Keeffe, O.M. Yaghi, The chemistry and applications of metal-organic frameworks, Science (80-.). 341 (2013). https://doi.org/10.1126/science.1230444.

[72] J. Liu, D.D. Zhu, C.X. Guo, A. Vasileff, S.Z. Qiao, Design strategies toward advanced mof-derived electrocatalysts for energy-conversion reactions, Adv. Energy Mater. 7 (2017) 1–26. https://doi.org/10.1002/aenm.201700518.

[73] N.L. Torad, M. Hu, S. Ishihara, H. Sukegawa, A.A. Belik, M. Imura, K. Ariga, Y. Sakka, Y. Yamauchi, Direct synthesis of MOF-derived nanoporous carbon with magnetic Co nanoparticles toward efficient water treatment, Small. 10 (2014) 2096–2107. https://doi.org/10.1002/smll.201302910.

[74] J.L.C. Rowsell, O.M. Yaghi, Strategies for hydrogen storage in metal-organic frameworks, Angew. Chemie - Int. Ed. 44 (2005) 4670–4679. https://doi.org/10.1002/anie.200462786.

[75] B. Chen, N.W. Ockwig, A.R. Millward, D.S. Contreras, O.M. Yaghi, High H_2 adsorption in a microporous metal-organic framework with open metal sites, Angew. Chemie - Int. Ed. 44 (2005) 4745–4749. https://doi.org/10.1002/anie.200462787.

[76] Z. Guo, H. Xu, S. Su, J. Cai, S. Dang, S. Xiang, G. Qian, H. Zhang, M. O'keeffe, B. Chen, A robust near infrared luminescent ytterbium metal-organic framework for sensing of small molecules, Chem. Commun. 47 (2011) 5551–5553. https://doi.org/10.1039/c1cc10897b.

[77] P. Horcajada, T. Chalati, C. Serre, B. Gillet, C. Sebrie, T. Baati, J.F. Eubank, D. Heurtaux, P. Clayette, C. Kreuz, J.S. Chang, Y.K. Hwang, V. Marsaud, P.N. Bories, L. Cynober, S. Gil, G. Férey, P. Couvreur, R. Gref, Porous metal-organic-framework nanoscale carriers as a potential platform for drug deliveryand imaging, Nat. Mater. 9 (2010) 172–178. https://doi.org/10.1038/nmat2608.

[78] N. Kornienko, Y. Zhao, C.S. Kley, C. Zhu, D. Kim, S. Lin, C.J. Chang, O.M. Yaghi, P. Yang, Metal-Organic Frameworks for Electrocatalytic Reduction of Carbon Dioxide, J. Am. Chem. Soc. 137 (2015) 14129–14135. https://doi.org/10.1021/jacs.5b08212.

[79] L. Yang, S. Kinoshita, T. Yamada, S. Kanda, H. Kitagawa, M. Tokunaga, T. Ishimoto, T. Ogura, R. Nagumo, A. Miyamoto, M. Koyama, A Metal-Organic Framework as an Electrocatalyst for Ethanol Oxidation, Angew. Chemie - Int. Ed. 49 (2010) 5348–5351. https://doi.org/10.1002/anie.201000863.

[80] B. Li, K. Leng, Y. Zhang, J.J. Dynes, J. Wang, Y. Hu, D. Ma, Z. Shi, L. Zhu, D. Zhang, Y. Sun, M. Chrzanowski, S. Ma, Metal-organic framework based upon the synergy of a Brønsted acid framework and Lewis acid centers as a highly efficient heterogeneous catalyst for fixed-bed reactions, J. Am. Chem. Soc. 137 (2015) 4243–4248. https://doi.org/10.1021/jacs.5b01352.

[81] A. Aijaz, N. Fujiwara, Q. Xu, From Metal − Organic Framework to Nitrogen-Decorated Nanoporous Carbons: High CO_2 Uptake and Effi cient Catalytic Oxygen Reduction, (2014).

[82] I.A. Khan, Y. Qian, A. Badshah, M.A. Nadeem, D. Zhao, Highly Porous Carbon Derived from MOF-5 as a Support of ORR Electrocatalysts for Fuel Cells, ACS Appl. Mater. Interfaces. 8 (2016) 17268–17275. https://doi.org/10.1021/acsami.6b04548.

[83] Q. Lai, Y. Zhao, Y. Liang, J. He, J. Chen, In Situ Confinement Pyrolysis Transformation of ZIF-8 to Nitrogen-Enriched Meso-Microporous Carbon Frameworks for Oxygen Reduction, Adv. Funct. Mater. 26 (2016) 8334–8344. https://doi.org/10.1002/adfm.201603607.

[84] H.X. Zhong, J. Wang, Y.W. Zhang, W.L. Xu, W. Xing, D. Xu, Y.F. Zhang, X.B. Zhang, ZIF-8 derived graphene-based nitrogen-doped porous carbon sheets as highly efficient and durable oxygen reduction electrocatalysts, Angew. Chemie - Int. Ed. 53 (2014) 14235–14239. https://doi.org/10.1002/anie.201408990.

[85] T.Y. Ma, S. Dai, M. Jaroniec, S.Z. Qiao, Metal-organic framework derived hybrid Co_3O_4-carbon porous nanowire arrays as reversible oxygen evolution electrodes, J. Am. Chem. Soc. 136 (2014) 13925–13931. https://doi.org/10.1021/ja5082553.

[86] T. Wang, Q. Zhou, X. Wang, J. Zheng, X. Li, MOF-derived surface modified Ni nanoparticles as an efficient catalyst for the hydrogen evolution reaction, J. Mater. Chem. A. 3 (2015) 16435–16439. https://doi.org/10.1039/C5TA04001A.

[87] P. Yin, T. Yao, Y. Wu, L. Zheng, Y. Lin, W. Liu, H. Ju, J. Zhu, X. Hong, Z. Deng, G. Zhou, S. Wei, Y. Li, Single Cobalt Atoms with Precise N-Coordination as Superior Oxygen Reduction Reaction Catalysts, Angew. Chemie. 128 (2016) 10958–10963. https://doi.org/10.1002/ange.201604802.

[88] B.Y. Guan, L. Yu, X.W. Lou, A dual-metal-organic-framework derived electrocatalyst for oxygen reduction, Energy Environ. Sci. 9 (2016) 3092–3096. https://doi.org/10.1039/c6ee02171a.

[89] M. Hu, J. Reboul, S. Furukawa, N.L. Torad, Q. Ji, P. Srinivasu, K. Ariga, S. Kitagawa, Y. Yamauchi, Direct carbonization of Al-based porous coordination polymer for synthesis of nanoporous carbon, J. Am. Chem. Soc. 134 (2012) 2864–2867. https://doi.org/10.1021/ja208940u.

[90] B. Liu, H. Shioyama, T. Akita, Q. Xu, Metal-organic framework as a template for porous carbon synthesis, J. Am. Chem. Soc. 130 (2008) 5390–5391. https://doi.org/10.1021/ja7106146.

[91] H.L. Jiang, B. Liu, Y.Q. Lan, K. Kuratani, T. Akita, H. Shioyama, F. Zong, Q. Xu, From metal-organic framework to nanoporous carbon: Toward a very high surface area and hydrogen uptake, J. Am. Chem. Soc. 133 (2011) 11854–11857. https://doi.org/10.1021/ja203184k.

[92] F. Meng, H. Zhong, D. Bao, J. Yan, X. Zhang, In Situ Coupling of Strung Co_4N and Intertwined N-C Fibers toward Free-Standing Bifunctional Cathode for Robust, Efficient, and Flexible Zn-Air Batteries, J. Am. Chem. Soc. 138 (2016) 10226–10231. https://doi.org/10.1021/jacs.6b05046.

[93] S. You, X. Gong, W. Wang, D. Qi, X. Wang, X. Chen, N. Ren, Enhanced Cathodic Oxygen Reduction and Power Production of Microbial Fuel Cell Based on Noble-Metal-Free Electrocatalyst Derived from Metal-Organic Frameworks, Adv. Energy Mater. 6 (2016) 1–9. https://doi.org/10.1002/aenm.201501497.

[94] H. Tang, S. Cai, S. Xie, Z. Wang, Y. Tong, M. Pan, X. Lu, Metal-organic-framework-derived dual metal-and nitrogen-doped carbon as efficient and robust oxygen reduction reaction catalysts for microbial fuel cells, Adv. Sci. 3 (2015) 1–8. https://doi.org/10.1002/advs.201500265.

[95] L. Zhou, J. Meng, P. Li, Z. Tao, L. Mai, J. Chen, Ultrasmall cobalt nanoparticles supported on nitrogen-doped porous carbon nanowires for hydrogen evolution from ammonia borane, Mater. Horizons. 4 (2017) 268–273. https://doi.org/10.1039/c6mh00534a.

[96] J. Xi, Y. Xia, Y. Xu, J. Xiao, S. Wang, (Fe,Co)@nitrogen-doped graphitic carbon nanocubes derived from polydopamine-encapsulated metal-organic frameworks as a highly stable and selective non-precious oxygen reduction electrocatalyst, Chem. Commun. 51 (2015) 10479–10482. https://doi.org/10.1039/c5cc03946k.

[97] X. Xing, Y. Song, W. Jiang, X. Zhang, CuFe-P from a Prussian blue analogue as an electrocatalyst for efficient full water splitting, Sustain. Energy Fuels. 4 (2020) 3985–3991. https://doi.org/10.1039/d0se00402b.

[98] L.M. Cao, D. Lu, D.C. Zhong, T.B. Lu, Prussian blue analogues and their derived nanomaterials for electrocatalytic water splitting, Coord. Chem. Rev. 407 (2020) 213156. https://doi.org/10.1016/j.ccr.2019.213156.

[99] J. Chen, Y. Yang, J. Su, P. Jiang, G. Xia, Q. Chen, Enhanced activity for hydrogen evolution reaction over CoFe catalysts by alloying with small amount of Pt, ACS Appl. Mater. Interfaces. 9 (2017) 3596–3601. https://doi.org/10.1021/acsami.6b12065.

[100] H. Zhang, Z. Ma, G. Liu, L. Shi, J. Tang, H. Pang, K. Wu, T. Takei, J. Zhang, Y. Yamauchi, J. Ye, Highly active nonprecious metal hydrogen evolution electrocatalyst: ultrafine molybdenum carbide nanoparticles embedded into a 3D nitrogen-implanted carbon matrix, NPG Asia Mater. 8 (2016) e293. https://doi.org/10.1038/am.2016.102.

[101] H. Bin Wu, B.Y. Xia, L. Yu, X.Y. Yu, X.W. Lou, Porous molybdenum

carbide nano-octahedrons synthesized via confined carburization in metal-organic frameworks for efficient hydrogen production, Nat. Commun. 6 (2015) 1–8. https://doi.org/10.1038/ncomms7512.

[102] M. Qamar, A. Adam, B. Merzougui, A. Helal, O. Abdulhamid, M.N. Siddiqui, Metal-organic framework-guided growth of Mo_2C embedded in mesoporous carbon as a high-performance and stable electrocatalyst for the hydrogen evolution reaction, J. Mater. Chem. A. 4 (2016) 16225–16232. https://doi.org/10.1039/c6ta06553h.

[103] Y. Liu, X. Zhou, T. Ding, C. Wang, Q. Yang, 3D architecture constructed via the confined growth of MoS_2 nanosheets in nanoporous carbon derived from metal-organic frameworks for efficient hydrogen production, Nanoscale. 7 (2015) 18004–18009. https://doi.org/10.1039/c5nr03810c.

[104] J. Sen Li, Y.J. Tang, C.H. Liu, S.L. Li, R.H. Li, L.Z. Dong, Z.H. Dai, J.C. Bao, Y.Q. Lan, Polyoxometalate-based metal-organic framework-derived hybrid electrocatalysts for highly efficient hydrogen evolution reaction, J. Mater. Chem. A. 4 (2016) 1202–1207. https://doi.org/10.1039/c5ta09743f.

[105] Z.F. Huang, J. Song, K. Li, M. Tahir, Y.T. Wang, L. Pan, L. Wang, X. Zhang, J.J. Zou, Hollow Cobalt-Based Bimetallic Sulfide Polyhedra for Efficient All-pH-Value Electrochemical and Photocatalytic Hydrogen Evolution, J. Am. Chem. Soc. 138 (2016) 1359–1365. https://doi.org/10.1021/jacs.5b11986.

[106] T. Tian, L. Ai, J. Jiang, Metal-organic framework-derived nickel phosphides as efficient electrocatalysts toward sustainable hydrogen generation from water splitting, RSC Adv. 5 (2015) 10290–10295. https://doi.org/10.1039/c4ra15680c.

[107] J. Chen, G. Xia, P. Jiang, Y. Yang, R. Li, R. Shi, J. Su, Q. Chen, Active and Durable Hydrogen Evolution Reaction Catalyst Derived from Pd-Doped Metal-Organic Frameworks, ACS Appl. Mater. Interfaces. 8 (2016) 13378–13383. https://doi.org/10.1021/acsami.6b01266.

[108] T. Wu, M. Pi, X. Wang, D. Zhang, S. Chen, Three-dimensional metal-organic framework derived porous CoP_3 concave polyhedrons as superior bifunctional electrocatalysts for the evolution of hydrogen and oxygen, Phys. Chem. Chem. Phys. 19 (2017) 2104–2110. https://doi.org/10.1039/c6cp07294a.

[109] M. Liu, J. Li, Cobalt Phosphide Hollow Polyhedron as Efficient Bifunctional Electrocatalysts for the Evolution Reaction of Hydrogen and Oxygen, ACS Appl. Mater. Interfaces. 8 (2016) 2158–2165. https://doi.org/10.1021/acsami.5b10727.

[110] Z. Shi, Y. Wang, H. Lin, H. Zhang, M. Shen, S. Xie, Y. Zhang, Q. Gao, Y. Tang, Porous nanoMoC@graphite shell derived from a MOFs-directed strategy: An efficient electrocatalyst for the hydrogen evolution reaction, J. Mater. Chem. A. 4 (2016) 6006–6013. https://doi.org/10.1039/c6ta01900e.

[111] L. Jiao, Y.X. Zhou, H.L. Jiang, Metal-organic framework-based CoP/reduced graphene oxide: High-performance bifunctional electrocatalyst for overall water splitting, Chem. Sci. 7 (2016) 1690–1695. https://doi.org/10.1039/c5sc04425a.

[112] M. Xu, L. Han, Y. Han, Y. Yu, J. Zhai, S. Dong, Porous CoP concave polyhedron electrocatalysts synthesized from metal-organic frameworks with enhanced electrochemical properties for hydrogen evolution, J. Mater. Chem. A. 3 (2015) 21471–21477. https://doi.org/10.1039/c5ta05018a.

[113] J. Hao, W. Yang, Z. Zhang, J. Tang, Metal-organic frameworks derived $Co_xFe_{1-x}P$ nanocubes for electrochemical hydrogen evolution, Nanoscale. 7 (2015) 11055–11062. https://doi.org/10.1039/c5nr01955a.

[114] X. Li, Y. Fang, X. Lin, M. Tian, X. An, Y. Fu, R. Li, J. Jin, J. Ma, MOF derived Co_3O_4 nanoparticles embedded in N-doped mesoporous carbon layer/MWCNT hybrids: Extraordinary bi-functional electrocatalysts for OER and ORR, J. Mater. Chem. A. 3 (2015) 17392–17402. https://doi.org/10.1039/c5ta03900b.

[115] B. Chen, G. Ma, Y. Zhu, J. Wang, W. Xiong, Y. Xia, Metal-organic-framework-derived bi-metallic sulfide on N, S-codoped porous carbon nanocomposites as multifunctional electrocatalysts, J. Power Sources. 334 (2016) 112–119. https://doi.org/10.1016/j.jpowsour.2016.10.022.

[116] S. Dou, X. Li, L. Tao, J. Huo, S. Wang, Cobalt nanoparticle-embedded carbon nanotube/porous carbon hybrid derived from MOF-encapsulated Co_3O_4 for oxygen electrocatalysis, Chem. Commun. 52 (2016) 9727–9730. https://doi.org/10.1039/c6cc05244d.

[117] Y. Fang, X. Li, F. Li, X. Lin, M. Tian, X. Long, X. An, Y. Fu, J. Jin, J. Ma, Self-assembly of cobalt-centered metal organic framework and multiwalled carbon nanotubes hybrids as a highly active and corrosion-resistant bifunctional oxygen catalyst, J. Power Sources. 326 (2016) 50–59. https://doi.org/10.1016/j.jpowsour.2016.06.114.

[118] Q. Dong, Q. Wang, Z. Dai, H. Qiu, X. Dong, MOF-Derived Zn-Doped $CoSe_2$ as an Efficient and Stable Free-Standing Catalyst for Oxygen Evolution Reaction, ACS Appl. Mater. Interfaces. 8 (2016) 26902–26907. https://doi.org/10.1021/acsami.6b10160.

[119] Z. Tao, T. Wang, X. Wang, J. Zheng, X. Li, MOF-Derived Noble Metal

Free Catalysts for Electrochemical Water Splitting, ACS Appl. Mater. Interfaces. 8 (2016) 35390–35397. https://doi.org/10.1021/acsami.6b13411.
[120] M.K. Debe, Electrocatalyst approaches and challenges for automotive fuel cells, Nature. 486 (2012) 43–51. https://doi.org/10.1038/nature11115.
[121] S. Jin, Are Metal Chalcogenides, Nitrides, and Phosphides Oxygen Evolution Catalysts or Bifunctional Catalysts?, ACS Energy Lett. 2 (2017) 1937–1938. https://doi.org/10.1021/acsenergylett.7b00679.
[122] Y.P. Zhu, C. Guo, Y. Zheng, S.Z. Qiao, Surface and Interface Engineering of Noble-Metal-Free Electrocatalysts for Efficient Energy Conversion Processes, Acc. Chem. Res. 50 (2017) 915–923. https://doi.org/10.1021/acs.accounts.6b00635.
[123] S. Phenomena, Oxygen evolution reaction on thermally treated iridium oxide films, J. Appl. Electrochem. 17 (1987) 737–745.
[124] M. Amiri, M. Fallahi, A. Bezaatpour, R. Jijie, M. Nozari-Asbmarz, M. Rouhi, R. Boukherroub, S. Szunerits, Solution Processable Cu(II)macrocycle for the Formation of Cu_2O Thin Film on Indium Tin Oxide and Its Application for Water Oxidation, J. Phys. Chem. C. 122 (2018) 16510–16518. https://doi.org/10.1021/acs.jpcc.8b02808.
[125] K.A. Stoerzinger, O. Diaz-Morales, M. Kolb, R.R. Rao, R. Frydendal, L. Qiao, X.R. Wang, N.B. Halck, J. Rossmeisl, H.A. Hansen, T. Vegge, I.E.L. Stephens, M.T.M. Koper, Y. Shao-Horn, Orientation-Dependent Oxygen Evolution on RuO_2 without Lattice Exchange, ACS Energy Lett. 2 (2017) 876–881. https://doi.org/10.1021/acsenergylett.7b00135.
[126] T. Reier, M. Oezaslan, P. Strasser, Electrocatalytic oxygen evolution reaction (OER) on Ru, Ir, and pt catalysts: A comparative study of nanoparticles and bulk materials, ACS Catal. 2 (2012) 1765–1772. https://doi.org/10.1021/cs3003098.
[127] F. Song, L. Bai, A. Moysiadou, S. Lee, C. Hu, L. Liardet, X. Hu, Transition Metal Oxides as Electrocatalysts for the Oxygen Evolution Reaction in Alkaline Solutions: An Application-Inspired Renaissance, J. Am. Chem. Soc. 140 (2018) 7748–7759. https://doi.org/10.1021/jacs.8b04546.
[128] M.S. Ahmed, B. Choi, Y.B. Kim, Development of Highly Active Bifunctional Electrocatalyst Using Coon Carbon Nanotubes for Oxygen Reduction and Oxygen Evolution, Sci. Rep. 8 (2018) 2543. https://doi.org/10.1038/s41598-018-20974-1.
[129] G. Cai, W. Zhang, L. Jiao, S.H. Yu, H.L. Jiang, Template-Directed Growth of Well-Aligned MOF Arrays and Derived Self-Supporting

Electrodes for Water Splitting, Chem. 2 (2017) 791–802. https://doi.org/10.1016/j.chempr.2017.04.016.

[130] F. Bu, W. Chen, M.F. Aly Aboud, I. Shakir, J. Gu, Y. Xu, Microwave-assisted ultrafast synthesis of adjustable bimetal phosphide/graphene heterostructures from MOFs for efficient electrochemical water splitting, J. Mater. Chem. A. 7 (2019) 14526–14535. https://doi.org/10.1039/c9ta03146d.

[131] H. Xu, K. Ye, K. Zhu, J. Yin, J. Yan, G. Wang, D. Cao, Template-directed assembly of urchin-like CoS_x/Co-MOF as an efficient bifunctional electrocatalyst for overall water and urea electrolysis, Inorg. Chem. Front. 7 (2020) 2602–2610. https://doi.org/10.1039/d0qi00408a.

[132] Y. Tan, H. Wang, P. Liu, Y. Shen, C. Cheng, A. Hirata, T. Fujita, Z. Tang, M. Chen, Versatile nanoporous bimetallic phosphides towards electrochemical water splitting, Energy Environ. Sci. 9 (2016) 2257–2261. https://doi.org/10.1039/c6ee01109h.

[133] I. Park, K. Yoo, R.D. Alorro, M.S. Kim, S.K. Kim, Leaching of copper from cuprous oxide in aerated sulfuric acid, Mater. Trans. 58 (2017) 1500–1504. https://doi.org/10.2320/matertrans.M2017147.

[134] D.A. Palmer, Solubility measurements of crystalline Cu_2O in aqueous solution as a function of temperature and pH, J. Solution Chem. 40 (2011) 1067–1093. https://doi.org/10.1007/s10953-011-9699-x.

[135] F.D. Speck, S. Cherevko, Electrochemical copper dissolution: A benchmark for stable CO_2 reduction on copper electrocatalysts, Electrochem. Commun. 115 (2020) 106739. https://doi.org/10.1016/j.elecom.2020.106739.

[136] X. Fan, Z. Li, A. Meng, C. Li, Z. Wu, P. Yan, Improving the Thermal Stability of Cu_3N Films by Addition of Mn, J. Mater. Sci. Technol. 31 (2015) 822–827. https://doi.org/10.1016/j.jmst.2015.07.013.

[137] L.C. Wang, B.H. Liu, C.Y. Su, W.S. Liu, C.C. Kei, K.W. Wang, T.P. Perng, Electronic band structure and electrocatalytic performance of Cu_3N nanocrystals, ACS Appl. Nano Mater. 1 (2018) 3673–3681. https://doi.org/10.1021/acsanm.8b00787.

[138] J. Hou, Y. Sun, Z. Li, B. Zhang, S. Cao, Y. Wu, Z. Gao, L. Sun, Electrical Behavior and Electron Transfer Modulation of Nickel–Copper Nanoalloys Confined in Nickel–Copper Nitrides Nanowires Array Encapsulated in Nitrogen-Doped Carbon Framework as Robust Bifunctional Electrocatalyst for Overall Water Splitting, Adv. Funct. Mater. 28 (2018) 23–25. https://doi.org/10.1002/adfm.201803278.

[139] C. Panda, P.W. Menezes, M. Zheng, S. Orthmann, M. Driess, In Situ Formation of Nanostructured Core-Shell Cu_3N-CuO to Promote

Alkaline Water Electrolysis, ACS Energy Lett. 4 (2019) 747–754. https://doi.org/10.1021/acsenergylett.9b00091.

[140] Q. Wang, Z. Zhang, X. Zhao, J. Xiao, D. Manoj, F. Wei, F. Xiao, H. Wang, S. Wang, MOF-Derived Copper Nitride/Phosphide Heterostructure Coated by Multi-Doped Carbon as Electrocatalyst for Efficient Water Splitting and Neutral-pH Hydrogen Evolution Reaction, ChemElectroChem. 7 (2020) 289–298. https://doi.org/10.1002/celc.201901860.

[141] S. Mondal, C.R. Raj, Copper Nitride Nanostructure for the Electrocatalytic Reduction of Oxygen: Kinetics and Reaction Pathway, J. Phys. Chem. C. 122 (2018) 18468–18475. https://doi.org/10.1021/acs.jpcc.8b03840.

[142] L.C. Wang, B.H. Liu, C.Y. Su, W.S. Liu, C.C. Kei, K.W. Wang, T.P. Perng, Electronic band structure and electrocatalytic performance of cu3n nanocrystals, ACS Appl. Nano Mater. 1 (2018) 3673–3681. https://doi.org/10.1021/acsanm.8b00787.

[143] X.Y. Fan, Z.J. Li, A.L. Meng, C. Li, Z.G. Wu, P.X. Yan, Study on the structure, morphology and properties of Fe-doped Cu_3N films, J. Phys. D. Appl. Phys. 47 (2014) 185304. https://doi.org/10.1088/0022-3727/47/18/185304.

[144] A. Sivanantham, P. Ganesan, A. Vinu, S. Shanmugam, Surface Activation and Reconstruction of Non-Oxide-Based Catalysts through in Situ Electrochemical Tuning for Oxygen Evolution Reactions in Alkaline Media, ACS Catal. 10 (2020) 463–493. https://doi.org/10.1021/acscatal.9b04216.

[145] Y. Yang, R. Zeng, Y. Xiong, F.J. Disalvo, H.D. Abruña, Cobalt-Based Nitride-Core Oxide-Shell Oxygen Reduction Electrocatalysts, J. Am. Chem. Soc. 141 (2019) 19241–19245. https://doi.org/10.1021/jacs.9b10809.

[146] K. Ren, P. Yin, Y. Zhou, X. Cao, C. Dong, L. Cui, H. Liu, X. Du, Localized Defects on Copper Sulfide Surface for Enhanced Plasmon Resonance and Water Splitting, Small. 13 (2017) 1700867. https://doi.org/10.1002/smll.201700867.

[147] M. Bajdich, M. García-Mota, A. Vojvodic, J.K. Nørskov, A.T. Bell, Theoretical investigation of the activity of cobalt oxides for the electrochemical oxidation of water, J. Am. Chem. Soc. 135 (2013) 13521–13530. https://doi.org/10.1021/ja405997s.

[148] J. Wang, L. Gan, W. Zhang, Y. Peng, H. Yu, Q. Yan, X. Xia, X. Wang, In situ formation of molecular Ni-Fe active sites on heteroatom-doped graphene as a heterogeneous electrocatalyst toward oxygen evolution,

Sci. Adv. 4 (2018) 7970. https://doi.org/10.1126/sciadv.aap7970.
[149] J. Ren, Y. Huang, H. Zhu, B. Zhang, H. Zhu, S. Shen, G. Tan, F. Wu, H. He, S. Lan, X. Xia, Q. Liu, Recent progress on MOF-derived carbon materials for energy storage, Carbon Energy. 2 (2020) 176–202. https://doi.org/10.1002/cey2.44.
[150] R. Ramachandran, C. Zhao, D. Luo, K. Wang, F. Wang, Morphology-dependent electrochemical properties of cobalt-based metal organic frameworks for supercapacitor electrode materials, Electrochim. Acta. 267 (2018) 170–180. https://doi.org/10.1016/j.electacta.2018.02.074.
[151] G. Zhan, L. Fan, F. Zhao, Z. Huang, B. Chen, X. Yang, S. feng Zhou, Fabrication of Ultrathin 2D Cu-BDC Nanosheets and the Derived Integrated MOF Nanocomposites, Adv. Funct. Mater. 29 (2019) 1806720. https://doi.org/10.1002/adfm.201806720.
[152] J. Rong, J. Xu, F. Qiu, Y. Zhu, Y. Fang, J. Xu, T. Zhang, Sea Urchin-Like MOF-Derived Formation of Porous Cu_3P@C as an Efficient and Stable Electrocatalyst for Oxygen Evolution and Hydrogen Evolution Reactions, Adv. Mater. Interfaces. 6 (2019) 1900502. https://doi.org/10.1002/admi.201900502.
[153] W.J. Son, J. Kim, J. Kim, W.S. Ahn, Sonochemical synthesis of MOF-5, Chem. Commun. (2008) 6336–6338. https://doi.org/10.1039/b814740j.
[154] Z. Xue, J. Zhang, L. Peng, B. Han, T. Mu, J. Li, G. Yang, Poly(ethylene glycol) stabilized mesoporous metal-organic framework nanocrystals: Efficient and durable catalysts for the oxidation of benzyl alcohol, ChemPhysChem. 15 (2014) 85–89. https://doi.org/10.1002/cphc.201300809.
[155] H. Guo, Y. Zhu, S. Wang, S. Su, L. Zhou, H. Zhang, Combining coordination modulation with acid-base adjustment for the control over size of metal-organic frameworks, Chem. Mater. 24 (2012) 444–450. https://doi.org/10.1021/cm202593h.
[156] Y. Yue, Z.A. Qiao, P.F. Fulvio, A.J. Binder, C. Tian, J. Chen, K.M. Nelson, X. Zhu, S. Dai, Template-free synthesis of hierarchical porous metal-organic frameworks, J. Am. Chem. Soc. 135 (2013) 9572–9575. https://doi.org/10.1021/ja402694f.
[157] X. Cheng, A. Zhang, K. Hou, M. Liu, Y. Wang, C. Song, G. Zhang, X. Guo, Size- and morphology-controlled NH_2-MIL-53(Al) prepared in DMF-water mixed solvents, Dalt. Trans. 42 (2013) 13698–13705. https://doi.org/10.1039/c3dt51322j.
[158] B. Zhang, J. Zhang, C. Liu, X. Sang, L. Peng, X. Ma, T. Wu, B. Han, G. Yang, Solvent determines the formation and properties of metal-organic

frameworks, RSC Adv. 5 (2015) 37691–37696. https://doi.org/10.1039/c5ra02440d.

[159] F. Israr, D.K. Kim, Y. Kim, W. Chun, Scope of various solvents and their effects on solvothermal synthesis of Ni-BTC, Quim. Nova. 39 (2016) 669–675. https://doi.org/10.5935/0100-4042.20160068.

[160] F. Avilés, J. V. Cauich-Rodríguez, L. Moo-Tah, A. May-Pat, R. Vargas-Coronado, Evaluation of mild acid oxidation treatments for MWCNT functionalization, Carbon N. Y. 47 (2009) 2970–2975. https://doi.org/10.1016/j.carbon.2009.06.044.

[161] Y. Cheng, X. Wang, C. Jia, Y. Wang, L. Zhai, Q. Wang, D. Zhao, Ultrathin mixed matrix membranes containing two-dimensional metal-organic framework nanosheets for efficient CO_2/CH_4 separation, J. Memb. Sci. 539 (2017) 213–223. https://doi.org/10.1016/j.memsci.2017.06.011.

[162] P. Kubica, A. Wolinska-Grabczyk, E. Grabiec, M. Libera, M. Wojtyniak, S. Czajkowska, M. Domański, Gas transport through mixed matrix membranes composed of polysulfone and copper terephthalate particles, Microporous Mesoporous Mater. 235 (2016) 120–134. https://doi.org/10.1016/j.micromeso.2016.07.037.

[163] D.A. Palmer, P. Bénézeth, Solubility of copper oxides in water and steam, 14th Int. Conf. Prop. Water Steam Kyoto. (2008) 491–496.

[164] M.E. Wadsworth, D.R. Wadia, Reaction Rate Study of the Dissolution of Cuprite in Sulphuric Acid, Jom. 7 (1955) 755–759. https://doi.org/10.1007/bf03377565.

[165] R.D. Kent, P.J. Vikesland, Dissolution and Persistence of Copper-Based Nanomaterials in Undersaturated Solutions with Respect to Cupric Solid Phases, Environ. Sci. Technol. 50 (2016) 6772–6781. https://doi.org/10.1021/acs.est.5b04719.

[166] H. Majima, Y. Awakura, K. Enami, H. Ueshima, T. Hirato, Kinetic study of the dissolution of cuprite in oxyacid solutions, Metall. Trans. B. 20 (1989) 573–580. https://doi.org/10.1007/BF02655914.

[167] J.J. Harper, P. Janik, Terephthalic Acid Solubility, J. Chem. Eng. Data. 15 (1970) 439–440. https://doi.org/10.1021/je60046a031.

[168] T. Kim, J. Lee, K.H. Lee, Microwave heating of carbon-based solid materials, Carbon Lett. 15 (2014) 15–24. https://doi.org/10.5714/CL.2014.15.1.015.

[169] J.M. Kim, D. Ko, J. Oh, J. Lee, T. Hwang, Y. Jeon, W. Hooch Antink, Y. Piao, Electrochemically exfoliated graphene as a novel microwave susceptor: The ultrafast microwave-assisted synthesis of carbon-coated silicon-graphene film as a lithium-ion battery anode, Nanoscale. 9 (2017)

15582–15590. https://doi.org/10.1039/c7nr04657j.
[170] R. Kumari, A. Sahai, N. Goswami, Effect of nitrogen doping on structural and optical properties of ZnO nanoparticles, Prog. Nat. Sci. Mater. Int. 25 (2015) 300–309. https://doi.org/10.1016/j.pnsc.2015.08.003.
[171] A. Sahai, Y. Kumar, V. Agarwal, S.F. Olive-Méndez, N. Goswami, Doping concentration driven morphological evolution of Fe doped ZnO nanostructures, J. Appl. Phys. 116 (2014) 164315. https://doi.org/10.1063/1.4900721.
[172] J.T. Luo, Y.C. Yang, X.Y. Zhu, G. Chen, F. Zeng, F. Pan, Enhanced electromechanical response of Fe-doped ZnO films by modulating the chemical state and ionic size of the Fe dopant, Phys. Rev. B - Condens. Matter Mater. Phys. 82 (2010) 014116. https://doi.org/10.1103/PhysRevB.82.014116.
[173] B.Y.R.D. Shannon, M. H, N.H. Baur, O.H. Gibbs, M. Eu, V. Cu, Revised Effective Ionic Radii and Systematic Studies of Interatomie Distances in Halides and Chaleogenides, Acta Cryst. A 32 (1976) 751–767.
[174] H. Guo, L. Liu, Q. Wu, L. Li, X. Tai, Cu_3N nanowire array as a high-efficiency and durable electrocatalyst for oxygen evolution reaction, Dalt. Trans. 48 (2019) 5131–5134. https://doi.org/10.1039/c9dt00362b.
[175] T.N. Huan, G. Rousse, S. Zanna, I.T. Lucas, X. Xu, N. Menguy, V. Mougel, M. Fontecave, A Dendritic Nanostructured Copper Oxide Electrocatalyst for the Oxygen Evolution Reaction, Angew. Chemie - Int. Ed. 56 (2017) 4792–4796. https://doi.org/10.1002/anie.201700388.
[176] B. Zhang, C. Li, G. Yang, K. Huang, J. Wu, Z. Li, X. Cao, D. Peng, S. Hao, Y. Huang, Nanostructured CuO/C Hollow Shell@3D Copper Dendrites as a Highly Efficient Electrocatalyst for Oxygen Evolution Reaction, ACS Appl. Mater. Interfaces. 10 (2018) 23807–23812. https://doi.org/10.1021/acsami.8b05948.
[177] C.C. Hou, Q.Q. Chen, C.J. Wang, F. Liang, Z. Lin, W.F. Fu, Y. Chen, Self-supported cedarlike semimetallic Cu_3P nanoarrays as a 3D high-performance Janus electrode for both oxygen and hydrogen evolution under basic conditions, ACS Appl. Mater. Interfaces. 8 (2016) 23037–23048. https://doi.org/10.1021/acsami.6b06251.
[178] J. Masud, W.P.R. Liyanage, X. Cao, A. Saxena, M. Nath, Copper Selenides as High-Efficiency Electrocatalysts for Oxygen Evolution Reaction, ACS Appl. Energy Mater. 1 (2018) 4075–4083. https://doi.org/10.1021/acsaem.8b00746.
[179] M. Chauhan, K.P. Reddy, C.S. Gopinath, S. Deka, Copper Cobalt Sulfide Nanosheets Realizing a Promising Electrocatalytic Oxygen

Evolution Reaction, ACS Catal. 7 (2017) 5871–5879. https://doi.org/10.1021/acscatal.7b01831.

[180] S. Wei, K. Qi, Z. Jin, J. Cao, W. Zheng, H. Chen, X. Cui, One-step synthesis of a self-supported copper phosphide nanobush for overall water splitting, ACS Omega. 1 (2021) 1367–1373. https://doi.org/10.1021/acsomega.6b00366.

[181] J. Hao, W. Yang, Z. Huang, C. Zhang, Superhydrophilic and Superaerophobic Copper Phosphide Microsheets for Efficient Electrocatalytic Hydrogen and Oxygen Evolution, Adv. Mater. Interfaces. 3 (2016) 1–8. https://doi.org/10.1002/admi.201600236.

[182] X. Liu, S. Cui, M. Qian, Z. Sun, P. Du, In situ generated highly active copper oxide catalysts for the oxygen evolution reaction at low overpotential in alkaline solutions, Chem. Commun. 52 (2016) 5546–5549. https://doi.org/10.1039/c6cc00526h.

[183] F. Arshad, A. Munir, Q.Q. Kashif, T. ul Haq, J. Iqbal, F. Sher, I. Hussain, Controlled development of higher-dimensional nanostructured copper oxide thin films as binder free electrocatalysts for oxygen evolution reaction, Int. J. Hydrogen Energy. 45 (2020) 16583–16590. https://doi.org/10.1016/j.ijhydene.2020.04.152.

[184] C.W. Wu, B. Unnikrishnan, A.P. Periasamy, I.W.P. Chen, Y.T. Tseng, Y.Y. Yang, W.J. Lin, C.C. Huang, H.T. Chang, Importance of Cobalt-Doping for the Preparation of Hollow CuBr/Co@CuO Nanocorals on Copper Foils with Enhanced Electrocatalytic Activity and Stability for Oxygen Evolution Reaction, ACS Sustain. Chem. Eng. 8 (2020) 9794–9802. https://doi.org/10.1021/acssuschemeng.0c02309.

[185] C. Panda, P.W. Menezes, M. Zheng, S. Orthmann, M. Driess, In Situ Formation of Nanostructured Core-Shell Cu_3N-CuO to Promote Alkaline Water Electrolysis, ACS Energy Lett. 4 (2019) 747–754. https://doi.org/10.1021/acsenergylett.9b00091.

[186] L. Wang, X. Ge, Y. Li, J. Liu, L. Huang, L. Feng, Y. Wang, Nickel enhanced the catalytic activities of amorphous copper for the oxygen evolution reaction, J. Mater. Chem. A. 5 (2017) 4331–4334. https://doi.org/10.1039/c6ta10866k.

[187] A.A. Yadav, Y.M. Hunge, S.B. Kulkarni, C. Terashima, S.W. Kang, Three-dimensional nanoflower–like hierarchical array of multifunctional copper cobaltate electrode as efficient electrocatalyst for oxygen evolution reaction and energy storage application, J. Colloid Interface Sci. 576 (2020) 476–485. https://doi.org/10.1016/j.jcis.2020.04.100.

[188] A. Serov, N.I. Andersen, A.J. Roy, I. Matanovic, K. Artyushkova, P.

Atanassov, $CuCo_2O_4$ ORR/OER Bi-Functional Catalyst: Influence of Synthetic Approach on Performance , J. Electrochem. Soc. 162 (2015) F449–F454. https://doi.org/10.1149/2.0921504jes.

[189] R. Hinogami, K. Toyoda, M. Aizawa, T. Kawasaki, H. Gyoten, Copper Delafossite Anode for Water Electrolysis, ECS Trans. 58 (2013) 27–31. https://doi.org/10.1149/05802.0027ecst.

[190] Z. Xu, H. Pan, Y. Lin, Z. Yang, J. Wang, Y. Gong, Constructing a hexagonal copper-coin-shaped $NiCoSe_2$@NiO@$CoNi_2S_4$@CoS_2 hybrid nanoarray on nickel foam as a robust oxygen evolution reaction electrocatalyst, J. Mater. Chem. A. 6 (2018) 18641–18648. https://doi.org/10.1039/c8ta06084c.

[191] BP, Statistical Review of World Energy, (2016).

[192] L. Yu, Q. Zhu, S. Song, B. McElhenny, D. Wang, C. Wu, Z. Qin, J. Bao, Y. Yu, S. Chen, Z. Ren, Non-noble metal-nitride based electrocatalysts for high-performance alkaline seawater electrolysis, Nat. Commun. 10 (2019) 5106. https://doi.org/10.1038/s41467-019-13092-7.

[193] I. Dincer, C. Zamfirescu, Sustainable Hydrogen Production, Sustain. Hydrog. Prod. 305 (2016) 972–974. https://doi.org/10.1016/b978-0-444-64203-5.00001-0.

[194] S.Y. Tee, K.Y. Win, W.S. Teo, L.D. Koh, S. Liu, C.P. Teng, M.Y. Han, Recent Progress in Energy-Driven Water Splitting, Adv. Sci. 4 (2017). https://doi.org/10.1002/advs.201600337.

[195] I. Roger, M.A. Shipman, M.D. Symes, Earth-abundant catalysts for electrochemical and photoelectrochemical water splitting, Nat. Rev. Chem. 1 (2017) 0003. https://doi.org/10.1038/s41570-016-0003.

[196] J.N. Tiwari, A.M. Harzandi, M. Ha, S. Sultan, C.W. Myung, H.J. Park, D.Y. Kim, P. Thangavel, A.N. Singh, P. Sharma, S.S. Chandrasekaran, F. Salehnia, J.W. Jang, H.S. Shin, Z. Lee, K.S. Kim, High-Performance Hydrogen Evolution by Ru Single Atoms and Nitrided-Ru Nanoparticles Implanted on N-Doped Graphitic Sheet, Adv. Energy Mater. 9 (2019) 1900931. https://doi.org/10.1002/aenm.201900931.

[197] C.H. Chen, D. Wu, Z. Li, R. Zhang, C.G. Kuai, X.R. Zhao, C.K. Dong, S.Z. Qiao, H. Liu, X.W. Du, Ruthenium-Based Single-Atom Alloy with High Electrocatalytic Activity for Hydrogen Evolution, Adv. Energy Mater. 9 (2019) 1803913. https://doi.org/10.1002/aenm.201803913.

[198] C.C.L. McCrory, S. Jung, J.C. Peters, T.F. Jaramillo, Benchmarking heterogeneous electrocatalysts for the oxygen evolution reaction, J. Am. Chem. Soc. 135 (2013) 16977–16987. https://doi.org/10.1021/ja407115p.

[199] L. Xu, Q. Jiang, Z. Xiao, X. Li, J. Huo, S. Wang, L. Dai, Plasma-

Engraved Co_3O_4 Nanosheets with Oxygen Vacancies and High Surface Area for the Oxygen Evolution Reaction , Angew. Chemie. 128 (2016) 5363–5367. https://doi.org/10.1002/ange.201600687.

[200] Z. Shi, K. Nie, Z.J. Shao, B. Gao, H. Lin, H. Zhang, B. Liu, Y. Wang, Y. Zhang, X. Sun, X.M. Cao, P. Hu, Q. Gao, Y. Tang, Phosphorus-Mo2C@carbon nanowires toward efficient electrochemical hydrogen evolution: Composition, structural and electronic regulation, Energy Environ. Sci. 10 (2017) 1262–1271. https://doi.org/10.1039/c7ee00388a.

[201] Y. Li, X. Tan, S. Chen, X. Bo, H. Ren, S.C. Smith, C. Zhao, Processable Surface Modification of Nickel-Heteroatom (N, S) Bridge Sites for Promoted Alkaline Hydrogen Evolution, Angew. Chemie - Int. Ed. 58 (2019) 461–466. https://doi.org/10.1002/anie.201808629.

[202] M. Görlin, P. Chernev, J.F. De Araújo, T. Reier, S. Dresp, B. Paul, R. Krähnert, H. Dau, P. Strasser, Oxygen evolution reaction dynamics, faradaic charge efficiency, and the active metal redox states of Ni-Fe oxide water splitting electrocatalysts, J. Am. Chem. Soc. 138 (2016) 5603–5614. https://doi.org/10.1021/jacs.6b00332.

[203] P.F. Liu, X. Li, S. Yang, M.Y. Zu, P. Liu, B. Zhang, L.R. Zheng, H. Zhao, H.G. Yang, $Ni_2P(O)/Fe_2P(O)$ Interface Can Boost Oxygen Evolution Electrocatalysis, ACS Energy Lett. 2 (2017) 2257–2263. https://doi.org/10.1021/acsenergylett.7b00638.

[204] M.R. Gao, J.X. Liang, Y.R. Zheng, Y.F. Xu, J. Jiang, Q. Gao, J. Li, S.H. Yu, An efficient molybdenum disulfide/cobalt diselenide hybrid catalyst for electrochemical hydrogen generation, Nat. Commun. 6 (2015) 5982. https://doi.org/10.1038/ncomms6982.

[205] G. Yilmaz, C.F. Tan, Y.F. Lim, G.W. Ho, Pseudomorphic Transformation of Interpenetrated Prussian Blue Analogs into Defective Nickel Iron Selenides for Enhanced Electrochemical and Photo-Electrochemical Water Splitting, Adv. Energy Mater. 9 (2019) 1802983. https://doi.org/10.1002/aenm.201802983.

[206] S. Dong, X. Chen, X. Zhang, G. Cui, Nanostructured transition metal nitrides for energy storage and fuel cells, Coord. Chem. Rev. 257 (2013) 1946–1956. https://doi.org/10.1016/j.ccr.2012.12.012.

[207] N. Han, P. Liu, J. Jiang, L. Ai, Z. Shao, S. Liu, Recent advances in nanostructured metal nitrides for water splitting, J. Mater. Chem. A. 6 (2018) 19912–19933. https://doi.org/10.1039/c8ta06529b.

[208] J. Jia, M. Zhai, J. Lv, B. Zhao, H. Du, J. Zhu, Nickel Molybdenum Nitride Nanorods Grown on Ni Foam as Efficient and Stable Bifunctional Electrocatalysts for Overall Water Splitting, ACS Appl.

Mater. Interfaces. 10 (2018) 30400–30408. https://doi.org/10.1021/acsami.8b09854.

[209] H. Yin, C. Zhang, F. Liu, Y. Hou, Hybrid of iron nitride and nitrogen-doped graphene aerogel as synergistic catalyst for oxygen reduction reaction, Adv. Funct. Mater. 24 (2014) 2930–2937. https://doi.org/10.1002/adfm.201303902.

[210] F. Yu, H. Zhou, Z. Zhu, J. Sun, R. He, J. Bao, S. Chen, Z. Ren, Three-Dimensional Nanoporous Iron Nitride Film as an Efficient Electrocatalyst for Water Oxidation, ACS Catal. 7 (2017) 2052–2057. https://doi.org/10.1021/acscatal.6b03132.

[211] Y. Hu, D. Huang, J. Zhang, Y. Huang, M.S.J.T. Balogun, Y. Tong, Dual Doping Induced Interfacial Engineering of Fe_2N/Fe_3N Hybrids with Favorable d-Band towards Efficient Overall Water Splitting, ChemCatChem. 11 (2019) 6051–6060. https://doi.org/10.1002/cctc.201901224.

[212] Q. Chen, R. Wang, M. Yu, Y. Zeng, F. Lu, X. Kuang, X. Lu, Bifunctional Iron–Nickel Nitride Nanoparticles as Flexible and Robust Electrode for Overall Water Splitting, Electrochim. Acta. 247 (2017) 666–673. https://doi.org/10.1016/j.electacta.2017.07.025.

[213] X. Liu, X. Lv, P. Wang, Q. Zhang, B. Huang, Z. Wang, Y. Liu, Z. Zheng, Y. Dai, Improving the HER activity of Ni_3FeN to convert the superior OER electrocatalyst to an efficient bifunctional electrocatalyst for overall water splitting by doping with molybdenum, Electrochim. Acta. 333 (2020) 135488. https://doi.org/10.1016/j.electacta.2019.135488.

[214] J. Zhang, T. Wang, P. Liu, Z. Liao, S. Liu, X. Zhuang, M. Chen, E. Zschech, X. Feng, Efficient hydrogen production on $MoNi_4$ electrocatalysts with fast water dissociation kinetics, Nat. Commun. 8 (2017) 15437. https://doi.org/10.1038/ncomms15437.

[215] M. Ma, A. Bétard, I. Weber, N.S. Al-Hokbany, R.A. Fischer, N. Metzler-Nolte, Iron-based metal-organic frameworks MIL-88B and NH_2-MIL-88B: High quality microwave synthesis and solvent-induced lattice “breathing,” Cryst. Growth Des. 13 (2013) 2286–2291. https://doi.org/10.1021/cg301738p.

[216] S. Choi, W. Cha, H. Ji, D. Kim, H.J. Lee, M. Oh, Synthesis of hybrid metal-organic frameworks of $\{Fe_xM_yM'_{1-x-y}\}$-MIL-88B and the use of anions to control their structural features, Nanoscale. 8 (2016) 16743–16751. https://doi.org/10.1039/c6nr05463c.

[217] P. Horcajada, F. Salles, S. Wuttke, T. Devic, D. Heurtaux, G. Maurin, A. Vimont, M. Daturi, O. David, E. Magnier, N. Stock, Y. Filinchuk, D. Popov, C. Riekel, G. Férey, C. Serre, How linker’s modification controls

swelling properties of highly flexible iron(III) dicarboxylates MIL-88, J. Am. Chem. Soc. 133 (2011) 17839–17847. https://doi.org/10.1021/ja206936e.

[218] O. Guselnikova, P. Postnikov, R. Elashnikov, E. Miliutina, V. Svorcik, O. Lyutakov, Metal-organic framework (MOF-5) coated SERS active gold gratings: A platform for the selective detection of organic contaminants in soil, Anal. Chim. Acta. 1068 (2019) 70–79. https://doi.org/10.1016/j.aca.2019.03.058.

[219] H. Qiao, Y. Yang, X. Dai, H. Zhao, J. Yong, L. Yu, X. Luan, M. Cui, X. Zhang, X. Huang, Amorphous (Fe)Ni-MOF-derived hollow (bi)metal/oxide@N-graphene polyhedron as effectively bifunctional catalysts in overall alkaline water splitting, Electrochim. Acta. 318 (2019) 430–439. https://doi.org/10.1016/j.electacta.2019.06.084.

[220] M. Yang, Y.N. Zhou, Y.N. Cao, Z. Tong, B. Dong, Y.M. Chai, Advances and Challenges of Fe-MOFs Based Materials as Electrocatalysts for Water Splitting, Appl. Mater. Today. 20 (2020) 100692. https://doi.org/10.1016/j.apmt.2020.100692.

[221] S. Foley, H. Geaney, G. Bree, K. Stokes, S. Connolly, M.J. Zaworotko, K.M. Ryan, Copper Sulfide (Cu_xS) Nanowire-in-Carbon Composites Formed from Direct Sulfurization of the Metal-Organic Framework HKUST-1 and Their Use as Li-Ion Battery Cathodes, Adv. Funct. Mater. 28 (2018) 1800587. https://doi.org/10.1002/adfm.201800587.

[222] F. Xie, X. Ma, W. Liu, Y. Wang, H. Dong, T. Mi, X. Jiang, J. Sha, An unprecedented molybdenum oxide based helical MOF with peroxidase-like activity synthesized by surfactant-thermal method, Inorg. Chem. Commun. 97 (2018) 93–97. https://doi.org/10.1016/j.inoche.2018.09.022.

[223] G. Huang, F. Zhang, L. Zhang, X. Du, J. Wang, L. Wang, Hierarchical $NiFe_2O_4/Fe_2O_3$ nanotubes derived from metal organic frameworks for superior lithium ion battery anodes, J. Mater. Chem. A. 2 (2014) 8048–8053. https://doi.org/10.1039/c4ta00200h.

[224] W. Chen, G. Qian, Q. Xu, C. Yu, M. Yu, Y. Xia, S. Yin, Efficient bifunctional catalysts for overall water splitting: Porous Fe-Mo oxide hybrid nanorods, Nanoscale. 12 (2020) 7116–7123. https://doi.org/10.1039/d0nr00446d.

[225] H. Chu, D. Zhang, B. Jin, M. Yang, Impact of morphology on the oxygen evolution reaction of 3D hollow Cobalt-Molybdenum Nitride, Appl. Catal. B Environ. 255 (2019) 117744. https://doi.org/10.1016/j.apcatb.2019.117744.

[226] Y. Li, X. Wei, L. Chen, J. Shi, M. He, Nickel-molybdenum nitride

nanoplate electrocatalysts for concurrent electrolytic hydrogen and formate productions, Nat. Commun. 10 (2019). https://doi.org/10.1038/s41467-019-13375-z.

[227] J.O.M. Bockris, T. Otagawa, Mechanism of oxygen evolution on perovskites, J. Phys. Chem. 87 (1983) 2960–2971. https://doi.org/10.1021/j100238a048.

[228] X. Chen, G. Liu, W. Zheng, W. Feng, W. Cao, W. Hu, P.A. Hu, Vertical 2D MoO_2/$MoSe_2$ Core–Shell Nanosheet Arrays as High-Performance Electrocatalysts for Hydrogen Evolution Reaction, Adv. Funct. Mater. 26 (2016) 8537–8544. https://doi.org/10.1002/adfm.201603674.

[229] C.G. Morales-Guio, L.A. Stern, X. Hu, Nanostructured hydrotreating catalysts for electrochemical hydrogen evolution, Chem. Soc. Rev. 43 (2014) 6555–6569. https://doi.org/10.1039/c3cs60468c.

[230] X. Wu, J. Li, Y. Li, Z. Wen, NiFeP-MoO_2 hybrid nanorods on nickel foam as high-activity and high-stability electrode for overall water splitting, Chem. Eng. J. 409 (2021) 128161. https://doi.org/10.1016/j.cej.2020.128161.

[231] P.W. Menezes, S. Yao, R. Beltrán-Suito, J.N. Hausmann, P. V. Menezes, M. Driess, Facile Access to an Active γ-NiOOH Electrocatalyst for Durable Water Oxidation Derived From an Intermetallic Nickel Germanide Precursor, Angew. Chemie - Int. Ed. (2020) 4640–4647. https://doi.org/10.1002/anie.202014331.

[232] Q. Wang, H. Zhao, F. Li, W. She, X. Wang, L. Xu, H. Jiao, Mo-doped Ni2P hollow nanostructures: highly efficient and durable bifunctional electrocatalysts for alkaline water splitting, J. Mater. Chem. A. 7 (2019) 7636–7643. https://doi.org/10.1039/c9ta01015g.

[233] H. Wu, W. Xiao, C. Guan, X. Liu, W. Zang, H. Zhang, J. Ding, Y.P. Feng, S.J. Pennycook, J. Wang, Hollow Mo-doped CoP nanoarrays for efficient overall water splitting, Nano Energy. 48 (2018) 73–80. https://doi.org/10.1016/j.nanoen.2018.03.034.

[234] M.W. Kanan, J. Yano, Y. Surendranath, M. Dincă, V.K. Yachandra, D.G. Nocera, Structure and valency of a cobalt-phosphate water oxidation catalyst determined by in situ X-ray spectroscopy, J. Am. Chem. Soc. 132 (2010) 13692–13701. https://doi.org/10.1021/ja1023767.

[235] P.F. Liu, S. Yang, L.R. Zheng, B. Zhang, H.G. Yang, Electrochemical etching of α-cobalt hydroxide for improvement of oxygen evolution reaction, J. Mater. Chem. A. 4 (2016) 9578–9584. https://doi.org/10.1039/c6ta04078k.

[236] P.F. Liu, S. Yang, L.R. Zheng, B. Zhang, H.G. Yang, Mo^{6+} activated multimetal oxygen-evolving catalysts, Chem. Sci. 8 (2017) 3484–3488.

https://doi.org/10.1039/c6sc04819f.
[237] F. Zhou, X. Zhang, R. Sa, S. Zhang, Z. Wen, R. Wang, The electrochemical overall water splitting promoted by MoS_2 in coupled nickel–iron (oxy)hydride/molybdenum sulfide/graphene composite, Chem. Eng. J. 397 (2020) 125454. https://doi.org/10.1016/j.cej.2020.125454.
[238] X. Zheng, B. Zhang, P. De Luna, Y. Liang, R. Comin, O. Voznyy, L. Han, F.P. García De Arquer, M. Liu, C.T. Dinh, T. Regier, J.J. Dynes, S. He, H.L. Xin, H. Peng, D. Prendergast, X. Du, E.H. Sargent, Theory-driven design of high-valence metal sites for water oxidation confirmed using in situ soft X-ray absorption, Nat. Chem. 10 (2018) 149–154. https://doi.org/10.1038/nchem.2886.
[239] B. Zhang, L. Wang, Z. Cao, S.M. Kozlov, F.P. García de Arquer, C.T. Dinh, J. Li, Z. Wang, X. Zheng, L. Zhang, Y. Wen, O. Voznyy, R. Comin, P. De Luna, T. Regier, W. Bi, E.E. Alp, C.W. Pao, L. Zheng, Y. Hu, Y. Ji, Y. Li, Y. Zhang, L. Cavallo, H. Peng, E.H. Sargent, High-valence metals improve oxygen evolution reaction performance by modulating 3d metal oxidation cycle energetics, Nat. Catal. 3 (2020) 985–992. https://doi.org/10.1038/s41929-020-00525-6.
[240] J.J. Zhang, C.M. Yang, C.Q. Jin, W.W. Bao, R.H. Nan, L. Hu, G. Liu, N.N. Zhang, Hierarchical iron molybdate nanostructure array for efficient water oxidation through optimizing electron density, Chem. Commun. 57 (2021) 3563–3566. https://doi.org/10.1039/d0cc07735f.
[241] N. Boucherit, A. Hugot-Le Goff, S. Joiret, Raman Studies of Corrosion Films Grown on Fe and Fe-6Mo in Pitting Conditions, Corr. Sci. 32 (1991) 497–507. https://doi.org/10.1016/0010-938X(91)90103-V.
[242] T. Wang, R. Jin, X. Wu, J. Zheng, X. Li, K. Ostrikov, A highly efficient Ni-Mo bimetallic hydrogen evolution catalyst derived from a molybdate incorporated Ni-MOF, J. Mater. Chem. A. 6 (2018) 9228–9235. https://doi.org/10.1039/c8ta01325j.
[243] Y. Zhang, H. Guo, X. Li, J. Du, W. Ren, R. Song, A 3D multi-interface structure of coral-like Fe-Mo-S/Ni_3S_2@NF using for high-efficiency and stable overall water splitting, Chem. Eng. J. 404 (2021) 126483. https://doi.org/10.1016/j.cej.2020.126483.
[244] T. Liu, M. Li, C. Jiao, M. Hassan, X. Bo, M. Zhou, H.L. Wang, Design and synthesis of integrally structured Ni_3N nanosheets/carbon microfibers/Ni3N nanosheets for efficient full water splitting catalysis, J. Mater. Chem. A. 5 (2017) 9377–9390. https://doi.org/10.1039/c7ta02217d.
[245] M. Jiang, Y. Li, Z. Lu, X. Sun, X. Duan, Binary nickel-iron nitride

nanoarrays as bifunctional electrocatalysts for overall water splitting, Inorg. Chem. Front. 3 (2016) 630–634. https://doi.org/10.1039/c5qi00232j.

[246] S. Dutta, A. Indra, Y. Feng, H.S. Han, T. Song, Promoting electrocatalytic overall water splitting with nanohybrid of transition metal nitride-oxynitride, Appl. Catal. B Environ. 241 (2019) 521–527. https://doi.org/10.1016/j.apcatb.2018.09.061.

[247] J.P. Perdew, K. Burke, M. Ernzerhof, Generalized gradient approximation made simple, Phys. Rev. Lett. 77 (1996) 3865–3868. https://doi.org/10.1103/PhysRevLett.77.3865.

[248] D. Joubert, From ultrasoft pseudopotentials to the projector augmented-wave method, Phys. Rev. B - Condens. Matter Mater. Phys. 59 (1999) 1758–1775. https://doi.org/10.1103/PhysRevB.59.1758.

[249] J. Zhang, Y. Liu, C. Sun, P. Xi, S. Peng, D. Gao, D. Xue, Accelerated Hydrogen Evolution Reaction in CoS_2 by Transition-Metal Doping, ACS Energy Lett. 3 (2018) 779–786. https://doi.org/10.1021/acsenergylett.8b00066.

[250] H. Wu, W. Xiao, C. Guan, X. Liu, W. Zang, H. Zhang, J. Ding, Y.P. Feng, S.J. Pennycook, J. Wang, Hollow Mo-doped CoP nanoarrays for efficient overall water splitting, Nano Energy. 48 (2018) 73–80. https://doi.org/10.1016/j.nanoen.2018.03.034.

[251] X. Liu, P. Wang, Q. Zhang, B. Huang, Z. Wang, Y. Liu, Z. Zheng, Y. Dai, X. Qin, X. Zhang, Synthesis of MoS_2/Ni_3S_2 heterostructure for efficient electrocatalytic hydrogen evolution reaction through optimizing the sulfur sources selection, Appl. Surf. Sci. 459 (2018) 422–429. https://doi.org/10.1016/j.apsusc.2018.08.024.

Chapter 3. Conclusion

This thesis demonstrated two examples of bimetallic transition nitride/oxynitride catalysts for efficient water electrolysis. Each electrocatalyst underwent a series of modifications including structural control, secondary metal introduction, and nitridation to maximize their catalytic performances.

The first study covered a strategic optimization of copper-based OER catalysts derived from MOFs. To the best of our knowledge, this is the first report on morphology variation of Cu-based MOF using solvent-dependent coordination kinetics of metal ions and organic linkers. As a result of this study, exquisite urchin-shaped MOFs were obtained in aqueous medium, unlike most previously reported methods for CuMOF synthesis that use toxic DMF as solvent. Iron was successfully incorporated into the urchin-shaped MOFs without significant morphology changes, and its derivate CuFeN/CNT composites exhibited considerable enhancements in OER activity. Compared to CuFeN catalysts derived from bulk MOFs, urchin-shaped MOF-derived CuFeN catalyst featured much smaller and well-distributed particles owing to the quick and even distribution of heat over the large surface area of the precursor MOF during the nitridation process. The all-microwave-assisted preparation process minimized the use of toxic organic solvent

and consumption of large amounts of energy and inert gas. The as-prepared optimal catalyst exhibited a current density as high as 350 mA cm^{-2} at an overpotential of 437 mV, which is a comparable value to the previously reported copper-based electrocatalysts.

The second study demonstrated a rapid microwave-assisted synthesis of uniform rod-like FeMo-MIL-88B microstructures and the excellent catalytic activity of its oxynitride derivate towards HER, OER, and overall water splitting. The catalysts transformed from MIL-88B were tiny nanoparticles confined in the initial porous microstructure, providing multiple active sites and pathway for electrolyte and gas transport. The effect of molybdenum incorporation and oxynitride formation on the electrochemical property and catalytic activity of FeMoON was investigated, and the results show that incorporation of Mo in optimal ratio significantly enhances the catalytic activity by tuning the sluggish Volmer step; and that N-doping significantly boosts water-splitting activity by enhancing charge transfer behavior. Two modifications combined, the optimized FeMoON alkaline water electrolyzer shows catalytic behavior surpassing that of the commercial Pt/C||RuO_2 electrolyzer (1.81 V and 1.89 V, respectively, for current density of 100 mA cm^{-2}). Moreover, FeMoON electrolyzer could bear 1000 cycles of accelerated degradation and 20 hours of constant applied

voltage without deterioration in current density, indicating good stability. It is worthy to note that the facility of both synthesis approaches enable large-scale production of catalysts unlike many of those reported in-situ grown catalysts that require direct growth on the substrate. The demonstrated synthesis approaches and conclusions of the aforementioned two studies are anticipated to inspire further studies on porous precursor-derived catalyst in the future.

Nevertheless, more effort is required to realize the transition metal-based catalysts for practical water electrolysis due to still-lacking electrochemical performances for large-scale production and unwanted side reactions such as degradation of catalysts or electrolytes. Extensive and intensive research is vital and therefore encouraged in order to establish the economic green-hydrogen system for a sustainable, better, cleaner, and affordable future for the next generation.

국문 초록

지난 수십 년간 각국은 지구 온난화를 늦출 필요성을 지속적으로 공론화해왔다. 이러한 정치적 움직임에도 불구하고 대기의 온실 가스 양은 빠른 속도로 증가하여 기후 변화 문제는 심각한 난제에서 본격적인 비상사태로 급등하였다. 지구 온난화에 대처하는 가장 효과적인 방법 중 하나는 현재의 탄소 기반 에너지 시스템을 녹색 수소 기반 에너지 시스템으로 전환하는 것이다. 수소는 전기, 열에너지 등의 최종 에너지로 변환 될 수 있으며, 전기와 달리 대용량으로 장기간 저장될 수 있다. 현재 화석 연료를 기반으로 한 수소 생산 방법은 상당한 양의 이산화탄소를 배출하기 때문에 재생 에너지를 기반으로 한 녹색 수소 생산이 필요 된다. 녹색 수소는 재생 에너지로 구동되는 전해조를 사용하는 물 전기 분해를 통해 생산될 수 있다.

물 전기 분해는 음극에서의 수소 발생 반응 (HER)과 양극에서의 산소 발생 반응 (OER)으로 구성되는데 본질적으로 느린 촉매 동역학으로 인해 실제 사용시 낮은 전기 화학 효율을 초래한다. 따라서 고도로 활성화 된 첨단 전기화학 촉매의 개발이 필요 된다. 과거에 Pt, Ru 및 Ir과 같은 백금족 금속이 높은 촉매 활성으로 인해 처음 제안되었지만 높은 비용, 희소성 및 불안정한 안정성으로 인해 대규모 산업 응용 분야에서 제한적이다. 이러한 이유로, 전이 금속 산화물, 탄화물, 인화물, 황화물, 질화물 및 산 질화물과 같은 다양한 형태의 지구에 풍부한 전이 금속이 대체 전기 촉매로서 집중적으로 조사되고 있다. 그 중에서도 전이 금속 질화물 / 산 질화물은 그의 화학적 안정성과 전도도를 포함한 유리한 특성으로 인해 큰 관심을 받고 있다. 그간 Co, Ni 및 Fe와 같은 전이 금속은 다양한 조합으로 광범위하게 연구되었으며 전기 분해에 유망한 것으로 입증되었다. 그러나 귀금속 기반 촉매에 비해 상대적으로 촉매 효율이 부족하기 때문에 추가 연구를

위한 여지가 충분하다.

본 논문에서는 수전해를 위한 전이금속 질화물/산질화물 기반 고성능 전기화학 촉매의 두 가지 예시를 제시한다.

첫 번째 연구에서는 구리-철 질화물/탄소나노튜브 복합체의 합성과 그의 전기화학 촉매 효율을 소개한다. 구리-철 질화물/탄소나노튜브 복합체는 유기금속 골격체 (MOF)를 전구체로 사용하여 마이크로파-질화를 통해 빠르게 합성될 수 있다. 전구체 MOF의 형태와 조성은 용매 의존적 성장 역학과 구리와 철 염의 비율을 조정하여 쉽게 제어 할 수 있다. 수성 매체에서 얻은 절묘한 성게 모양의 구리-철-MOF의 질화를 통해 얻어진 구리-철 질화물/탄소나노튜브 복합체는 크게 향상된 OER 활성을 나타내며 420mV의 적용된 과전압에서 전류 밀도가 단 4.25mA에서 236.32mA로 증가하여 5460.47 % 로 큰 폭의 향상을 보인다.

두 번째 연구에서는 마이크로파 합성법으로 빠르게 만들어진 MOF에서 파생 된 철-몰리브덴 산질화물 촉매의 제작과 수전해 성능을 다루었다. 철-몰리브덴 산질화물 촉매는 전구체 MOF의 다공성 미세 구조에 갇힌 5-10 nm 나노 입자로 구성되어 전해질 및 가스 수송을위한 여러 활성 부위와 경로를 제공한다. 또한 최적의 비율로 Mo를 첨가할 시 느린 Volmer 단계를 조정하여 촉매 활성이 크게 향상되는 것이 확인되었다. 철-몰리브덴 산질화물 촉매로 구성된 알칼리수 전해조는 상용 Pt/C || RuO_2 전해조 (100mA cm^{-2}의 전류 밀도에서 1.89V)를 능가하는 촉매 거동(100mA cm^{-2}의 전류 밀도에서 1.81V)과 우수한 안정성을 확보하였다.

두 연구 모두에서 개질되지 않은 비교군과 비교하여 개질된 촉매의 과전합이 크게 감소하는 것으로 보아 구조적 제어, 이중 금속 도입 및 질화 전략이 촉매활성 향상에 상당한 관련이 있음을 확인하였다.